Experimental Evaluation and Modeling of a Turbine Blade with Potassium Evaporative Cooling

by

Jessica L. Townsend

B.S. Mechanical Engineering
University of Massachusetts, Amherst, 1994

M.S. Mechanical Engineering
University of California, Davis, 1996

Submitted to the Department of Aeronautics and Astronautics
in partial fulfillment of the requirements for the degree of

Doctor of Philosophy
at the
MASSACHUSETTS INSTITUTE OF TECHNOLOGY

June 2004

Author.....
Department of Aeronautics and Astronautics
March 17, 2004 AERO

Certified by .....
Jack L. Kerrebrock
Professor (Emeritus) of Aeronautics and Astronautics
Thesis Supervisor

Certified by .....
Alan H. Epstein
R.C. Maclaurin Professor of Aeronautics and Astronautics
Doctoral Committee Chair

Certified by .....
Dr. David B. Stickler
Executive Vice President, Aerodyne Research, Inc.

Accepted by .....
Edward M. Greitzer
H.N. Slater Professor of Aeronautics and Astronautics
Chair, Department Committee on Graduate Students

Experimental Evaluation and Modeling of a Turbine Blade with Potassium Evaporative Cooling

by

Jessica L. Townsend

Submitted to the Department of Aeronautics and Astronautics
on March 17, 2004 in partial fulfillment of the
requirements for the degree of
Doctor of Philosophy in Aeronautics and Astronautics

Abstract

A new method of turbine blade cooling, the Return Flow Cascade, has been developed in which vaporization of a liquid metal such as potassium is used to maintain the blade surface at a nearly uniform temperature. Turbine blades cooled using this technology have lower blade temperature levels compared to that available with conventional air cooling, potentially resulting in higher firing temperatures or a choice of a wider range of materials for the hot gas path. The detailed operation of the Return Flow Cascade is described including fluid mechanic and heat transfer phenomena that occur at high heat flux and gravitational acceleration levels characteristic of modern gas turbine engines. The performance limits of the Return Flow Cascade are identified by the development of a theoretical model that estimates the performance of the system for a range of operating conditions found in the experimental test rig and in an actual gas turbine engine. These limits include vapor choking in the internal blade passages, pool boiling limits in the blade, and surface tension restriction of liquid flow. Experimental results are presented from testing in the Rotating Heat Transfer Rig at the Massachusetts Institute of Technology. An infrared detector capable of high scan rates was used to fully map the temperature distribution of a single, heated, rotating turbine blade. The blade surface temperature maps show that the Return Flow Cascade works as designed by enforcing a nearly constant temperature over the surface of the blade. Cascade initiation limits predicted by the internal vapor choking model are in good agreement with the test data.

Thesis Supervisor: Jack L. Kerrebrock
Title: Professor (Emeritus) of Aeronautics and Astronautics

Acknowledgements

A great number of people have provided guidance, support, and assistance during the five years I have been working on my doctoral dissertation. First and foremost, I would like to thank Professor Jack Kerrebrock for his unending support, encouragement, and expertise. His easy-going manner, availability, and enthusiasm, even during difficult times, were hugely appreciated. This project was his brainchild and he set me off and running at the start and allowed me to make it my own. A second major contributor without whom this project would not have gotten off the ground is Dr. David Stickler. His countless hours of work designing the experimental blade model and testing apparatus ensured that the testing work would be successful. His ongoing commitment to this project and his constant availability for advice and support is greatly appreciated. I also need to thank both Jack Kerrebrock and David Stickler for their ability to "rig up" solutions to experimental equipment problems. I've learned that sometimes the fast way IS the best way.

I would also like to thank the other members of my committee, Professor Alan Epstein and Professor Mark Spearing, as well as Professor Edward Greitzer and Dr. Jerry Guenette, for their excellent advice and guidance during my time at MIT. Your help is much appreciated and will not be forgotten.

The help and advice of Jimmy Letendre and Jack Costa was invaluable to the successful completion of this project. Their willingness to answer every question I had and make time to assist me in the laboratory went beyond the call of duty. I have come to know and like both of them immensely and will always be grateful for their assistance. Also, I would like to thank John Mingus of Applied Energy Systems who was instrumental in the assembly of the test model.

Lori Martinez did an excellent job of keeping me sane during my tenure in the Gas Turbine Laboratory. Her sympathetic ear, jars of candy, and knowledge of how things are done in the GTL made my time here much more pleasant.

I would like to thank the other GTL staff who assisted me in many ways: Holly Anderson, Viktor Dubrowski, Julie Finn, Mary McDavitt, Diana Park and Paul Warren. The students of the GTL are lucky to have you.

I would also like to thank past and present GTL students Raffi Babikian, Beilene Hao, Jameel Janjua, Jody Kirchner, Steve Lukachko and Chris Spadaccini for their help, humor and friendship.

I would like to thank the mentors and teachers who have inspired and supported me throughout the years, including Fran Funai, Professor George A. Russell and Professor James Baughn.

This would not have been possible without the close friendship of Brigitte Castaing, Victor Garzon, Adam Hendriks, Jessica Marquez, Anna McVittie, Alexis Stanke, Jon Szafranski, John Wright, and especially my roommate Andrea Migliassi. Special thanks to the bookclub girls and my friends at Tir na nOg for additional social support.

Finally, I would like to thank the most important people in my life, my family. I am so grateful for the love and encouragement that you have shown me in everything that I have set out to do, and it is only with your support that I have gotten to where I am today.

Dedicated to the memory of my grandfathers,
Leo Francis Murphy and Raymond Ellsworth Townsend

This work was supported by the Air Force under contract number F33615-00-C-2043 and was a joint project between the MIT Gas Turbine Laboratory and Aerodyne Research, Incorporated. Additional acknowledgements are given to Thermacore International, Incorporated for their assistance in charging the blade model, and Turbocam for the fabrication of the blade and condenser.

Contents

Acknowledgements 5

List of Figures 11

List of Tables 13

Nomenclature 15

Chapter 1 Introduction 19

1.1 Motivation 19

1.2 Objectives 21

1.3 Definition of Important Dimensionless Parameters 22

1.3.1 Evaporation in Liquid Pool 22

1.3.2 Vapor Flow 23

1.3.3 Condensation 23

1.3.4 Liquid Flow 23

1.4 Previous Work 24

1.5 Contributions of Thesis 26

Chapter 2 Experimental Procedure 29

2.1 Purpose of Experimental Work 29

2.2 Description of Experimental Setup 29

2.2.1 Blade Model with Integral Condenser 29

2.2.2 Rotating Heat Transfer Rig 34

2.2.3 Data Acquisition System 37

2.3 Experimental Procedure 38

2.4 Data Reduction 40

2.4.1 Current and Power 40

2.4.2 Infrared Detector Output 41

Chapter 3 Experimental Results 43

3.1 General Results and Observations 43

3.2 Initiation of Cascade Operation 43

3.3 Effect of Condenser Cooling Air Flow Rate 47

3.4 Heat Flux Threshold 49
3.5 Effects Specific to Experimental Apparatus 49
3.5.1 Excessive Hub Cooling by Ground Strap 49
3.5.2 Uneven Cooling due to Blade Tilt 53
3.6 Blade Failure 56
Chapter 4 Modeling and Performance Analysis 59
4.1 Modeling Approach 59
4.2 Time Scales 59
4.3 Pool Boiling 61
4.3.1 Conduction and Free Convection in Liquid Pool 62
4.3.2 Transition to Nucleate Boiling 64
4.3.3 Prediction of Critical Heat Flux 65
4.3.4 Boiling Regime for Engine Operation 69
4.4 Vapor Flow 70
4.4.1 Vapor Choking in Blade 70
4.5 Film Condensation 78
4.6 Liquid Flow 79
4.6.1 Flow Limit Due to Surface Tension 79
4.6.2 Fluid Flow Limit in Overflow Ports 81
4.7 Blade Conduction Analysis 82
4.7.1 Conduction Profile Comparison with Test Data 85
4.8 Effect of Coriolis Force 86
4.9 Modeling Conclusions 88
Chapter 5 Engine Implementation 89
5.1 Extension of Modeling Results to Engine Conditions 89
5.1.1 Pool Boiling 89
5.1.2 Vapor Choking 90
5.1.3 Film Condensation 91
5.1.4 Liquid Flow Limits 91
5.1.5 Blade Conduction 92

5.2 Issues for Implementation in an Engine 92
5.2.1 Blade Geometry 93
5.2.2 Condenser Design 93
5.2.3 Internal Coolant 93
5.3 Design Study 94
5.3.1 Engine Parameters 94
5.3.2 Evaporatively Cooled Nickel Based Alloy Turbine 96
5.3.3 Film Cooling of a Nickel Based Alloy Turbine Blade 104
5.3.4 Evaporative Cooling of a Low Alloy Steel Turbine Blade 106
5.3.5 Fuel as a Secondary Coolant for RFC Cooling 107
5.3.6 Design Study Summary 108
Chapter 6 Summary, Conclusions and Future Work 111
6.1 Summary of Major Findings 111
6.2 Conclusions 111
6.3 Future Work 112
References 145

List of Figures

Figure 1-1 Conceptual Schematic of Evaporative Cooling using the Return Flow Cascade 21
Figure 2-1 Cross-section of Blade Model and Integral Condenser 30
Figure 2-2 Pressure side, suction side, baffle and tip cap of blade model 31
Figure 2-3 Condenser, Condenser Housing and Base Plate 31
Figure 2-4 Shelf Detail 32
Figure 2-5 Blade Model Geometry and Nominal Dimensions 32
Figure 2-6 Local Heat Flux and Blade Skin Thickness Variation (Reference []) 33
Figure 2-7 Rotating Heat Transfer Rig 35
Figure 2-8 Rotating Arm and Transformers 35
Figure 2-9 Schematic of Rotating Heat Transfer Rig 35
Figure 2-10 Condenser Thermocouple Locations 37
Figure 2-11 Measured and Controlled Run Parameters for Run 12 39
Figure 2-12 Blade Surface Temperature Plot 42
Figure 3-1 Blade Temperature Distribution (K) with "Conduction Profile" (Run 7-37) 44
Figure 3-2 Blade Temperature Distribution (K) with "Conduction Profile" (Run 7-37) 44
Figure 3-3 Mid-chord Suction Side Temperature Profile 46
Figure 3-4 Blade Temperature Distribution (K), Cooling Air Flow Off (Run 9-9) 48
Figure 3-5 Blade Temperature Distribution (K), Cooling Air Flow On (Run 9-10) 48
Figure 3-6 Photograph of Copper Ground Strap Installation 50
Figure 3-7 Mid-Chord Suction Side Temperature Profile, Uncorrected Power = 300 W, Comparison with and without Ground Strap Installed 51
Figure 3-8 Post-Initiation Blade Temperature Distribution in degrees Kelvin, Run 7-47, ... 52
Figure 3-9 Post-Initiation Blade Temperature Distribution in degrees Kelvin, Run 19-12, ... 52
Figure 3-10 Photograph of Blade and Condenser Model with 6° Tilt 53
Figure 3-11 Temperature Difference between Suction Side and Pressure Side of Blade 54
Figure 3-12 Blade Temperature Distribution (K) for Operating Cascade with and without Blade Tilt 55

Figure 4-1 Boiling Curve [21] 61
Figure 4-2 Simplified Model of Liquid Pool in Shelf 62
Figure 4-3 Comparison of Empirical Correlations for CHF of Potassium, g = 9.8 m/s^2 69
Figure 4-4 Diagram of Blade and Condenser for Vapor Flow Analysis 71
Figure 4-5 Comparison of Minimum Temperature for Unchoked Vapor Flow in Blade as Indicated by Cascade Initiation with Test Data at 453G (15 RPS) 76
Figure 4-6 Pressure Gradient in Blade Port and Transition Section for Rotational Acceleration = 453G 77
Figure 4-7 Minimum Rotational Acceleration Require to Overcome Surface Tension Limits in Liquid Overflow Port 81
Figure 4-8 Schematic of Blade, Copper Bus Bar and Copper Ground Strap for Conduction Modeling Analysis 83
Figure 4-9 Blade Temperature Distribution (K), Corrected Power = 42.6 W (Run 7-32) 85
Figure 4-10 Mid-chord Suction Side Profile, Run 7-32 compared with Model Match 86
Figure 4-11 Effect of Coriolis Acceleration on Liquid and Vapor Flow in Blade for Rig and Engine Conditions 87
Figure 5-1 Minimum Blade Temperature for Non-Choked Vapor Flow in Blade Center Port... 91
Figure 5-2 Minimum Blade Port Temperature for Non-Choking Flow in Blade Port 97
Figure 5-3 Heat Exchanger Effectiveness of Condenser for Evaporative Cooling Design Study99
Figure 5-4 Schematic of Condenser Heat Exchanger Cross Section for Evaporatively Cooled Turbine Blade 100
Figure 5-5 Top View of Condenser 100
Figure 5-6 Schematic of Single Condenser Array Geometry 101
Figure 5-7 Required Cooling Air Flow for Range of Compressor Pressure Ratios 104
Figure A-6-1 Schematic of Infrared Imaging System for Blade Surface Temperature Measurement – Top View 116
Figure A-6-2 Schematic of Infrared Imaging System for blade Surface Temperature Measurement – Side View 116

List of Tables

Table 2-1 Parameters Monitored During Each Run 38
Table 3-1 Conditions at Initiation of Cascade Operation 47
Table 4-1 Time Scales for Two Phase and Flow Processes 60
Table 4-2 Comparison of CHF Test Conditions for Previously Published Work with Potassium and Current Experimental Set-up 66
Table 4-3 Comparison of Typical Film Condensation Parameters for Rig and Engine Conditions 79
Table 5-1 Maximum Conditions Expected and Achieved During Testing 89
Table 5-2 Engine Parameters for Design Study 95
Table 5-3 Blade Parameters for Design Study 96
Table 5-4 Condenser Parameters for Design Study 98
Table 5-5 Evaporative Cooling Results for Design Study 103
Table 5-6 Film Cooling Parameters for Design Study 104
Table 5-7 Results of Film Cooling Analysis for Design Study 106
Table 5-8 Cooling Performance Comparison of Nickel Based Alloy and Low Alloy Steel Turbine Blades 107

Nomenclature

Roman

A_{blade}	Surface area of the blade
A_{bcp}	Cross-sectional area of the blade center port
A_{free}	Free flow area of heat exchanger
A_{pool}	Cross-sectional area of the liquid pool in the shelf
A_{port}	Area of a liquid overflow port
A_s	Surface area of the blade
A_{scan}	Area of one infrared scan point
A_t	Total heat exchanger area
Bo	Bond number
c	Specific heat, blade chord
c_p	Specific heat at constant pressure
C_{cold}	Heat capacity of cold side of heat exchanger
C_{min}	Minimum heat capacity in heat exchanger
D_h	Hydraulic diameter
F_{st}	Force due to surface tension
F_p	Force due to pressure head
g	Acceleration of gravity
g_r	Acceleration of gravity in the r-direction
Gr_L	Grashof number
h	Depth of liquid pool in shelf
$\bar{h}$	Average heat transfer coefficient
h_{fg}	Heat of vaporization
I	Specific impulse
I_{blade}	Measured current through blade model
I_{rig}	Current measured at rig wall
k_l	Liquid thermal conductivity
L	Length

m_{liq}	Mass of liquid in RFC
$\dot{m}$	Mass flow
$\dot{m}_{air}$	Mass flow of cooling air to rig
$\dot{m}_{evap}$	Rate of evaporation in shelves
$\dot{m}_{ports}$	Mass flow through liquid overflow ports
M_o	Inlet Mach number
M_4	Mach number at turbine inlet
M_r	Radial Mach number
N_b	Number of blades
N_f	Number of fins
N_{shelf}	Number of shelves
Nu	Nusselt number
P	Pressure, Power, or Perimeter
P_{air}	Pressure of condenser cooling air
P_{corr}	Corrected power
P_{cr}	Critical pressure
P_G	Partial pressure of incondensable gases
P_L	Pressure at heater (shelf) surface
P_o	Ambient pressure
Pr	Prandtl number
PR	Pressure ratio
P_v	Vapor pressure
q	Heat flux to blade
q'''	Internal heat generation
q_{cr}	Critical heat flux
q_{shelf}	Heat flux to one cascade shelf
Q	Heat to blade
r	Radius
R	Radius

R_{tot}	Total resistance of fin array
r_{cond}	Radius from axis of rotation to bottom of condenser
$r_{cond,in}$	Radius from axis of rotation to bottom of baffle
r_{hub}	Radius from axis of rotation to blade hub
r_{tip}	Radius from axis of rotation to blade tip
Re	Reynolds number
Ro	Rossby number
RPS	Rotations per second
S	Blade span, Blade spacing
SFC	Specific fuel consumption
t	Time
$t_{conduction}$	Time scale for conduction in blade
t_{evap}	Time scale for evaporation
t_{liq}	Time scale for liquid flow
t_{vap}	Time scale for vapor flow
T	Temperature
$T_{air,in}$	Temperature of condenser cooling air in
$T_{air,out}$	Temperature of condenser cooling air out
T_b	Temperature at base of fin
$T_{blade,base}$	Temperature measured at the base of the blade
T_{blade}	Blade surface temperature matrix
T_c	Condenser temperature, temperature of cold side of heat exchanger
T_L	Temperature at heater surface
T_o	Inlet temperature
T_{sat}	Saturation temperature
T_w	Wall temperature
T_3	Compressor discharge temperature
T_4	Turbine inlet temperature
u_{liq}	Velocity of liquid
u_x	Velocity of vapor

V	Velocity of blade
V_{blade}	Voltage measured through blade model
V_{IR}	Voltage output from IR system
x	Distance along the liquid film in the condenser
z	Distance in the axial direction

Greek Symbols

α	Thermal diffusivity
β	Diffusion coefficient
δ	Thickness of liquid film
ε	Heat exchanger effectiveness
γ	Surface tension, Ratio of specific heats
Γ	Mass flow rate per unit width of condenser film
η_{ad}	Adiabatic film cooling effectiveness
η_c	Compressor adiabatic efficiency
η_f	Fin efficiency
η_o	Fin array efficiency
λ_d	Taylor instability wavelength
μ_l	Liquid viscosity
ν_l	Liquid dynamic viscosity
θ	Azimuthal angle
$\theta_{b,lm}$	Heat exchanger log-mean temperature difference
ρ_l	Liquid density
ρ_v	Vapor density
σ	Stefan – Bolztmann Constant
Ω	Rotational speed
ξ	Percentage of inert gas content of bubble

Chapter 1 Introduction

1.1 Motivation

The objective of the thesis research is to develop an improved understanding of and a technology base for an innovative form of cooling for gas turbines, termed Evaporative Cooling. As applied to the rotating parts of a gas turbine, Evaporative Cooling makes use of evaporation of a liquid in the interior of the turbine blade to enforce a nearly constant temperature in the blade, irrespective of the heat flux distribution, in a fashion similar to that of heat pipes. The function of the wick of the heat pipe, which is to draw the liquid from the cold end of the heat pipe through capillary action and distribute it in the evaporator, is replaced by the centrifugal force of the rotating turbine blade and an internal structure of capture shelves that distribute and retain liquid on the inner surface of the blade. These shelves, together with a condenser and the connecting flow paths, constitute a Return Flow Cascade. Thus, more specifically the objective of this research is to develop an improved understanding of the function of the Return Flow Cascade under conditions representative of applications in high performance gas turbines.

Existing high performance gas turbines use air taken from the compressor discharge to cool the turbine blades and other parts of the hot section of the engine by various means including internal convection cooling and film cooling. In convection cooling the blade is cooled by air flow in internal passages, while in film cooling air flows from holes in the blade surface to lower the effective temperature of the flow over the blade. These cooling approaches are well understood and quite effective, but they have fundamental characteristics that limit this effectiveness.

First amongst these is that the cooling air must be at a pressure at least equal to the turbine inlet pressure, therefore it must come from the compressor discharge, hence at the corresponding temperature. As compressor pressure ratios (and therefore temperature ratios) are increased to improve cycle efficiency, blade cooling effectiveness decreases. Second, the flow of cooling air out of the blade surfaces tends to disrupt the boundary layer flow and degrade turbine aerodynamic efficiency. These are system level limits. Another equally important issue is that some areas of the blade will be exposed to a higher heat flux. Although the air cooling

system is designed to cool these areas more aggressively, the actual heat flux distribution is difficult to predict. As a result there are variations in the blade temperature that produce corresponding thermal stresses, reducing the blade life. Evaporative Cooling eliminates the air flow through the blade surface and enforces near constancy of the blade temperature mitigating these problems.

In addition vaporization cooling offers the possibility of rejecting the cooling heat to a sink other than the compressor discharge air. Martinez-Tamayo [1] has shown that for conventional air cooling there is a turbine inlet temperature beyond which, due to increasing compressor discharge temperature, the performance increase from a higher firing temperature no longer exceeds the performance penalty associated with bleed air cooling. By removing the limit due to compressor discharge cooling, vaporization cooling could allow higher firing temperatures. It also offers the possibility of using lower weight and lower cost turbine blade materials. Thus, vaporization cooling offers distinct possibilities for improving the performance of the gas turbine.

Implementation of vaporization cooling depends on the viability of the Return Flow Cascade (RFC). The function of the RFC is to maintain a layer of liquid on the internal surfaces of the blade, where it can evaporate in response to the heat flux into the blade, and to return the liquid from a condenser, which converts the vapor to liquid. This is the function played by the wick in a heat pipe, but it is important to note that a classical heat pipe cannot function in the rotating turbine blade because the capillary pumping on which it depends cannot overcome the pressure gradient produced by rotation. In the Return Flow Cascade, liquid returning from the condenser enters the radially inwardmost shelf, from which some of it vaporizes and the rest continues to the next shelf. This cascade continues to the outermost shelf, so that all shelves are provided with just the amount of liquid required to match their evaporation rate. Figure 1-1 shows this at a conceptual level.

The function of the Return Flow Cascade has been verified in a number of modeling experiments [2] giving confidence that the fundamental mechanism is viable. However, prior to the present work, it had not been verified in a geometry representative of a turbine blade, nor had it been demonstrated with potassium as the two-phase cooling substance. This work addresses

these issues, in addition to providing a basis for modeling the behavior of the Return Flow Cascade under both rig testing and gas turbine engine conditions.

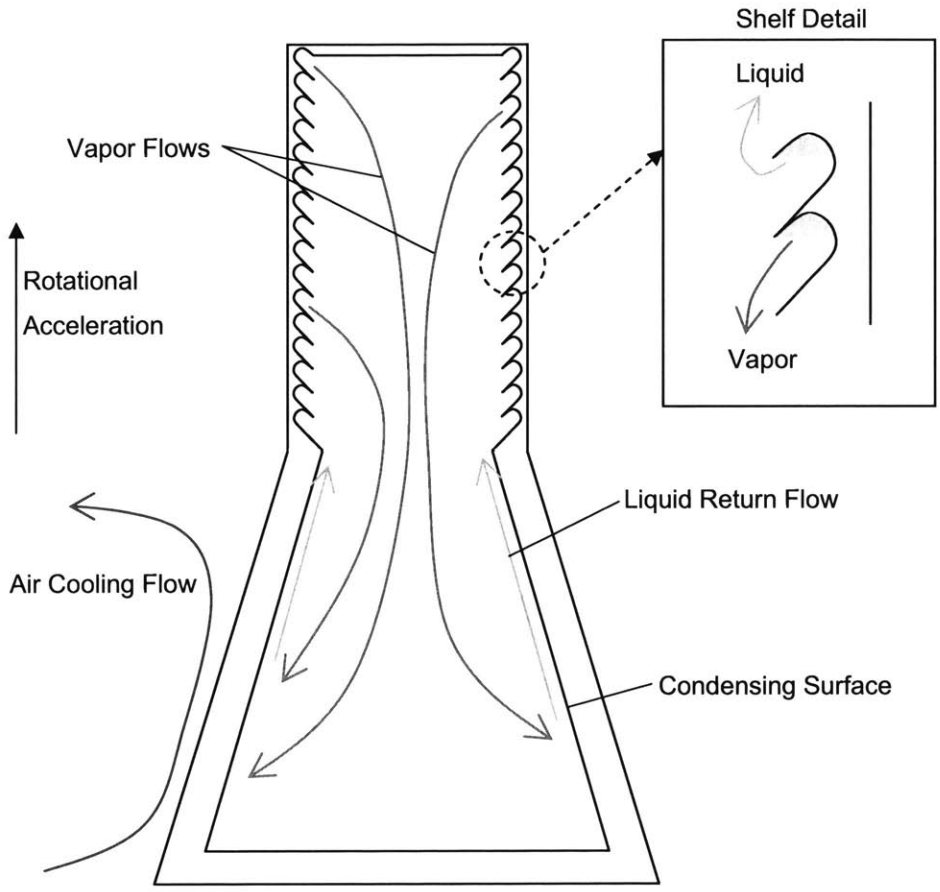

Figure 1-1 Conceptual Schematic of Evaporative Cooling using the Return Flow Cascade

1.2 Objectives

The main objective of this work is to develop an understanding of the behavior and limits of the evaporative cooling system as applied to turbine blade cooling in aircraft engines. A second objective is to provide detailed models of phenomena found in the return flow cascade including liquid metal fluid dynamics and heat transfer in a system with large rotational acceleration forces. A third objective is to use these models to determine the limits that affect

blade cooling effectiveness in modern gas turbine engines. A final objective is to provide the technical community with the first measurements of blade surface temperature of an evaporatively cooled turbine blade with heat loads similar to those found in gas turbines.

1.3 Definition of Important Dimensionless Parameters

Evaporatively cooled turbine blades are exposed to the same heat flux distribution and rotational acceleration levels as conventional air cooled blades, but there are additional characteristic dimensionless parameters that govern the internal flow processes due to the two-phase nature of the flow, the material properties of the liquid metal coolant, and the fact that evaporative cooling is a closed loop cooling system. The governing dimensionless parameters for the important processes in the Return Flow Cascade (evaporation in the capture shelves, vapor flow to the condenser, film condensation in the condenser, and liquid flow to the blade) are presented below.

1.3.1 Evaporation in Liquid Pool

The liquid potassium evaporates from liquid pools in the capture shelves that line the internal surface of the blade. The Prandtl number, Pr is the ratio of the momentum diffusivity and the thermal diffusivityis defined as

$$\mathrm{Pr} = \frac{\nu}{\alpha} \tag{1.1}$$

where ν is the dynamic viscosity and α is the thermal diffusivity. For liquid metals such as potassium, Pr << 1 which indicates that the thermal diffusion rate greatly exceeds the momentum diffusion rate and therefore thermal gradients in the liquid pools will propagate quickly. This is important for Return Flow Cascade operation in that if the thermal gradients in the pool are minimized, it is more likely that the pool will operate in the natural convection regime with evaporation from the free surface of the pool which is a stable mode of heat transfer.

1.3.2 Vapor Flow

The flow of potassium vapor through the blade to the condenser is governed by the effect of the Coriolis force and the Mach number. The effect that the Coriolis force has on the vapor flow can be quantified using the Rossby Number, defined as

$$\mathrm{Ro} = \frac{\mathrm{U}}{\mathrm{L}\Omega} \tag{1.2}$$

where U is a characteristic velocity of the flow, L is a characteristic distance, and Ω is the rotational speed. For Ro << 1 Coriolis effects dominate and for Ro >> 1, inertial effects dominate. For both the experimental and engine conditions, Ro ~ 10 which indicates that while Coriolis effects will not dominate, they may still have an effect on the flow.

The Mach number, M, for the vapor flow in the blade port can be used to determine whether or not the flow will choke. When M = 1, the vapor flow will be choked and the maximum mass flow rate for the given port area will be reached.

1.3.3 Condensation

When the vapor flow reaches the condenser, it will condensate on the condenser walls, either through film or drop-wise condensation. For film condensation the governing parameter is the Reynolds number which can be used to determine whether the film is laminar, wavy laminar or turbulent. The film Reynolds number is defined as

$$\mathrm{Re} = \frac{\Gamma}{\mu \mathrm{L}} \tag{1.3}$$

where Γ is the mass flux of liquid, μ is the dynamic viscosity, and L is the characteristic length for the liquid flow. For Re < 30 the film is laminar. For both experimental and engine conditions, Re > 30 indicating that film condensation will be wavy laminar or turbulent.

1.3.4 Liquid Flow

The liquid flows from the condenser into the first capture shelf. Once that shelf is filled additional liquid flows through liquid overflow ports to the next shelf, and so on. The flow in the liquid overflow port will be limited by surface tension effects if the Bond Number, Bo is less

than 1. The Bond number is the ratio of the bouyancy force to the surface tension and is defined as

$$Bo = \sqrt{\frac{\rho g D^2}{\gamma}} \tag{1.4}$$

where ρ is the liquid density, g is the rotational acceleration, D is the diameter of the port and γ is the surface tension of the liquid. There are some experimental conditions where Bo < 1 indicating that Return Flow Cascade operation was limited due to effects of surface tension in the liquid overflow ports.

1.4 Previous Work

Soon after the development of the gas turbine in the late 1930's, the need for turbine blade cooling was recognized. As early as 1940, Ernst Eckert and others at the NASA Lewis Research Center (now NASA Glenn) were exploring internal air cooling, transpiration cooling, film cooling and natural convection liquid cooling [3]. One of the earliest published proposals for liquid cooled turbine blades was made by Schmidt [4] in 1951 based on work he had done in Germany during World War II. His proposal was an open thermosyphon in which liquid water is fed into a hollow rotor and then through radial holes into the turbine blades. In 1955, Cohen and Bayley [5] reviewed several types of liquid cooling and commented that the two-phase closed thermosyphon "in which a quantity of liquid is enclosed within each blade to act as a conveyor of heat to the more easily cooled root" was the most suitable method for cooling turbine blades. They also noted that liquid metals would be an attractive choice of working fluid due to the fact that the internal operating pressure would be close to one atmosphere at expected blade temperatures, although their testing was done only with water, butyl alcohol and chlorobenzene.

In the 1960s methods to cool turbine blades using compressor bleed air were introduced into practice. These methods have a major advantage over liquid cooling, in that the coolant is supplied from and can be rejected to the engine core air flow. Air cooling has been the dominant cooling method since that time.

There have, however, been many analytical and experimental studies of liquid cooling in the last forty years. Gray [6] proposed a wickless rotating heat pipe integral with the shaft of the engine which would deliver liquid through radial passages to the turbine blades for cooling. The

shaft would have a slight internal taper at the condenser end such that the centrifugal force motivates the condensate back towards the evaporator end. This scheme is similar to Schmidt's early work except that it is a closed loop cooling system. Gray also focused on the effect of centrifugal acceleration on the phase change processes in the heat pipe.

Work has also been done on the static two-phase closed thermosyphon which operates at 1 G (9.81 m/s^2). The rotational acceleration levels in a rotating turbine blade are much higher than 1 G, but these studies provided the groundwork for future investigations of rotating thermosyphons. Many of the lessons learned from these early studies were used in the design of the Return Flow Cascade. Lee and Mital [7] performed tests on a static two-phase thermosyphon and explored the effect of fill volume on maximum heat flux. They found that there is maximum fill volume above which there is no additional advantage in terms of increased heat flux capability. Imura, Sasaguchi and Kozai [8] developed a correlation for the critical heat flux of a static two-phase closed thermosyphon. They determined that the critical heat flux for flow through small tubes is smaller than that for pool boiling. Hong, Chen and Wang [9] theoretically determined that the negative effects of noncondensable gases on condensation in a static thermosyphon are decreased at higher system temperature.

A number of experimental and theoretical studies of rotating two-phase thermosyphons were done, with the purpose of understanding the effects of heat flux, rotational acceleration thermosyphon geometry and noncondensable gases on the heat transfer performance. One of the first published analyses of a rotating two-phase closed thermosyphon using a liquid metal cooling was done by Genot and LeGrives [10]. They examined the vapor-liquid interaction under high centrifugal forces and also examined the effects of heat flux, rotating speed and cooling air flow rate experimentally in an evacuated rotating rig at moderate and high rates of rotation. They also confirmed that a two-phase thermosyphon is capable of dissipating the heat fluxes expected in gas turbine engines. Chato [11] investigated the phase change heat transfer of the film condensation layer in the condenser of a static two-phase closed thermosyphon. Ling, Cao, and Chang [12] derived closed form solutions for the liquid film distributions in the condenser section and the vapor temperature drop in the evaporator section of a radially rotating miniature thermosyphon at rotational speeds on the order of those found in gas turbine engines. They determined that the internal diameter, the rotating speed and the operating temperature can

affect the performance of the thermosyphon. Ling and Cao [13] then modified their analysis to include the effect of noncondensable gases. Finally, Ling, Cao and Lopez [14] tested their theoretical results by testing miniature rotating thermosyphons with a diameter on the order 1 mm and measured the effects of heat flux, cooling air flow rate, rotation rate and internal diameter. A similar experimental study was also done by Waowaew et al [15]. These studies on rotating thermosyphons prove that the concept of vaporization cooling as implemented in a thermosyphon is viable for turbine blade cooling.

Kerrebrock and Stickler [2, 16, 17, 18] performed the first experimental work on the Return Flow Cascade. They tested a cylindrical model with shelves axisymmetric about the radial direction coupled to a conical condenser with water as the working fluid. They were able to achieve a nearly constant temperature (within 20 C) between the evaporator and condenser and also found that the cascade has some self-regulating capability.

All the experimental work mentioned above was done using geometrically simple models. Ling et al and Waowaew both used a cylindrical thermosyphon, and Genot and LeGrives used a flat, parallelepiped model. The heat load in these studies was supplied by resistive heating through the model. In addition, temperature measurements were taken via surface mounted thermocouples.

Advanced methods for measuring the surface temperature of a rotating model have been developed. Katz [19] and Curwen [20] both described the use of a pyrometer as an onboard temperature sensor to detect overheating in the turbine rotor blades. Guidez [21] was the first to use an infrared pyrometer to take high spatial resolution temperature measurements of a rotating heated passage. This technique was also used at the MIT Gas Turbine Laboratory by Kreatsoulas [22], Barry [23] and Bons [24]. Using an infrared sensor and focusing mirrors, surface temperature maps of their rotating models were measured with a spatial resolution of 1 mm^2. The surface temperature measurement method outlined in the latter three references was used for this study.

1.5 Contributions of Thesis

The present study answers some important questions about the effectiveness and feasibility of the Return Flow Cascade for use in gas turbines and allows future researchers to

begin the process of implementing this technology in an engine. Unlike previous experiments outlined above, the model geometry is representative of an actual turbine blade and the heat flux to the blade is simulated to reflect the actual chordwise heat distribution typical of a gas turbine. In conjunction with experimental results, models of the fluid dynamics and heat transfer phenomena (including pool boiling, film condensation, vapor flow and liquid flow) are developed. While alkali metal heat transfer has been extensively studied in the context of heat pipes, the application of alkali metal internal cooling at the extreme conditions found in a gas turbine has not been studied. This project examined the behavior of alkali metals subjected to the extreme conditions in a gas turbine and also includes an analysis of how this behavior can be utilized to provide effective cooling for a turbine blade. This study also contains the first reported surface temperature measurements of a heated rotating turbine blade utilizing the Return Flow Cascade technology.

Chapter 2 Experimental Procedure

2.1 Purpose of Experimental Work

The purpose of the experimental work was to provide a characterization of evaporative cooling for a realistic turbine blade model with potassium as the coolant. This was accomplished by testing the system over a range of operating parameters (rotational speed, heat flux, and cooling air flow rate) while measuring the thermal response of the system. Specifically, the temperature gradients associated with the imposed heat flux distribution and the internal shelf structure spanwise spacing were determined.

2.2 Description of Experimental Setup

2.2.1 Blade Model with Integral Condenser

The system studied is a turbine blade with integral air cooled condenser and is shown in Figure 2-1. The internal wall of the turbine blade is lined with capture shelves from hub to tip that trap the liquid coolant. A photograph of the components of the blade before assembly is shown in Figure 2-2. The inner wall of the blade is lined with 27 shelves from hub to tip. The shelves are continuous along the entire perimeter of the blade and allow the liquid coolant level to equilibrate in each shelf. The blade span is 3.5 cm and the chord is 2.5 cm. The size of the blade model was constrained by the available clearance in the rotating rig and the facility cooling air flow capacity which affects the total heat input to the blade and hence the blade surface area.

The blade is welded to the condenser such that the blade center port as delineated by the baffle opens directly into the cooled condenser chamber. The condenser is rectangular in cross-section and is externally air cooled. Small air passages were machined into the long sides of the condenser and are shown in cross-section A-A of Figure 2-1. When the condenser housing (shown in the center of Figure 2-3) is slipped over the condenser it encloses the air passages and also creates the two main passages as plenum for cooling air in and out. The condenser "floats" in the housing to allow for differential thermal expansion.

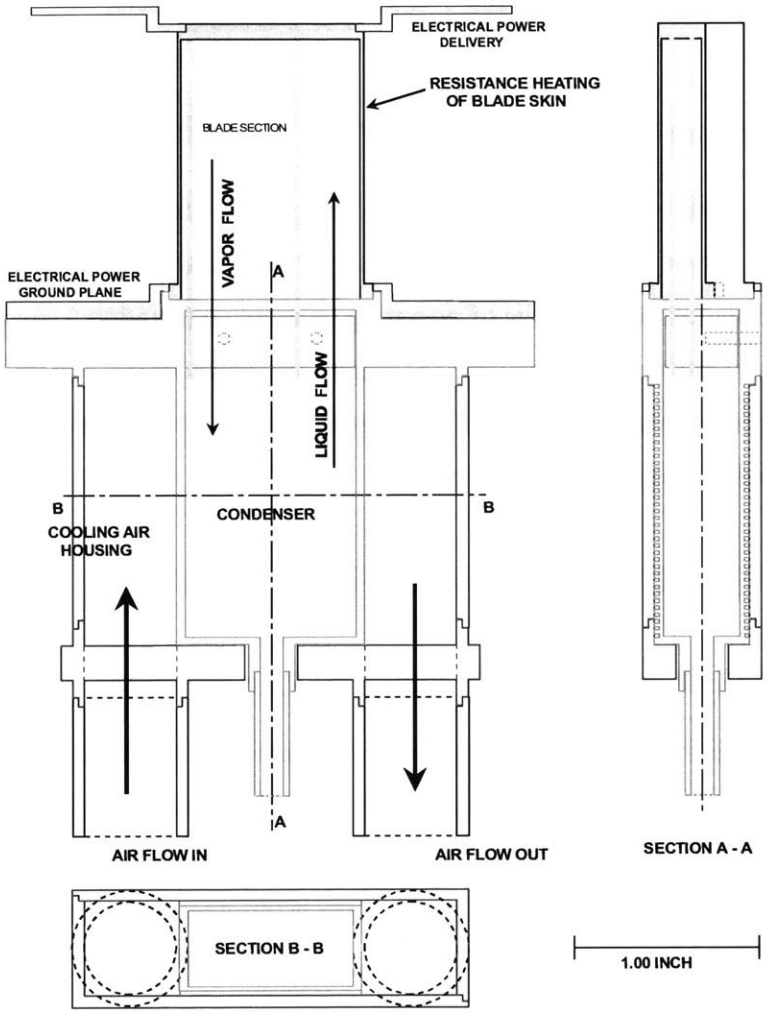

Figure 2-1 Cross-section of Blade Model and Integral Condenser

Potassium was chosen as the coolant because of its high heat of vaporization, its vapor pressure characteristics and its wetting ability. The vapor pressure curve for potassium indicates that at a typical average blade temperature (1050 K) the corresponding equilibrium vapor pressure at which evaporation will occur is approximately 1 atmosphere. The potassium fill amount was determined by calculating the amount of liquid that could be held in all the shelves, the volume taken up by a tip pool with a depth of 0.05 inch, the volume of liquid that forms the liquid film in the condenser, and the volume of vapor needed to fill the remainder of the empty space in the blade. The final fill amount calculated for potassium was 0.45 grams which corresponds to 4% of the void volume of the blade and condenser system. The potassium fill

tube is located at the bottom of the condenser and shown in Figure 2-1. First, the blade was evacuated, then the correct amount of potassium was loaded into the blade through the fill tube, and finally the fill tube was pinched off and sealed closed.

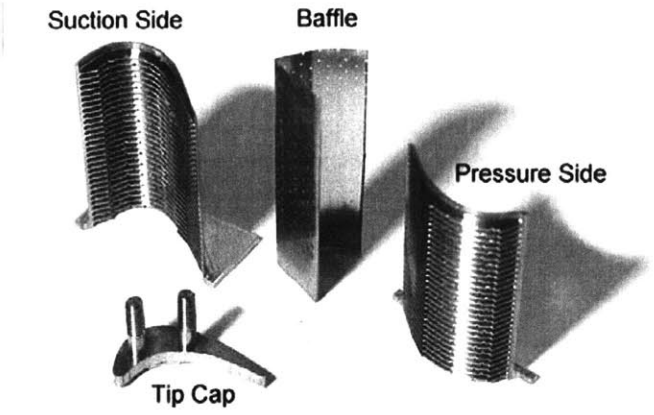

Figure 2-2 Pressure side, suction side, baffle and tip cap of blade model

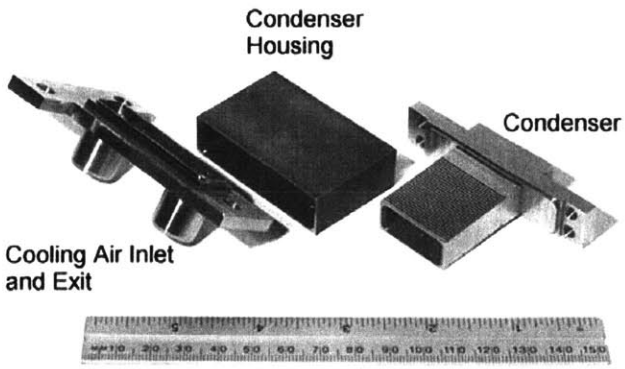

Figure 2-3 Condenser, Condenser Housing and Base Plate

A schematic of the shelf cross-section is shown in Figure 2-4. There are nine overflow ports in each shelf that allow the coolant to flow to the next radially outward shelf. The overflow ports are offset from shelf to shelf to prevent a continuous stream of liquid flow to the tip, bypassing the shelves. A baffle that matches the internal contour of the shelves when installed was also used to prevent the liquid from flowing directly to the tip without being distributed in the shelves. The baffle (also shown in the center of the photograph in Figure 2-2) has six vapor ports at each radial shelf location to allow the evaporated potassium to flow into the center port

of the blade. The purpose of the baffle is to ensure that the liquid coolant flows to the next radially outward shelf through the liquid overflow ports, and does not not by spill over the edge of the shelf and bypass the remaining shelves. The baffle extends 1.5 cm beyond the hub of the blade into the condenser. The baffle wall sits directly against the edge of the shelves and ensures that liquid flowing from one shelf to another goes through the liquid overflow ports.

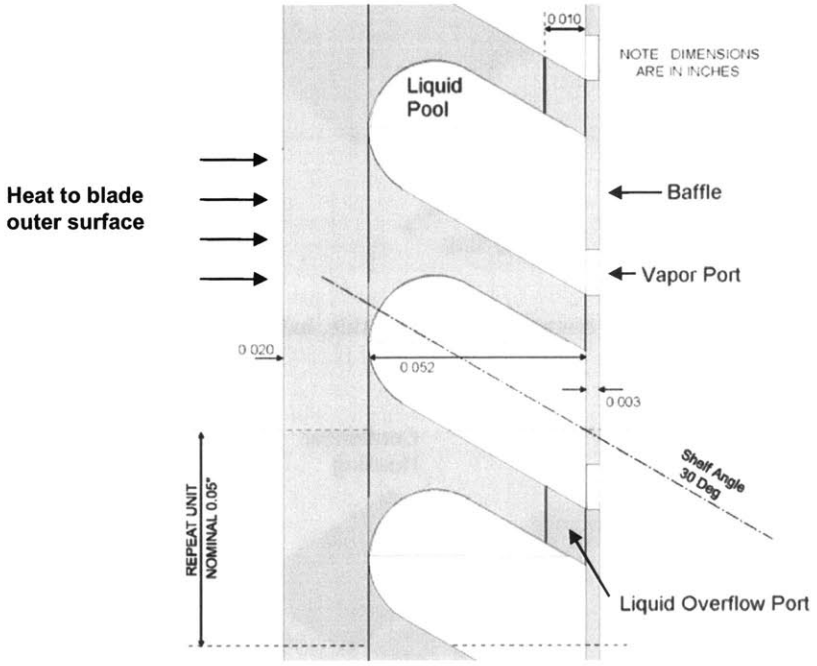

Figure 2-4 Shelf Detail

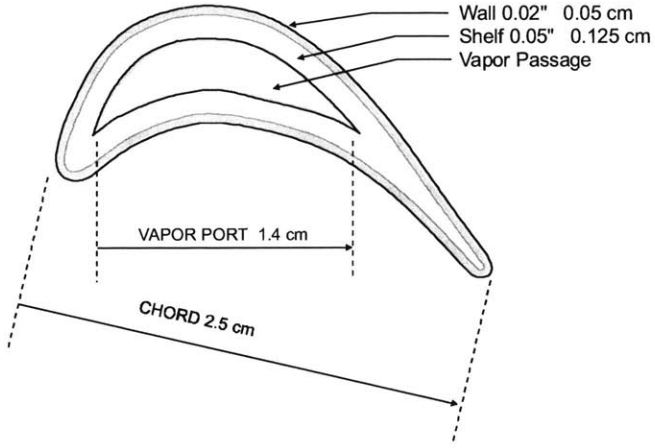

Figure 2-5 Blade Model Geometry and Nominal Dimensions

The blade contour was selected to represent current turbine engine blade technology and is shown along with some nominal dimensions in Figure 2-5. The nominal blade skin thickness is 0.05 cm (0.02 in). The actual blade skin thickness varies around the perimeter of the blade in order to allow the resistive heating to create a heat flux profile similar to that found in modern gas turbine engines. The heat flux profile as a percentage of average blade heat flux for a high performance turbine blade and the variation in blade skin thickness are shown in Figure 2-6.

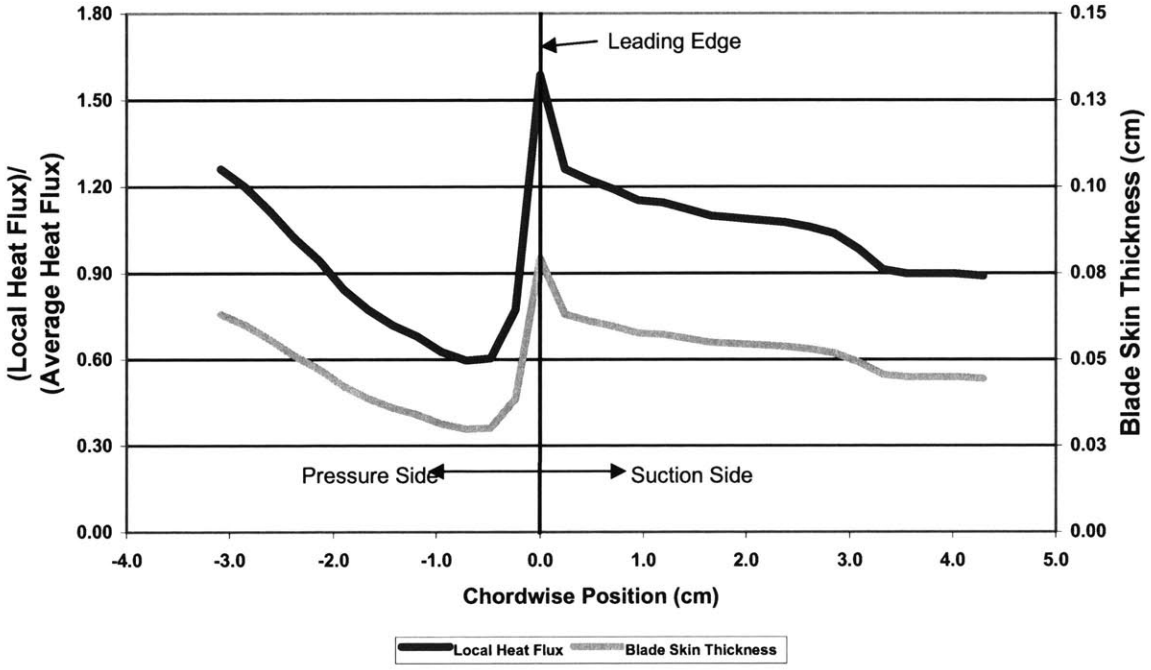

Figure 2-6 Local Heat Flux and Blade Skin Thickness Variation (Reference [25])

The vapor-liquid transport process is illustrated in Figure 2-1. Liquid potassium flows up the condenser walls under the motivation of rotational acceleration and into the blade. The liquid fills each shelf and then flows through the liquid overflow ports to fill the next shelf, and continues filling all the shelves up to the tip of the blade. Liquid evaporates from the shelves and the vapor flows through the vapor ports in the baffle and then flows radially inward through the blade center port and is condensed on the condenser walls. Cooling air flow enters the condenser housing, flows through the small air passages along the two sides of the condenser and out on the opposite side.

2.2.2 Rotating Heat Transfer Rig

All experimental work took place in the Rotating Heat Transfer Rig at the Gas Turbine Laboratory at the Massachusetts Institute of Technology. This facility has been used for numerous turbine cooling studies over the past 25 years. [22, 23, 24] Photos showing the experimental set-up and a schematic of the rig are shown in Figures 2-7, 2-8, and 2-9. The blade model is mounted on the end of a rotating arm with the appropriate counterweights on the opposite end. The rotor arm is enclosed in a large tank which can be evacuated to a pressure of 10^{-4} torr. This eliminates windage losses, minimizing the shaft power required to drive the unit, and avoids convective heat transfer from the test hardware.

2.2.2.1 Electrical Power System

A variable voltage supply is used to provide power to heat the blade model. The heating power current passes through isolated terminals in the tank wall and then through a set of carbon slip rings to the rotating arm. Four transformers in parallel convert the high voltage, low current input to a low voltage, high current output suitable for heating the nichrome blade. Two transformers are mounted on each side of the rotating arm and are visible in Figure 2-8. The power system is capable of delivering a heat flux to the blade that a first stage turbine blade would be exposed to in a gas turbine engine. The primary input current was measured using a shunt located just outside the rig vacuum wall.

The current input is delivered to the blade via copper straps. In the original power delivery system, the copper straps from the transformers were connected to a copper tip plate which was maintained in physical contact with the tip of the blade by clamping the plate down on the blade tip via two tightening nuts. The contact resistance between the copper tip plate and nichrome blade tip, however, was found to be much higher than expected resulting in a limit on the maximum power delivered to the blade. A new copper tip cap was then made with a cavity that fit over the tip of the blade. With the tip cap in place and the blade inverted, the cavity was filled with molten silver-tin solder. This system, referred to as the "solder bathtub", allows for a

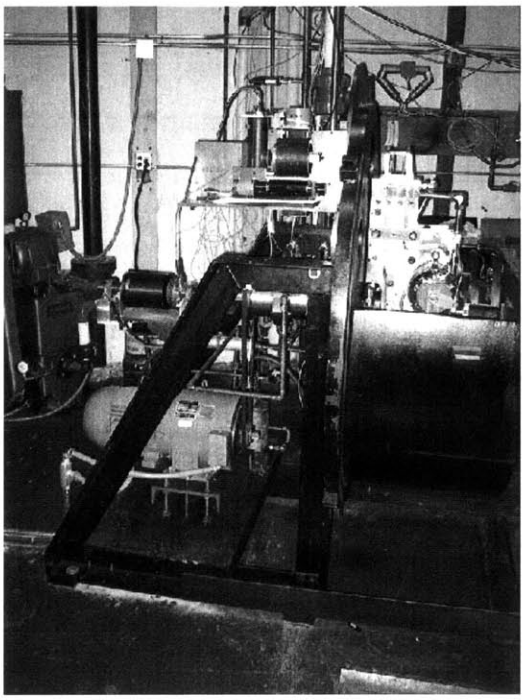

Figure 2-7 Rotating Heat Transfer Rig

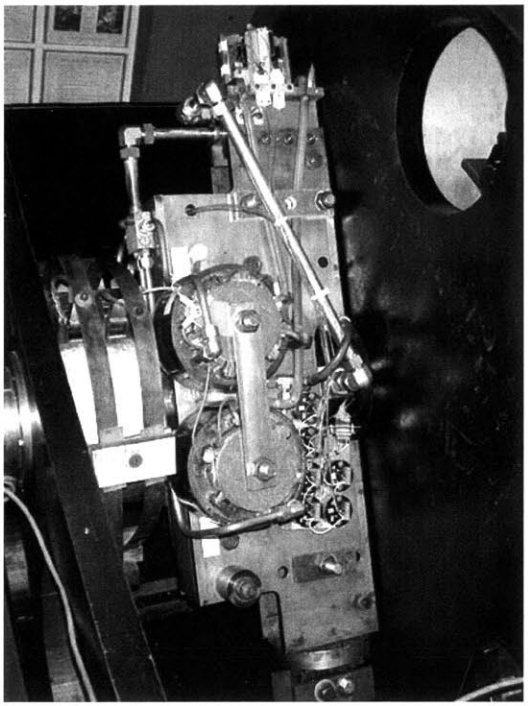

Figure 2-8 Rotating Arm and Transformers

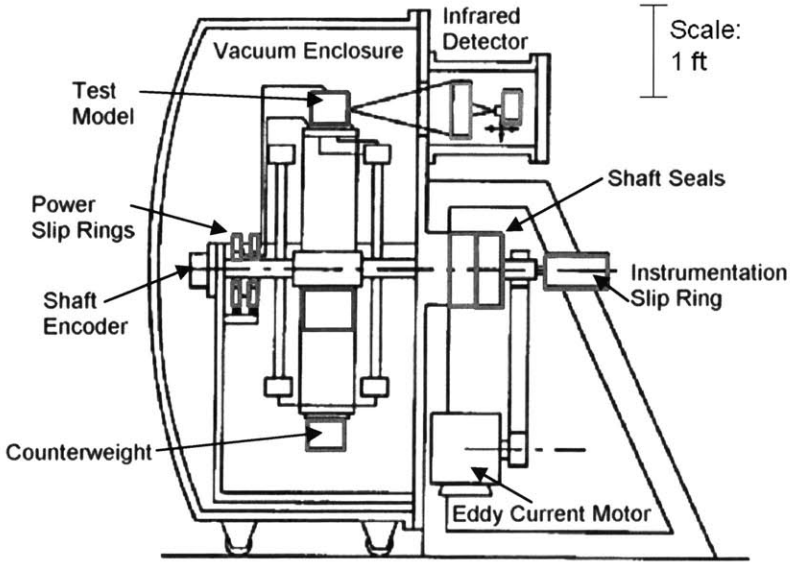

Figure 2-9 Schematic of Rotating Heat Transfer Rig

low resistance current path through the copper to the solder to the blade. As the blade heats up the solder melts but stays in the "bathtub" due to centrifugal force from the rotational motion. This system also reduces the stresses on the blade. The copper tip cap is maintained in place using the copper straps and an additional stainless steel support beam across the top.

2.2.2.2 Speed Measurement and Control System

A BEI optical encoder mounted on the end of the shaft is used to measure the rotational speed and angular position. The rotor speed is regulated using an eddy current motor and controller. A LabView routine continuously measures and controls the speed of the rotating arm to within ± 0.1 RPS during a run. The rig was originally designed to run at speeds up to 30 RPS. However, the highest speed attained during balancing was 15 RPS. The rig was run successfully up to 16.5 RPS during testing without deleterious effects to the blade or instrumentation. Typical speeds for a gas turbine engine are 150 – 200 RPS.

2.2.2.3 Blade Surface Temperature Measurement

The blade surface temperature is measured as a raster scan over the surface of the blade. The sensor is an Electro-Optical Systems HgCdTe infrared temperature sensor used in previous studies. The IR sensor is contained in a chamber adjacent to the chamber enclosing the rotating arm and is mounted on a two-axis movable platform. Two stepper motors are used to locate the sensor in relation to the blade model as it passes by the open viewing window between the two chambers. The horizontal distance between the IR sensor and the blade is set at the optimal focus location at the beginning of a run and is not moved once the run has begun. The vertical stepper motor is exercised throughout the run to collect data over the entire blade surface from hub to tip. A constant feed of liquid nitrogen through the vacuum wall of the IR chamber is used to maintain the detector at the operating temperature of 217 K.

The BEI encoder index is set at an angular location such that it triggers the IR data acquisition just before the blade model reaches the viewing window. A telescope consisting of two spherical mirrors located on the IR platform focuses the signal from the blade onto the IR detection aperture. The IR system measures the incident radiation from a nominal area of 1 mm^2 on the blade surface. Two flat mirrors positioned on either side of the blade at 45 degree angles from the blade chord provide an optical path covering the entire blade perimeter on each

rotational pass. Further description of the IR system and telescope including the focusing and calibration procedures can be found in Appendix A.

2.2.2.4 Condenser Temperature Measurement

The condenser housing was originally fitted to handle four Omega Type K small gage thermocouples spaced along the length of the condenser. Due to constraints on the number of signals that could be wired through the slip rings in the rotating shaft, only three thermocouples were installed. The location of the thermocouples is shown in Figure 2-10.

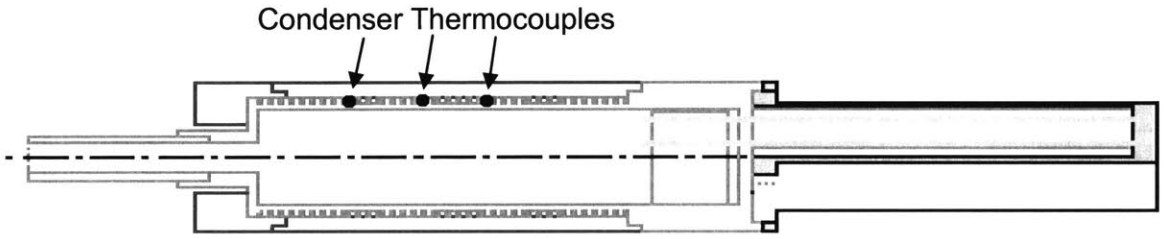

Figure 2-10 Condenser Thermocouple Locations

2.2.2.5 Cooling System

Cooling air enters the rig through a series of shaft seals. The cooling air is used to cool both the blade model and the transformers. The cooling air flow rate is measured using a Micromotion Flowmeter located outside the rig. A bypass valve located at the end of the rotating arm near the blade model was used to limit the cooling air flow to the blade. For all test runs, the valve was set to bypass cooling air and therefore an accurate measurement of cooling air flow rate to the condenser is not available, although the upper bound is determined from the measurement. Two Type K thermocouples were used to measure the inlet and exhaust temperature of the cooling air into the condenser. The air pressure was measured using an Omega PX303-100G5V pressure transducer.

2.2.3 Data Acquisition System

A PC data acquisition computer running LabView was used to collect and process the data. The list of parameters monitored and recorded during each run is shown in Table 2-1.

With the exception of the rotational speed and the blade surface temperature, all signals are first converted to 0 – 5 V signals using Analog Devices 5B Signal Conditioners. The analog to digital conversion is performed by a Measurement Systems 16 bit data acquisition board. Processing, recording and plotting of signals is done in the LabView environment. The speed signal from the encoder is processed using a Measurement Computing Encoder board. The IR signal is processed using a Measurement Computing 12 bit data acquisition board with burst mode capability to 140 MHz.

All parameters with the exception of the blade surface temperature are recorded continuously throughout a test run. The blade surface temperature is recorded as commanded by the user during the run.

Table 2-1 Parameters Monitored During Each Run

Parameter	**Symbol**	**Units**
Rotational speed	RPS	RPS
Cooling air temperature into rig	$T_{air,in}$	K
Cooling air temperature out from rig	$T_{air,out}$	K
Air flow rate	$\dot{m}_{air}$	kg/s
Air flow pressure	P_{air}	psia
Current to rig	I_{rig}	A
Voltage through blade model	V_{blade}	V
Condenser temperatures	T_{c1}, T_{c2}, T_{c3}	K
Blade base temperature	$T_{blade,base}$	K
Blade surface temperature distribution	T_{blade} (matrix of values as a function of span and chord location)	K

2.3 Experimental Procedure

A test run is defined as rig startup, a series of changes to rig speed, power to blade, and cooling air flow rate, data collection at various operating conditions, and rig shutdown. The Startup and Shutdown Checklists can be found in Appendix B. Typically, once the Startup

Checklist was completed, the rig rotational speed was ramped up to 5 RPS, at which point the power level to the blade was set at a low level between 50 – 150 W. The speed was then ramped up to 10 RPS where several scans of the blade surface temperature were taken. Finally, the speed was ramped up to 15 RPS, the speed at which the major portion of each run was conducted. During rig balancing, a vibration mode was detected at approximately 12 – 13 RPS, so sustained operation at those speeds was avoided. Once 15 RPS was reached, more scans of surface temperature were taken. The run would then proceed with increases in the power level to the blade followed by several blade surface temperature scans. Initial runs showed that the blade started glowing a dull red around 1000 K and it was decided that blade temperature levels above 1030 K (1400 F) were unacceptable for the experimental work. If the blade surface temperature reached 1030 K (1400 F), the cooling air flow was turned on or increased to reduce the blade the temperature. The controlled and measured rig parameters for a typical run (Run 12) are shown in Figure 2-11.

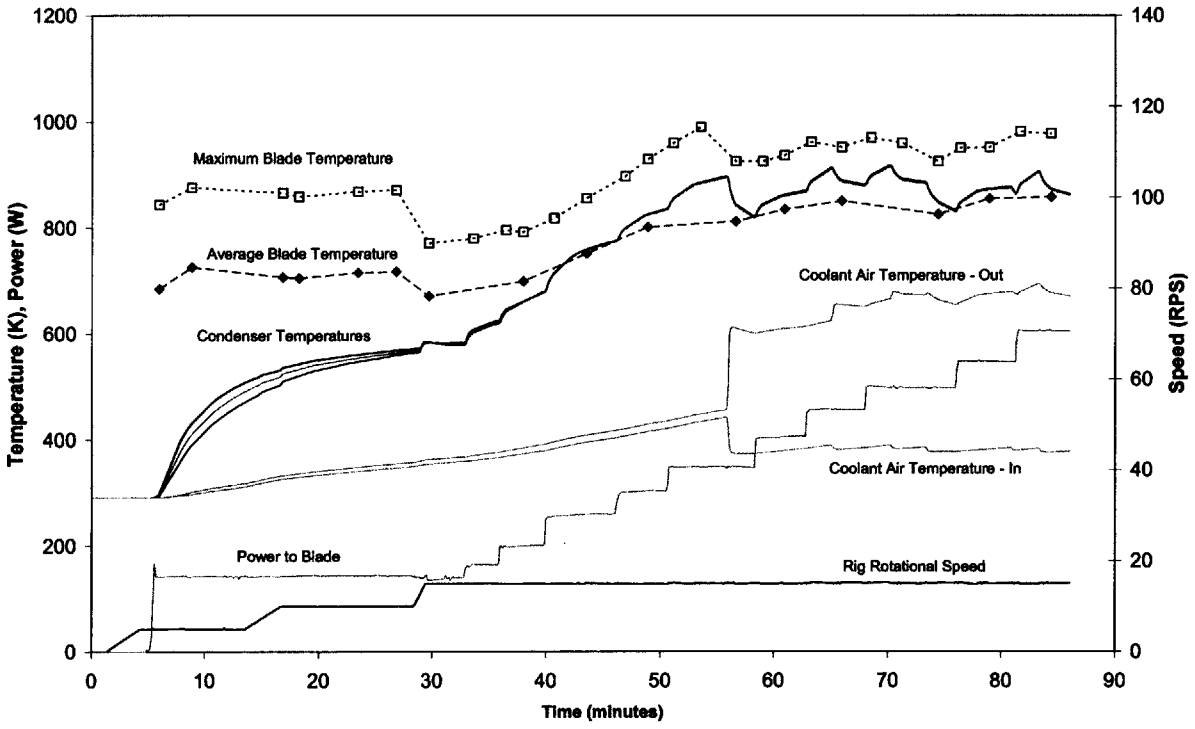

Figure 2-11 Measured and Controlled Run Parameters for Run 12

A total of 19 runs were done with a total rig operating time of 27.7 hours. Several modifications to the rig apparatus were made during the testing. The first was the change in the electrical power delivery system to the blade described in Section 2.2.2.1. The "solder bathtub" was installed after Run 11 and was used for the remainder of the runs. A second modification was the removal of the copper ground strap connecting the hub of the blade to the rotating arm. The ground strap was removed after Run 14 and was not re-installed for the remainder of the runs. An unintended modification was a 6° tilt in the blade which was discovered after Run 13, the first run with the "solder bathtub." This new method included a more rigid method of clamping the copper power strap in place that may have been responsible for the deformation of the blade causing the tilt. Runs 13 – 18 were done with the tilt in place. The baseplate of the condenser was modified before Run 19 to correct the tilt in the blade (thereby introducing a 6° tilt to the condenser as a result). The effects of the ground strap and the blade tilt on cascade performance are explored in more detailed in Chapter 3, however, it should be noted that these effects were artifacts of the experimental set-up and would not occur in engine operation.

In Runs 1 – 6 and Run 15 the rotational speed levels were low enough that cascade operation did not occur. A table of conditions at which blade surface temperature scans were recorded for the remainder of the runs can be found in Appendix C.

2.4 Data Reduction

2.4.1 Current and Power

The blade current and voltage were measured continuously during each run and were converted to power using a previously determined calibration curve. The calibration was performed by measuring the primary current into the rig, I_{rig}, at the rig exterior wall and the secondary current through a mock-up model of the blade, I_{blade}, mounted on the end of the rotating arm. A linear curve was fit to the data and the resulting calibration equation is

$$I_{blade} = 35.85 I_{rig} . \tag{2.1}$$

The total power (also referred to as the uncorrected power) to the blade is determined using I_{blade} and V_{blade}:

$$P = V_{blade} I_{blade} \tag{2.2}$$

The radiative loss from the blade is determined using the reduced IR data. Each individual temperature measurement on the surface of the blade represents an area, A_{scan}, of 1.0 mm by 0.5 mm. This area will vary slightly depending on the blade view angle, but the error should average out over the entire surface of the blade, especially since the blade surface temperature is nearly constant. By summing the individual radiation losses at each scan location over the entire surface of the blade, an estimate of the corrected power which takes into account the total radiation loss can be made:

$$P_{corr} = P - \sum_{A_{scan}} \sigma A_{scan} T^4 \tag{2.3}$$

At the range of powers tested, the radiative heat loss is not negligible. The corrected power represents the power available to be transported by evaporative cooling. The average heat flux to the blade can then be determined using the total surface area of the blade, A_{blade}:

$$q = \frac{P_{corr}}{A_{blade}} \tag{2.4}$$

Due to the variances in wall thickness, the local heat flux varies as a function of the perimeter around the blade. There is no intentional spanwise variance in local heat flux, although there will be some variance due to the temperature profile driven by conduction across the span of the blade.

2.4.2 Infrared Detector Output

The blade surface temperature measurements were converted from voltage to temperature during the runs using previously determined calibration curves and plotted in LabView after each scan to provide an immediate visual temperature map of the blade. The calibration relating radiation collected by the IR detector (measured in terms of voltage) and the corresponding blade surface temperature is:

$$T = \left(1.503\times10^{8} V_{IR}^2 + 4.959\times10^{9} V_{IR} + 1.697\times10^{10}\right)^{1/4} \tag{2.5}$$

Because the speed control is disabled during the 1 - 2 minutes that the infrared detector is reading the radiation from the blade, some of the scan lines are shifted a distance related to the variations in speed (±0.1 RPS) during the scan. Following each run, the shifted scan lines were manually lined up with the rest of the data. The voltage data was then reduced a second time to

produce clearer versions of the temperature maps taken during the run. The listing of the Matlab code used to reduce the IR voltage data after the run is given in Appendix B. The purpose of the data reduction code is to convert the voltage data to temperature and to plot the resulting surface temperature maps in a meaningful way. A typical blade surface temperature plot is shown in Figure 2-12. The suction side and pressure side are delineated by the vertical lines and the leading edge, trailing edge, hub and tip are identified.

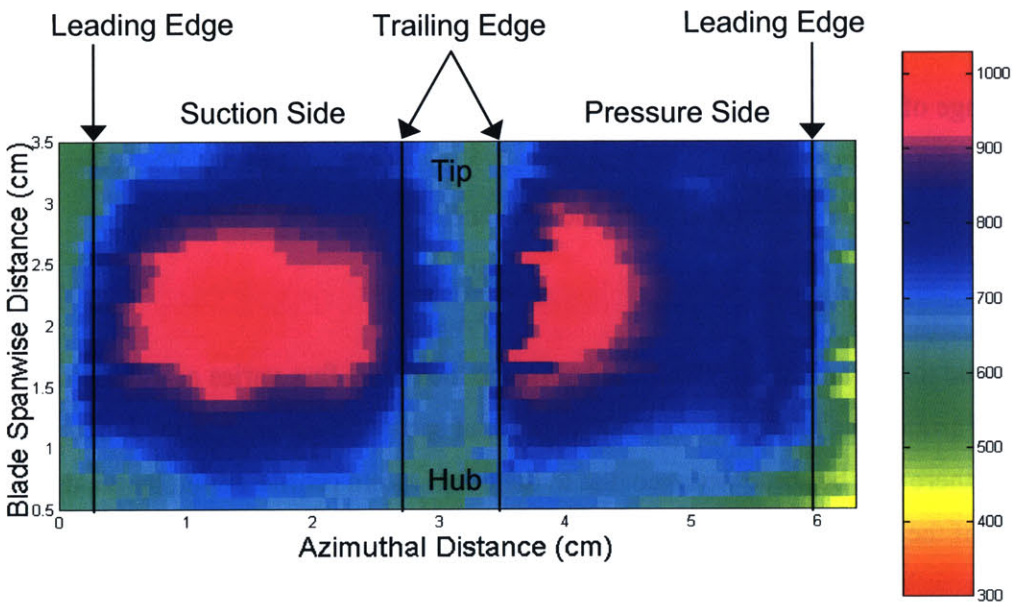

Figure 2-12 Blade Surface Temperature Plot

Chapter 3 Experimental Results

3.1 General Results and Observations

The first result is that the Return Flow Cascade functioned as it was conceived to, in a turbine blade geometry with potassium as the coolant. Proper functioning was clearly distinguishable by a near-uniform blade temperature. A spanwise conduction profile, with a hotter region at mid-span and cooler hub and tip was measured when the cascade was not functional. It was found that there is a rig rotational speed below which the Return Flow Cascade does not effectively cool the blade, in approximate agreement with modeling predictions. No high heat flux limit, traceable to the cascade performance, was reached during testing. Blade tilt adversely affected the cascade performance by limiting liquid coolant distribution on one side of the blade. The result was one side of the blade operating at a near-uniform blade temperature while the other side exhibited a spanwise conduction profile.

Experimental results show that the Return Flow Cascade can maintain the blade temperature at a nearly constant level in a typical turbine blade geometry with potassium as the coolant. For the purposes of analyzing the data, the phrase "maintains a nearly constant blade temperature" refers to a case where the standard deviation of the average temperature distribution over the blade is less than 50 K (90 °F) around a base temperature of approximately 800 K (980 °F). Successful operation was shown at rotational speeds ranging from 10 to 16.5 RPS (radial acceleration of 200 to 550 G) and at an uncorrected power level of 605 W, corresponding to a maximum blade average heat flux of 18.8 W/cm^2.

3.2 Initiation of Cascade Operation

Cascade initiation refers to the point at which the Return Flow Cascade begins to effectively dissipated the heat supplied to the blade. The point of cascade initiation is characterized by a large drop (50 – 100 K) in blade average temperature, an increase (20 - 40 K) in condenser temperature and a distinct change in the blade temperature distribution from a "conduction profile" to a "cascade profile." The experimental work has shown that there is a low rotational acceleration threshold for initiation of cascade operation. During the runs the

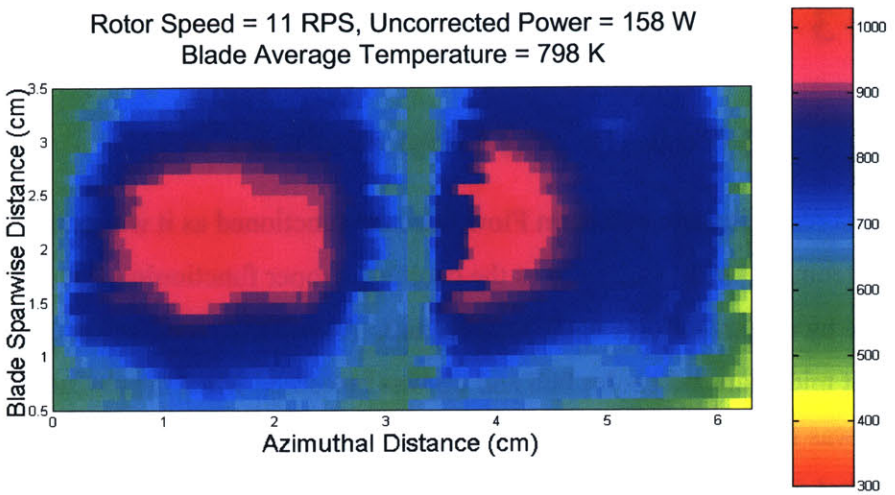

Figure 3-1 Blade Temperature Distribution (K) with "Conduction Profile" (Run 7-37)

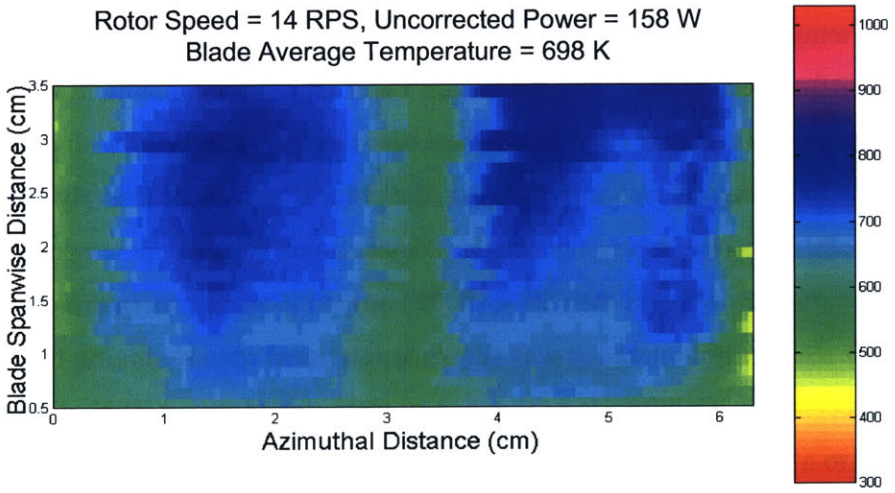

Figure 3-2 Blade Temperature Distribution (K) with "Conduction Profile" (Run 7-37)

blade surface temperature was recorded at speeds of 5, 10, and 15 RPS. For the majority of the runs cascade initiation did not occur at speeds lower than 15 RPS. An example of cascade initiation is illustrated in Figures 3-1 and 3-2. The blade surface temperature in degrees Kelvin is shown for both the suction side and the pressure side of the blade and is represented by a color

bar shown on the right side of the plot. The hub, tip, leading edge, and trailing edge are labeled on Figure 2-12 for reference. Each plot represents a full IR scan of the blade surface taken over a 1 - 2 minute period.

The blade temperature distribution shown in Figure 3-1 is from Run 7 and is typical for an electrically heated blade with little or no cooling. This is referred to as a "conduction profile." The maximum surface temperature is at the mid-span of the blade and the hub and tip are cooler. The IR scan shown in Figure 3-1 was taken at a rotational speed of 11 RPS and an uncorrected power of 158 W. The speed was then increased from 11 RPS to 14 RPS at a constant uncorrected power and a second IR scan was taken 3 minutes later, shown in Figure 3-2. The temperature distribution in Figure 3-2 is typical when the cascade is operating as intended. The average blade surface temperature is much more uniform and is 100 K cooler than before cascade initiation.

A complementary method of presenting the blade temperature maps is to look at one chord-wise location, specifically the mid-chord of the suction side of the blade. On the temperature maps shown in Figure 3-1 and 3-2, this means tracing the temperature along a line from hub to tip at an azimuthal distance of 1.5 cm, to highlight the radial variation. The condenser temperatures are added to this plot to illustrate the temperature profile from the bottom of the condenser to the tip of the blade. The mid-chord suction side temperature profile for the Run 7 cascade initiation is shown in Figure 3-3. The dotted line connecting the condenser and blade temperatures does not represent the actual temperature profile between the measured condenser temperatures and the blade hub. Error bars are shown for the condenser temperature measurements (± 4.3 K) and for the blade temperature measurements (± 18.2 K). The error and uncertainty analysis can be found in Appendix E.

The transition from a conduction profile to cascade operation is evident in the shape of the curves in Figure 3-3. The blade temperature decreased and became more uniform and the condenser temperature increased, reflecting a greater flow of vapor to the condenser. The depression in temperature at the blade hub is due to an unforeseen heat transfer path by the placement of the resistive heating ground strap and is covered in more detail in Sections 3.5 and 4.7.

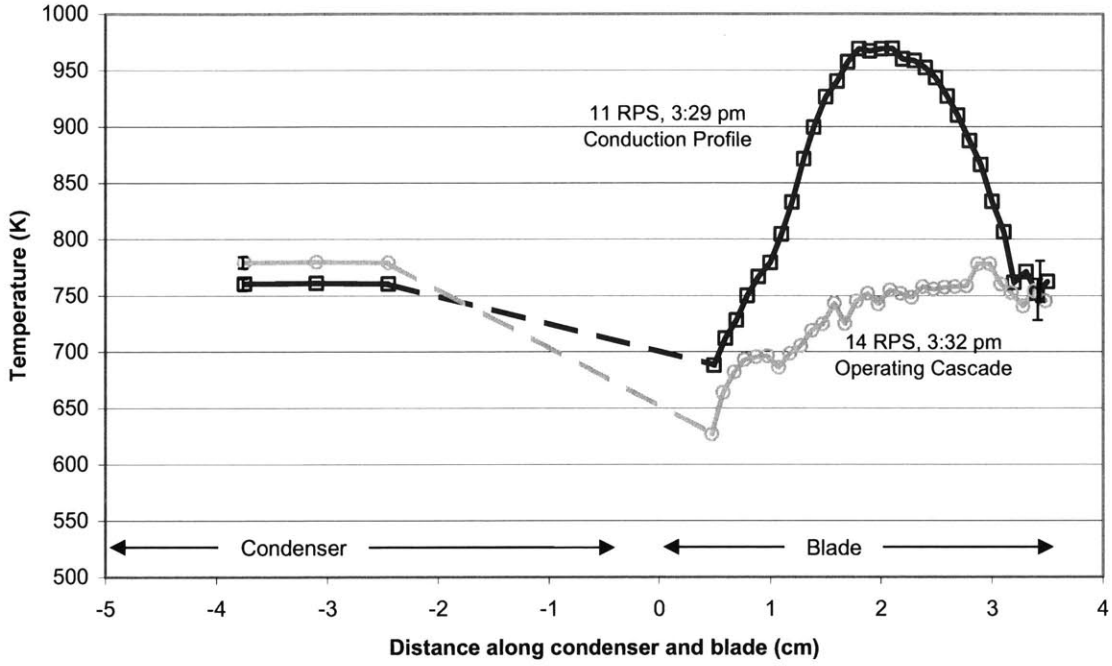

Figure 3-3 Mid-chord Suction Side Temperature Profile
Cascade Initiation for Run 7, Uncorrected Power = 158 W

A summary of the conditions at initiation of cascade operation for each experimental run is shown in Table 3-1. The data for Runs 7 – 13 shows that cascade operation initiated at 14 RPS or higher, and at average blade power levels of 150 – 200 W.

Cascade initiation occurred in two ways. The first is initiation during or immediately after an increase in rig rotational speed to 15 RPS. The power to the blade was constant during the initiation. The second type of transition occurred at a constant rotational speed of 15 RPS and constant power to the blade. In this case, the speed was increased to 15 RPS, but initiation did not occur during or immediately after the increase. Instead, intiation occurred spontaneously some time later. The only blade parameters changing would have been condenser temperature and blade tip temperature. It is therefore postulated that there are two limits on cascade operation. The first is a liquid flow limit in the shelves which would become less significant as speed increased. The second is choking in the vapor port which would be dependent on the

temperature of the vapor. Both of these limits are explored in Chapter 4, Modeling and Performance Analysis and include comparisons to the test data.

Table 3-1 Conditions at Initiation of Cascade Operation

	Speed (RPS)	Uncorrected Power (W)	Condenser Temperature (K)	Ground Strap Installed?	Blade Tilt Evident?
Run 7	14	159	780	Yes	No
Run 8	15	134	655	Yes	No
Run 9	15	102	610	Yes	No
Run 10	15	195	722	Yes	No
Run 11	15	207	696	Yes	No
Run 12	15	138	584	Yes	No
Run 13	15	175	637	Yes	No
Run 14	10	170	562	Yes	Yes
Run 16	10	141	533	No	Yes
Run 17	10	104	475	No	Yes
Run 18	5	115	401	No	Yes
Run 19	15	161	668	No	No

3.3 Effect of Condenser Cooling Air Flow Rate

As discussed in Chapter 2, the air flow rate used to cool the condenser was not measured directly. Also, the flow rates used to cool the condenser at the low power levels tested were below the range of the flowmeter. The cooling air flow is therefore presented on the blade temperature scans as either "ON" or "OFF." When the cooling air flow was off, the condenser was cooled by conduction to the rotating arm. This was sufficient for uncorrected power levels up to about 300 W.

An example of the effect of cooling air flow on the blade surface temperature is shown in Figures 3-4 and 3-5. Figure 3-11 is a scan from Run 9 at an uncorrected power level of 205 W and an average blade surface temperature of 812 K. Cooling air flow was turned on and then

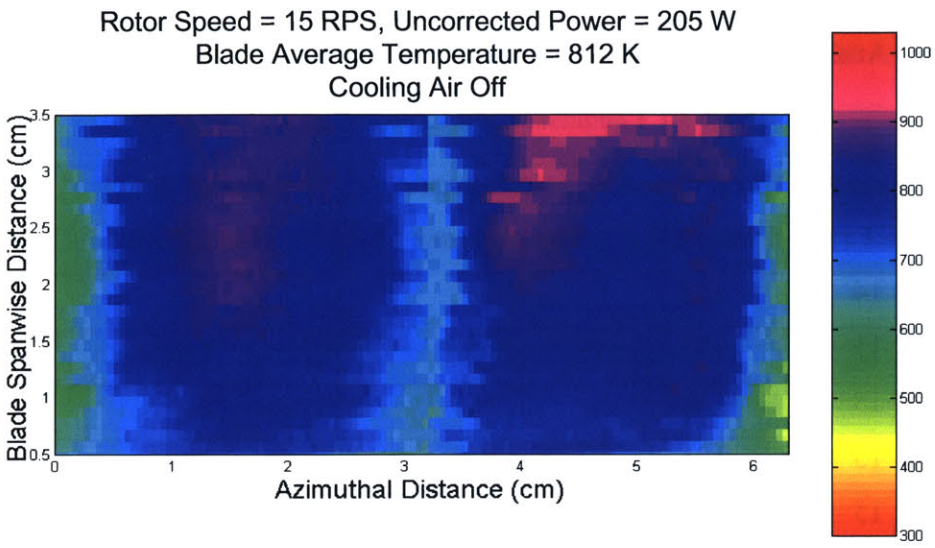

Figure 3-4 Blade Temperature Distribution (K), Cooling Air Flow Off (Run 9-9)

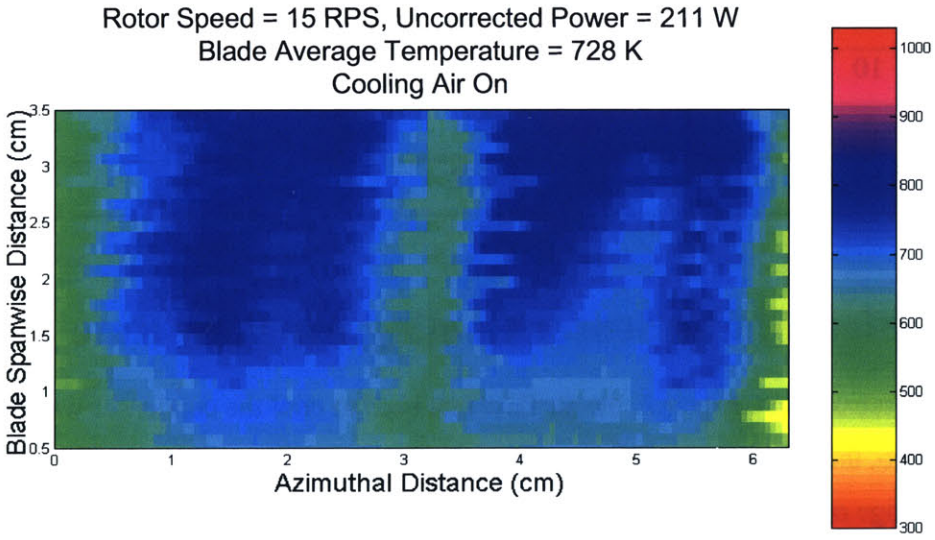

Figure 3-5 Blade Temperature Distribution (K), Cooling Air Flow On (Run 9-10)

increased just to the point where the condenser temperatures could be observed to decrease. Figure 3-5 shows the scan taken 3 minutes later with the condenser air on. The average blade surface temperature decreased by 84 K to 728 K. The condenser temperatures decreased over 100 K, from 876 K to 749 K. The cooling air had the desired effect of lowering the blade surface

temperature. Assuming that there are no restrictions on vapor flow into the condenser (as will be discussed in Chapter 4) the blade surface temperature can be controlled by adjusting the condenser cooling rate. The increased condenser cooling lowers the vapor pressure in the condenser and in the blade. The temperature at which the liquid evaporates decreases and therefore the blade surface temperature drops as a result.

3.4 Heat Flux Threshold

The heat flux to the blade was limited by several factors. Initially, the heat flux was limited by the power supply and the power delivery system to the blade. Both of these were modified to allow for blade power delivery levels up to 3 kW. The final limit is the temperature of the blade. Before the blade became tilted, a power level of 605 W was reached with a maximum blade surface temperature of 975 K (1300 F). In runs where the blade was tilted, the blade temperature limit of 1030 K was reached at lower power levels. Unfortunately, when the tilt and the ground strap were removed, the blade failed before higher power levels could be achieved. The potential high power limit of the blade design was thus not reached during the testing.

3.5 Effects Specific to Experimental Apparatus

Effective cascade operation as shown in the surface temperature maps in Figures 3-2, 3-4, and 3-5 was observed for the majority of the tests. There were, however, several effects related to the experimental apparatus which prevented effective cooling of the blade. While these effects are not expected in engine operation, they are useful for eliciting a better understanding of the internal flow processes of the Return Flow Cascade.

3.5.1 Excessive Hub Cooling by Ground Strap

The ground strap was originally intended to create an electrical conductance path from the base of the blade to the rotating arm, preventing excess heating of the condenser through resistive heating. The ground strap is shown as installed on the condenser and blade assembly in Figure 3-6. An unintended consequence was that the ground strap also created a substantial thermal conductance path from the hub of the blade. As a result, the hub temperature for those

runs where the ground strap was installed, shown in Table 3-1, was lower than the blade tip and condenser temperatures. This effect is shown for three different runs at 15 RPS and an uncorrected power of 300 W in Figure 3-7, where the mid-chord suction side temperature profile and the condenser temperatures are shown for scans taken in Runs 10, 12, and 16. The dip in hub temperature seen in Runs 10 and 12 is caused by conduction through the ground strap. The data shows that this prevents adequate cascade cooling over the span of the blade. The temperature profile for the Run 10 data on the plot indicates that there is an area near the tip of the blade where cascade cooling is not dissipating the heat from the resistive heating. Once the ground strap was removed, the temperature gradient at the hub decreased and the temperature was more uniform over the entire span of the blade as seen for Run 16.

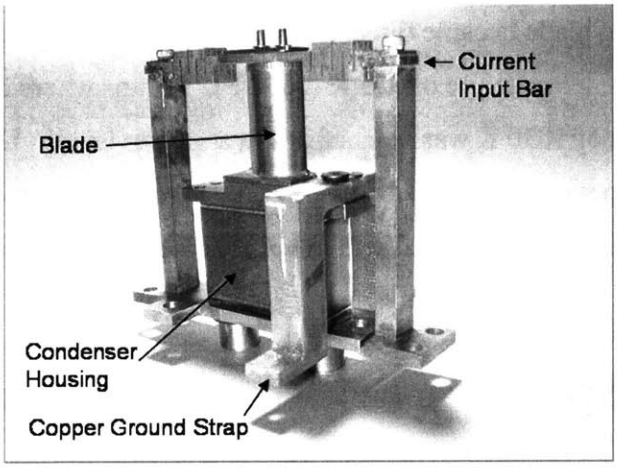

Figure 3-6 Photograph of Copper Ground Strap Installation

A comparison of IR scans from Run 7 and Run 19 in Figures 3-8 and 3-9 at similar operating conditions clarifies this point. The effect of the ground strap is seen in Figure 3-8. The blade temperature is uniform over about ¾ of the span, but the hub is at least 100 K cooler than the rest of the blade. In Figure 3-9, the ground strap was removed and the blade temperature is nearly uniform over the entire span. These figures and the previous one illustrate that the blade-condenser cascade system can be operated with only a small drop in temperature from the tip of the blade to the condenser when the ground strap is removed. It should be emphasized that the ground strap is peculiar to this experimental set-up and would not be an issue in an engine design.

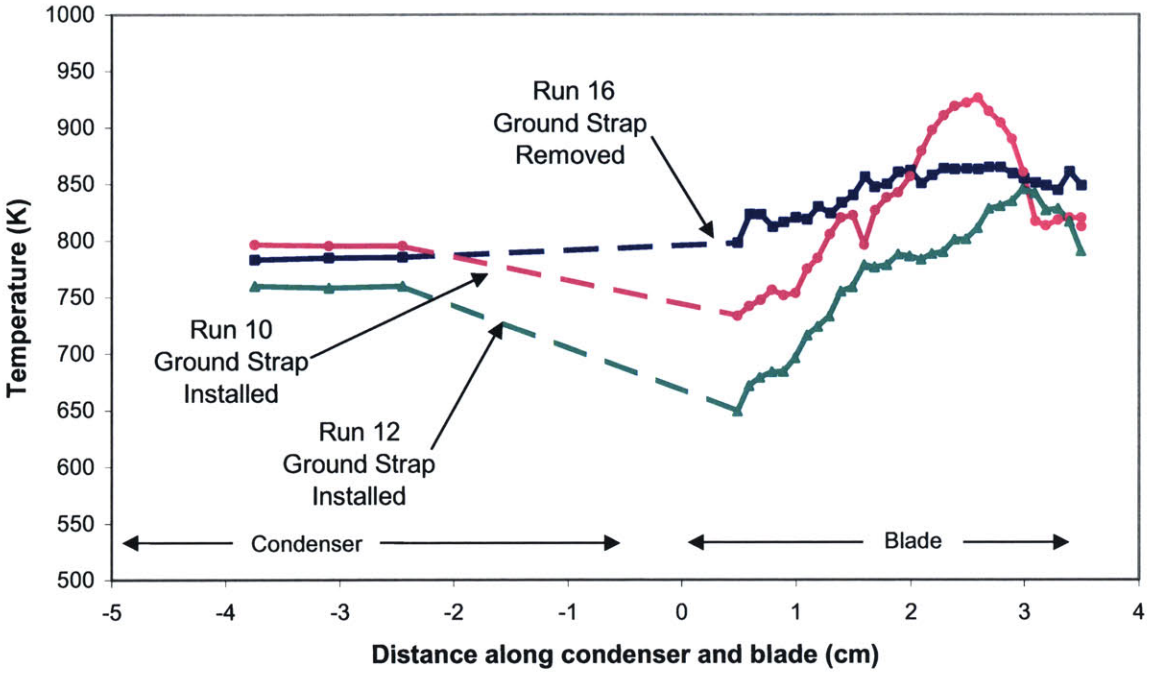

Figure 3-7 Mid-Chord Suction Side Temperature Profile, Uncorrected Power = 300 W, Comparison with and without Ground Strap Installed

Another effect that may have occurred but was not explicitly observed is recirculation of the vapor in the blade due to the cooled hub. When the ground strap is installed, it acts to conduct heat away from the hub of the blade and may maintain the hub at a temperature low enough for the flowing vapor to condense on the inner baffle wall. Only vapor that condenses on the condenser wall will be returned to the shelves. Any vapor that condenses on the internal baffle wall will flow directly to the tip, bypassing the shelves and possibly preventing effective cascade cooling.

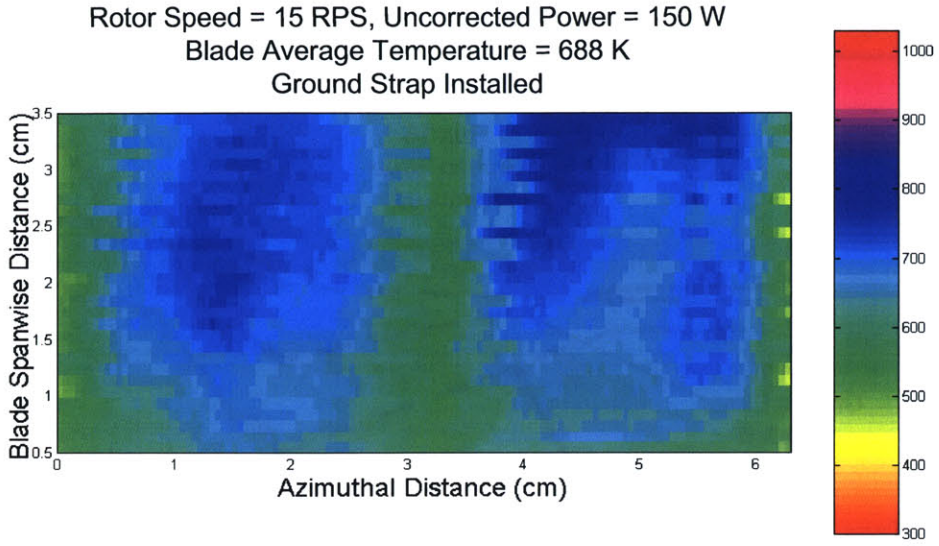

Figure 3-8 Post-Initiation Blade Temperature Distribution in degrees Kelvin, Run 7-47, Uncorrected Power = 150 W, Ground Strap Installed (Run 7-47)

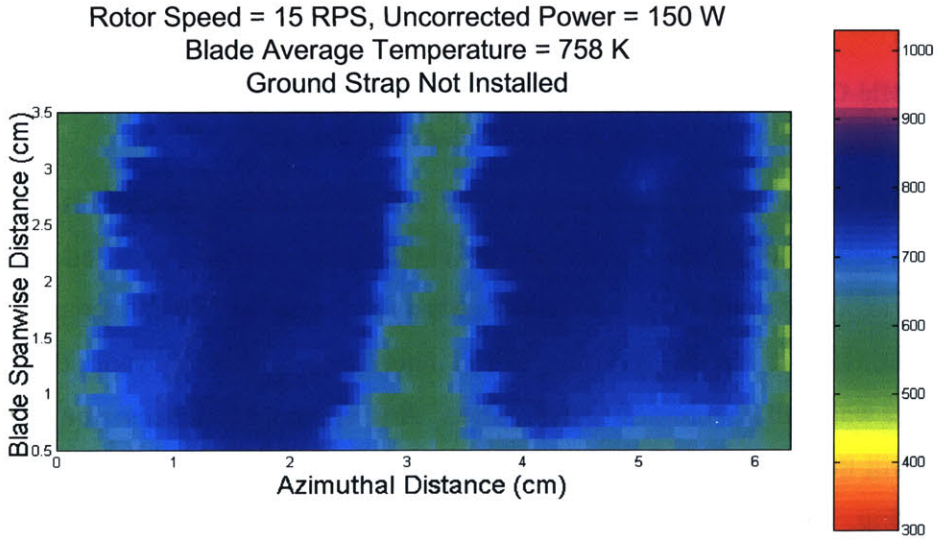

Figure 3-9 Post-Initiation Blade Temperature Distribution in degrees Kelvin, Run 19-12, Uncorrected Power = 150 W, No Ground Strap (Run 19-12)

3.5.2 Uneven Cooling due to Blade Tilt

Cascade initiation and operation were also affected by a tilt in the blade which was noticed during a visual inspection after Run 13. The blade was leaning towards the pressure side. Further inspection showed that there was a 6° tilt from the vertical, as shown in Figure 3-10. The blade tilt was present for Runs 14 through 18. The key characteristics of the tilted blade cascade behavior are that cascade initiation occurred at lower speeds, the transition was much more gradual, the suction side initiated before the pressure side and cascade operation was more effective on the suction side. It is possible that the blade became tilted gradually over a series of runs. The detrimental effects on cascade operation were only noticeable after Run 13.

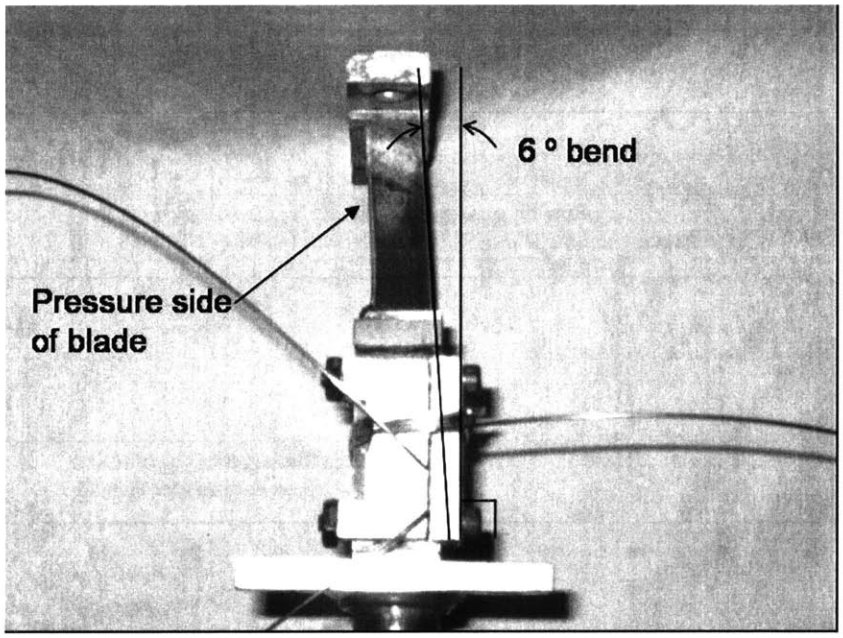

Figure 3-10 Photograph of Blade and Condenser Model with 6° Tilt

The blade surface temperature data for Runs 12 - 18 indicates that there is better cascade cooling on the suction side of the blade. Even if the cascade was operational on both sides of the blade, the pressure side was at a higher average temperature than the suction side. The blade tilt was removed by machining a 6° angle into the base plate for Run 19, and the blade surface temperature maps from this run show even, consistent cooling on both sides of the blade.

The temperature difference between the suction side and the pressure side of the blade is shown in Figure 3-11. The temperature difference for each scan of blade temperature is plotted

versus rig runtime. Temperature differences between ± 36 K (65 °F) were regarded as within the uncertainty range of the IR temperature measurement (± 18 K for each temperature measurement) and therefore cannot be regarded as an indication of uneven cooling. There are, however, temperature differences greater than ± 36 K between the two sides of the blade for Runs 12 through 18, the runs where the blade tilt was evident, with the pressure side having a consistently higher temperature than the suction side. The data for Run 19, where the tilt has been corrected, show temperature differences within the ± 36 K range again, indicating that the tilt was responsible for the excessive heating of the pressure side.

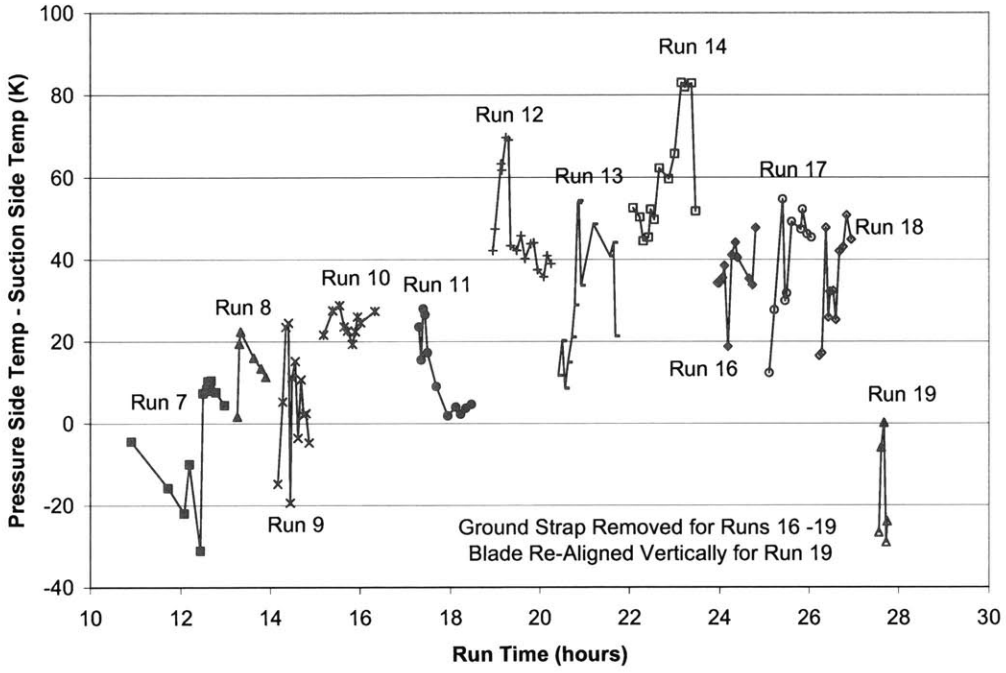

Figure 3-11 Temperature Difference between Suction Side and Pressure Side of Blade

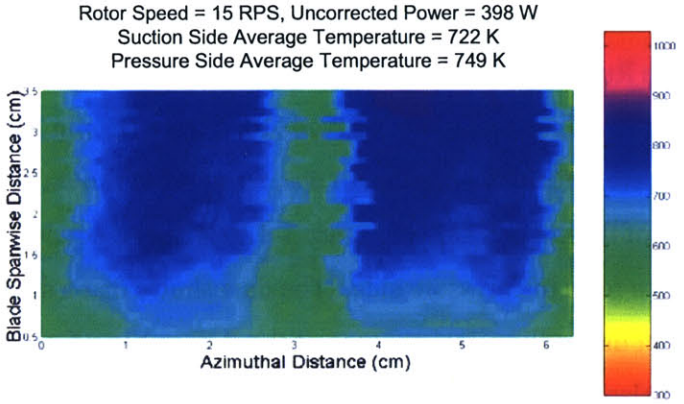

(a) No blade tilt, Uncorrected Power = 398 W

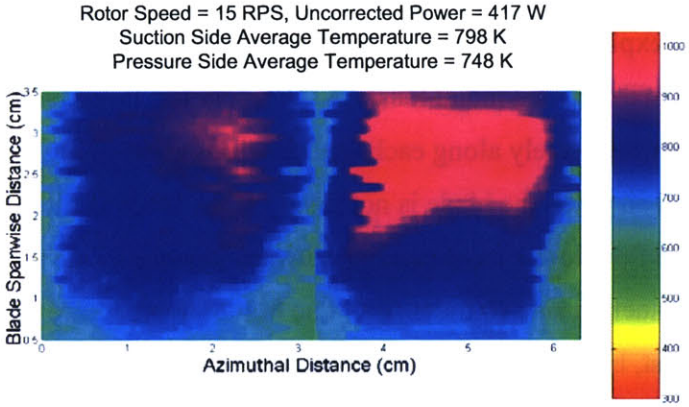

(b) Blade tilt, Uncorrected Power = 417 W

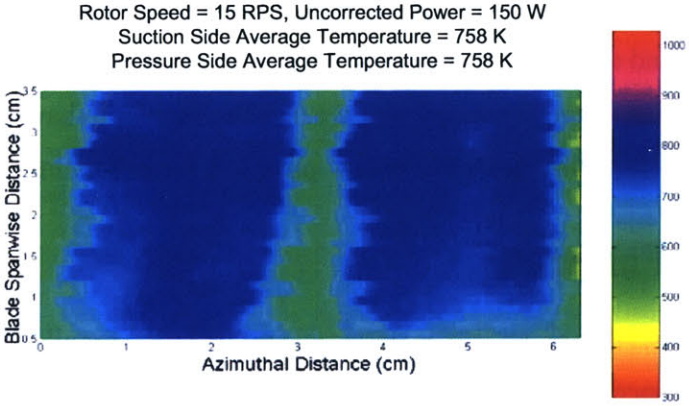

(c) **Blade tilt removed, Uncorrected Power = 155 W**

Figure 3-12 Blade Temperature Distribution (K) for Operating Cascade with and without Blade Tilt

An example of uneven cooling due to the blade tilt is shown in Figure 3-12. A blade temperature scan from Run 10 is shown in Figure 3-10a, where the blade is cooled evenly on both sides. The uneven cooling caused by the blade tilt from a scan in Run 14 is shown in Figure 3-12a and a final scan from Run 19 after the tilt was removed is shown in 3-12c. The heating near the trailing edge of the suction side in Figure 3-12b is due to conduction through the blade skin and shelf structure from the pressure side. The data shows that a small degree of blade tilt can significantly affect the cooling performance of the Return Flow Cascade.

The blade tilt also has an effect on the rotational rig speed at which cascade operation first occurs. As given in Table 3-1 Runs 14, and 16 – 18 had cascade operation begin at speeds of 5 or 10 RPS, compared to the rest of the runs that initiated at 15 RPS.

One possible explanation for these effects is as follows. When the blade is not tilted, each shelf is located at a constant radial location. When liquid flows radially outward from shelf to shelf, it also flows transversely along each shelf towards areas of higher heat flux, hence the even cooling that is seen when the blade is not tilted. If the blade is tilted, the liquid in the shelves would tend to flow to the most radially outward location. Due to the nature of the tilt this is located on the suction side of the blade. The hub of the pressure side of the blade may be cooled properly at first, but as the excess liquid flows radially outward, it will tend to flow towards the suction side of the blade and eventually the pressure side of the blade will receive little or no liquid for cooling resulting in the hot spot that is seen in Figure 3-12b.

As will be shown in Chapter 4, the liquid flow limit from shelf to shelf is a function of the rotational speed and the depth of the liquid pool. The tilted blade causes the liquid to flow towards the suction side of the blade and would cause the shelves to have a larger pool depth allowing the liquid to flow through the overflow ports at a lower rotational speed.

3.6 Blade Failure

Successful cascade operation was observed and recorded for all test runs beginning with Run 7. In each run, once the cascade initiated operation as indicated by a "cascade profile" on the blade surface temperature distribution, it did not revert back to the "conduction profile" unless the rotational acceleration was decreased. Even if the heat flux to the blade were increased, the blade would maintain a "cascade profile" although at a higher temperature. This

behavior was not observed during the last run, Run 19. Cascade operation began at a speed of 15 RPS and an uncorrected power of 161 W. Approximately 36 minutes into the run, there was a sudden 34 K decrease in condenser temperature. There was no cooling air flow to the condenser at this time. The blade surface temperature scans immediately after this drop in condenser temperature showed a return to a "conduction profile" even though the speed of the rig had not changed. During the rest of Run 19, no cascade cooling was observed.

A possible explanation for the sudden decrease in condenser temperature is if the blade or condenser surface were compromised resulting in a leak large enough to allow potassium vapor to leak out. The pressure inside the blade would have been higher than the tank pressure, which is evacuated down to a level of 10^{-4} torr. If some potassium vapor leaked out, the vapor pressure in the condenser would decrease and the condenser temperature would also decrease as a result. Once Run 19 was completed, the tank was allowed to pressurize back to room pressure. At this point air may have leaked into the blade and reacted with the potassium to form a solid superoxide which could block up the shelves and prevent liquid potassium from flowing radially outwards. A careful examination of the blade was done after Run 19 to determine where a leak might have occurred. The blade was disassembled after the run and was found to still contain potassium. The blade was cleaned and examined but no leak locations were found. The condenser was pressure tested for leaks but none were found. There was some difficulty in welding the pieces of the blade and condenser together at the beginning of the test program, especially in the area of the leading edge and trailing edge hub. Extra stress may have been put on these areas when the blade became tilted, and it is suspected that a leak could have originated in one of those location. However, the data and observations from Run 19 are the best evidence available to conclude that blade failure did occur.

Chapter 4 Modeling and Performance Analysis

4.1 Modeling Approach

In an evaporatively cooled turbine blade a liquid metal is exposed to high heat fluxes and high radial accelerations as it undergoes processes such as pool boiling, evaporation, condensation, and liquid and vapor flow. The complexity of the system is such that, for the purposes of this dissertation, in-depth modeling and analysis of only the critical heat flux for boiling and the vapor and liquid flow processes in the experimental blade model are presented. For each of the remaining processes (natural convection and evaporation in the shelves and condensation at the condenser wall) simpler analyses and qualitative reasoning will be presented that identify the important phenomena and the limits that each process may impose on overall Return Flow Cascade operation. Modeling results are then used to estimate limits and performance for the experimental conditions, where possible. Prediction of Return Flow Cascade limits and performance for engine operation are presented in Chapter 5.

4.2 Time Scales

A comparison of the time scales associated with the two-phase and transport processes in the Return Flow Cascade cooling system can be used to determine what processes are significant in transient cascade operation.

The time scale for evaporation becomes important when a large portion of the liquid in the system has formed a pool at the tip of the blade. This could occur in blades that are oriented in the tip-down position after the engine winds down. In order for liquid to return to the shelves, the tip pool needs to evaporate, the vapor must flow to the condenser, and the liquid must return to the shelves. The time scale for evaporation of all the liquid in the system is dependent on the heat to the system, Q, the total mass of liquid in the system, m_{liq}, and the heat of vaporization of the liquid and is given by

$$t_{evap} = \frac{m_{liq} h_{fg}}{Q}. \tag{4.1}$$

Two other important time scales are associated with vapor flow from the blade to the condenser, and liquid flow from the condenser to the shelves. These is important in understanding how the system responds to sudden changes in heat flux to the blade. The time scale for vapor flow from the blade to the condenser is

$$t_{vap} = \frac{\rho_v A_{bcp} L_{span}}{\dot{m}}. \tag{4.2}$$

where L_{span} is the length of the blade from hub to tip, A_{bcp} is the cross sectional area of the blade center port, and $\dot{m}$ is the mass flow rate of vapor. The time scale for liquid return flow from the condenser to the blade shelves is

$$t_{liq} = \frac{L_{cond}}{u_{liq}} \tag{4.3}$$

where L_{cond} is the length of the condenser, and u_{liq} is the velocity of the liquid film. The time scale associated with conduction in the blade is

$$t_{conduction} = L^2 \frac{\rho c}{k} \tag{4.4}$$

where ρ, c, and k are the density, specific heat and thermal conductivity, respectively, of the blade material. L is the characteristic dimension for conduction. The conduction time scale is calculated for two characteristic dimensions, the blade skin thickness, and the span of the blade. The time scales for both rig and engine operation are shown in the Table 4-1.

Table 4-1 Time Scales for Two Phase and Flow Processes

Time Scale	Rig Conditions	Engine Conditions
Evaporation, t_{evap}	10 s	1 s
Vapor flow, t_{vap}	10^{-3} s	10^{-4} s
Liquid flow, t_{liq}	10^{-2} s	10^{-3} s
Conduction, $t_{conduction}$ (Blade Skin)	10^{-1} s	10^{-1} s
Conduction, $t_{conduction}$ (Blade Span)	10^{2} s	10^{2} s

The time scales for vapor and liquid flow are on the order of a hundredth or a thousandth of a second, indicating that the system response to transients is essentially instantaneous. Also, since the vapor and liquid flow time scales are so small compared to the time it takes for a complete

scan of the blade surface temperature (about 1 minute), transient effects were not captured in the scans.

4.3 Pool Boiling

Determining the mechanism by which evaporation occurs in the shelves is achieved by modeling the process as pool boiling, in which liquid on a heated surface can boil if the temperature of the surface is higher than the saturation temperature of the liquid. In this case, the shelf structure is the heated surface and the liquid potassium that fills each shelf forms the pool.

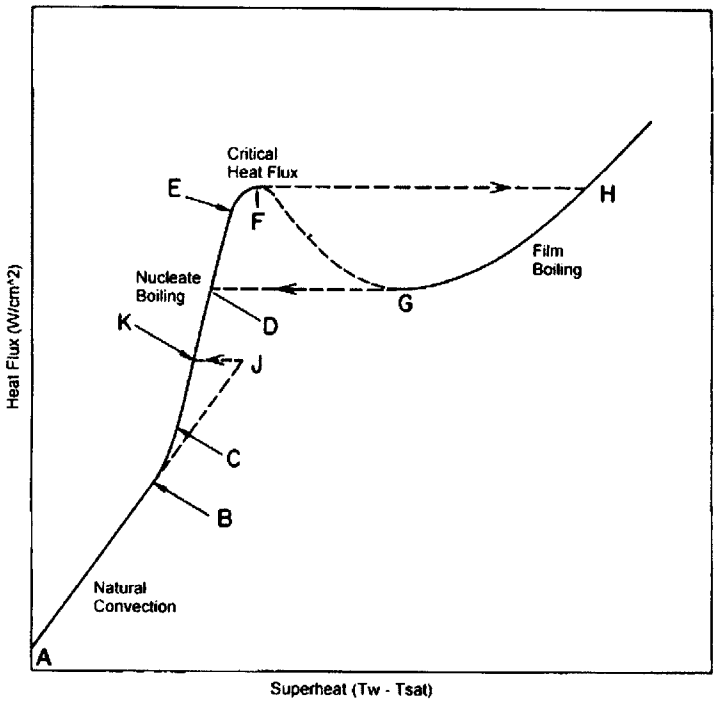

Figure 4-1 Boiling Curve [21]

The regimes of pool boiling are shown in Figure 4-1. Natural convection is represented in Figure 4-1 as the linear curve AJ. Transition to nucleate boiling can occur as early as point B and the nucleate boiling regime continues to point F, which represents the critical heat flux. If the heat flux is increased above this point, the boiling will shift to film boiling (point H) with a consequent large increase in surface temperature. If the heat flux is then reduced, film boiling continues down curve HG and at point G there is a shift back to nucleate boiling at point D. The most stable, optimal boiling heat transfer is within the natural convection or nucleate boiling

regimes, along curve AE. Prediction of the critical heat flux is necessary to ensure operation in this region. A review of conduction and natural convection in the liquid pool will be presented first.

4.3.1 Conduction and Free Convection in Liquid Pool

Before transition to natural convection or nucleate boiling in the pool, the heating of the liquid in the shelves will occur by conduction only. A simplified model of the shelf is used for the conduction analysis, shown in Figure 4-2.

The liquid is trapped in the pool by the rotational acceleration, g, which acts in the radially outward direction due to the centrifugal force of the rotating turbine blade. The radius is measured from the axis of the rotating arm, and is given as r_1 and r_2 at the free surface and shelf surface of the pool, respectively.

Assuming a wall temperature of T_w and heating from the top surface only, the temperature profile in the liquid pool can be found from a one-dimensional, steady state conduction analysis. The temperature distribution of the liquid pool as a function of radius is

$$T(r) = T_w - \frac{q_{shelf}}{k_l}(r_2 - r) \tag{4.5}$$

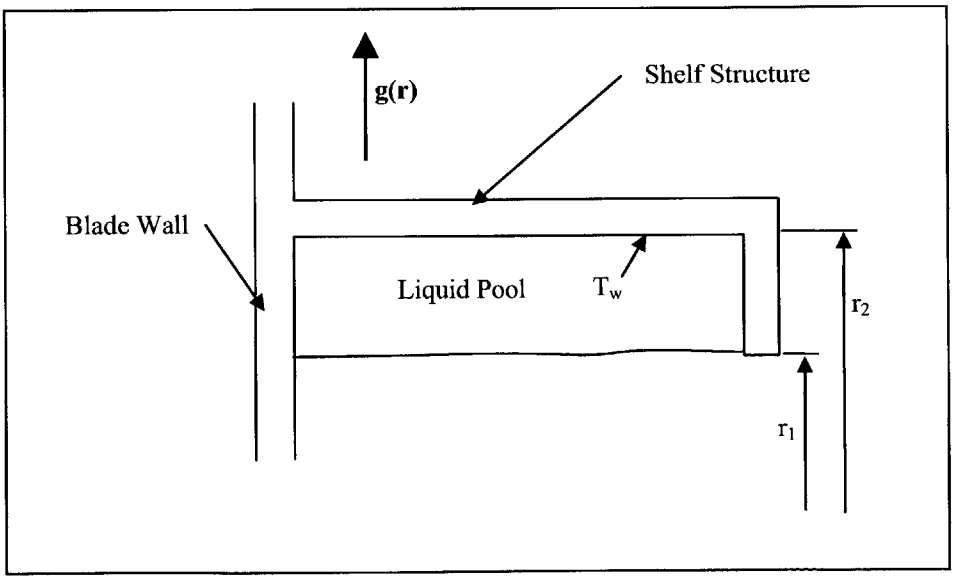

Figure 4-2 Simplified Model of Liquid Pool in Shelf

where q_{shelf} is the heat transfer to one shelf and is defined as $q_{shelf} = q_{total}/N_{shelf}$ where N_{shelf} is the number of shelves in the blade. The assumption here is that the heat flux is uniform over the surface of the blade and each shelf must dissipate the same level of heat. The thermal conductivity of the liquid coolant is k_l. For conduction heating only and typical rig operation conditions, the temperature change from the shelf surface to the free surface is less than 1 K. Evaporation could occur from the surface of the pool if the temperature there were higher than the saturation temperature corresponding to the pressure at the surface of the pool. For the experimental testing, the pressure increase from the free surface of the pool to the shelf surface is approximately 1.5 kPa (0.22 psi).

The point of transition to natural convection is difficult to predict for complex geometries such as the shelf structure in the blade. Also, empirical relations for simple geometries often do not extend to the range of rotational accelerations seen in the rotating rig or in gas turbines. The general effect is that a higher pressure differential in the liquid pool results in more convective flow and enhances natural convection heat transfer. However once the transition has occurred, it can be determined whether free convection or forced convection is the dominant process. This is important for understanding whether the transition to nucleate boiling will occur in a stable manner or not. The conduction analysis was done assuming a stagnant pool of coolant, but in actuality there is some transverse coolant flow along a given shelf to deliver coolant to all portions of the blade including the leading edge and trailing edge. A measure of the relative importance of natural and forced convection is the dimensionless group Gr_L / Re_L^2 which represents the ratio of the buoyancy force to the inertial force and is given by:

$$\frac{Gr_L}{Re_L^2} = \frac{g\beta\Delta T\rho_l^2 A_{pool}^2 L}{\dot{m}_{shelf}} \tag{4.6}$$

where $\dot{m}_{shelf}$ is the mass flow of liquid transversely in the shelf, A_{pool} is the cross-sectional area of the liquid pool in the shelf, and L is the distance along a given shelf where transverse flow could occur. For the testing conditions the ratio $Gr_L / Re_L^2 \gg 1$ which indicates that free convection is dominant and forced convection effects can be neglected. This is important in understanding how the transition to nucleate boiling will occur in the blade model.

4.3.2 Transition to Nucleate Boiling

For most normal liquids, the transition to nucleate boiling occurs when vapor bubbles are generated at nucleation sites on the heater surface. In the case of liquid metals, whose wetting properties are superior to those of other liquids like water, the transition to nucleate boiling can occur later and at higher wall superheats. The transition may be sudden, resulting in generation of vapor at the heating surface which causes liquid to be temporarily ejected from the pool. [26] This is shown in Figure 4-1 as the transition from the natural convection line to the nucleate boiling curve along line JK, If this occurs in the blade model the baffle will keep the liquid in the shelves. The superheat ($T_w - T_{sat}$) at which transition occurs is difficult to predict because it is dependent on many parameters. Many experimental studies have been done with varying results. Superheats as high as 278 K (500 °F) have been measured for potassium before an unstable transition from free convection to nucleate boiling. [27] Forced convection wall superheats are typically lower than natural convection superheats. The fact that free convection is the dominant effect in the shelves before transition to nucleate boiling could result in higher superheats.

The parameters that are important for the onset of nucleate boiling in cascade operation are the pressure at the heating surface, the concentration and types of inert gases that may be present, the roughness of the shelf surface, the pressure-temperature history, and the method with which power is applied to the blade. The effect of pressure for pool boiling of liquid metals has been well documented. As the pressure increases, the superheat at transition to nucleate boiling decreases. An approximate value of the superheat was estimated by Dwyer [26] by starting with the Laplace bubble equilibrium equation, which describes a spherical bubble of vapor under thermodynamic and mechanical equilibrium.

$$P_v - P_L = \frac{2\gamma}{r} - P_G \tag{4.7}$$

P_G is the partial pressure of the inert gas in the bubble initiation cavity. The equation can also be written as

$$P_v - P_L = \frac{2\gamma}{r}(1-\xi) \tag{4.8}$$

where $\xi = rP_G/2\gamma$, a dimensionless parameter that varies from 0 to 1 and is a measure of the inert gas content of the bubble. The Clausius-Clapeyron equation can be written as follows.

$$\frac{dP}{P} = \frac{h_{fg}}{R}\frac{dT}{T^2} \tag{4.9}$$

Integrating, and combining with Equation (4.8) gives

$$T_L - T_{sat} = \frac{2RT^2\gamma}{\lambda r P}(1-\xi) \tag{4.10}$$

A representative liquid coolant pressure at the heater surface expected during blade model testing is 0.5 atm. This includes the additional effect of rotational acceleration which results in higher pressures in the liquid pool at the heater (or shelf) surface. The superheat for potassium, with no inert gas in the system ($\xi = 0$), a bubble radius of 5×10^{-5} inch, and a system temperature of 590 K (600 °F) is $T_L - T_{sat}$ = 104 K (187 °F). The lower the superheat, the more gradual the transition to nucleate boiling will be and the less likely the liquid coolant will be expelled from the pool during the transition. If the baffle was not present and the transition to nucleate boiling took place nearly simultaneously in all shelves, liquid could be expelled and would pool at the blade tip, depriving all the shelves of coolant and possibly causing blade burn-out.

4.3.3 Prediction of Critical Heat Flux

Predicting the critical heat flux (CHF) for both the experimental set-up and any future engine applications of the Return Flow Cascade is necessary to understand the heat flux limits of the system. Operation at higher heat fluxes than the CHF will result in transition to the film boiling regime at a much higher wall temperature.

The critical heat flux can be approximated using an empirical equation developed for a set of conditions that are similar to those encountered during the blade model testing. Two such correlations come from the work of Colver and Balzhiser and Subbotin et al as related in Dwyer [26]. A comparison of the experimental conditions from the published references and the conditions in the present testing are summarized in Table 4.2.

Table 4-2 Comparison of CHF Test Conditions for Previously Published Work with Potassium and Current Experimental Set-up

	Subbotin, et al	Colver and Balzhiser	Present Testing, MIT
Heater geometry	Horizontal disk, 1.5 in diameter	Horizontal cylinder, 0.38 in diameter, 1.25 in long	Horizontal cascade shelf, 0.05 in wide, 2.75 in long (along blade perimeter)
Pool geometry	8.0 in deep, right cylinder, 2.75 in diameter	4 – 6 in deep, right cylinder, 1.36 in diameter	0.02 in deep, 0.05 in wide, 2.75 in long (blade perimeter)
Heating Surface Material	Stainless Steel	Haynes-25 Alloy (Co 51%, Ni 10%, Cr 10%, W 15%)	Nichrome
Pressure above liquid, psia	0.17 - 25	0.23 - 22	0.4 – 8.5
Pressure at heater surface, psia	0.36 – 25.2	0.33 – 22.14	0.46 – 8.81
Acceleration of Gravity (m/s^2)	9.8	9.8	494 – 4444

The empirical equations for the CHF data are, for Colver and Balzhiser,

$$q_{cr} = 4\times10^5 p_L^{0.17} \tag{4.11}$$

and for Subbotin, et al,

$$q_{cr} = 3.7\times10^5 p_L^{0.2} \tag{4.12}$$

where p_L is in psia, and the critical heat flux q_{cr} is in Btu/(hr ft^2). These two empirical equations depend only on the pressure at the boiling surface, p_L.

There are two major differences between the conditions used to develop the above empirical equations and the actual MIT test conditions. The first is the difference in heater and pool geometry. Above a certain minimum representative heater length, the CHF is independent

of the geometry. This length can be defined in terms of a dimensionless heater length, L/λ_d where λ_d is the Taylor instability wavelength, which represents the distance that separates columns of rising bubbles on the heater surface. The Taylor instability wavelength is defined as

$$\lambda_d = 2\pi\left[\frac{3\gamma}{g(\rho_l - \rho_v)}\right]^{1/2}. \tag{4.13}$$

Lienhard and Dhir [28] found for ordinary liquids (not liquid metals) that for values of this ratio less than 3, the CHF could not be considered to be independent of the geometry of the heater and instead depends on the number of vapor jets supported by the heater surface. Fewer vapor jets mean a lower CHF, which could curtail the stable operating range for nucleate boiling. For the MIT testing conditions, L/λ_d ranges from 0.09 – 0.29. For this value of L/λ_d the empirical equations above would not hold for ordinary liquids. However, for liquid metals, the CHF is made up of contributions from both the vapor transport process as well as what is known as conductive-convective heating. These contributions are of the same magnitude, and conductive-convective heating is much less dependent on heater geometry than the vapor transport effect. The CHF given by Equations (4.11) and (4.12) could be used to provide a conservative estimate, even for the much smaller heating surface.

The second difference between the empirical equation conditions and the MIT test conditions is the large difference in the acceleration of gravity. The tests of Subbotin et al and Colver and Balzhiser were conducted at 1 G. Theoretical analysis has shown that the acceleration of gravity has the same effect on both the vapor transport and conduction-convection contributions to the CHF. As acceleration of gravity increases, the CHF also increases. Therefore, use of these equations can be justified since they will under predict the CHF for the MIT testing conditions. It is certainly desirable to have a more accurate prediction, but the CHF results from these empirical equations will provide a conservative approximation.

There are several generalized empirical equations for CHF in the literature that are compiled from a range of data sets for several different liquid metals. Kirillov [26] developed an equation based only on the liquid thermal conductivity and the pressure at the heater surface, based on experimental data for sodium, potassium and cesium, all at an acceleration of gravity of 1 G.

$$q_{cr} = 3.12\times10^{5} k_L^{0.6} \left(\frac{p_L}{p_{cr}}\right)^{1/6} \tag{4.14}$$

where k_L is in units of Btu/(hr ft °F) and q_{cr} is in units of Btu/(hr ft^2). Subbotin et al [26] developed an empirical equation based on experimental CHF data for sodium, potassium, rubidium and cesium for both horizontal flat disk heaters as well as horizontal cylindrical heaters.

$$q_{cr} = 0.14 h_g \rho_v \left[1+\frac{45}{P_{cr}}\left(\frac{P_{cr}}{P_L}\right)^{0.4}\right]\left[\frac{g\gamma(\rho_l-\rho_v)}{\rho_v^2}\right]^{1/4} \tag{4.15}$$

Subbotin's correlation does include a dependence on the acceleration of gravity, although the range of G's that the equation is valid for is not given. The literature is sparse in empirical measurements of CHF at high rotational accelerations.

A comparison of the two empirical equations, each based on one set of CHF data, and the two generalized empirical equations is shown in Figure 4-3. The system temperature shown on the x-axis sets the pressure at the free surface of the liquid pool. The pressure in Equations (4.11) and (4.12) is the pressure at the heating surface and is a function of the pressure at the free surface and the depth of the pool.

For an acceleration of gravity of 1 G, Kirillov's equation gives the most conservative estimate of CHF. Subbotin's generalized correlation, Equation (4.15), is proportional to $g^{1/4}$. For the MIT testing conditions (up to 400 G's), the predicted CHF would be 4.5 times higher than that predicted at 1 G. For a typical gas turbine level of rotational acceleration, Subbotin's correlation would predict a CHF more than 8 times higher than that at 1 G. For the purposes of this investigation, and until more empirical CHF data is available at higher gravity levels, Kirillov's generalized empirical equation will be used as a conservative estimate of the CHF. Therefore the heat flux limit is given by Equation (4.14) and is shown in Figure 4-3 as the Kirillov (Generalized) curve. The heat flux limit given by Kirillov's generalized correlation is higher than both the heat flux achievable in the MIT experimental apparatus and the heat flux expected in a modern gas turbine engine and therefore should not be a limiting factor in cascade performance.

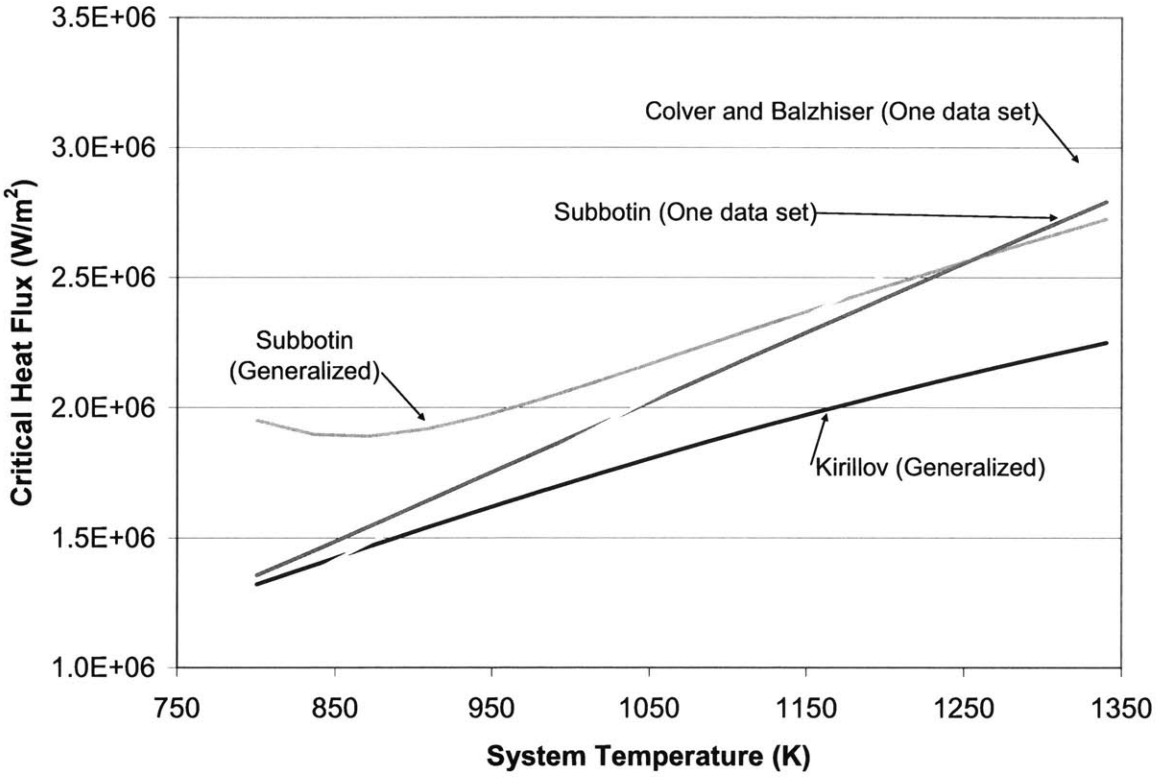

Figure 4-3 Comparison of Empirical Correlations for CHF of Potassium, g = 9.8 m/s^2

4.3.4 Boiling Regime for Engine Operation

The high rotational acceleration levels in a gas turbine engine will maintain the liquid pool in the natural convection regime by enforcing a large pressure gradient but small temperature gradient through the pool. A typical value of the temperature at which the vapor evaporates from the pool for an engine is 1000 K. The corresponding vapor pressure at the pool surface is then 75 kPa. Taking into account an acceleration of gravity of 50,000G and a pool depth of 0.5 mm, the pressure at the shelf wall is 240 kPa. The temperature at the shelf wall can be estimated using the conduction analysis given in Section 4.3.1 and is found to be 1024 K. This estimate is high because natural convection currents in the pool will enhance mixing and reduce the temperature gradient through the pool. The boiling point of potassium at the shelf wall pressure of 240 kPa is 1127 K, which is much higher than the temperature of the liquid at any

location in the pool. For this reason, evaporation will occur only at or near the surface of the pool and the liquid pool will be maintained in the natural convection regime.

4.4 Vapor Flow

Vapor evaporating from the liquid pools in the shelves flows through vapor ports in the baffle and into the center blade port. The vapor flows radially inward motivated by the pressure gradient between the blade and the cooler condenser. The baffle which delineates the perimeter of the center blade port extends into the condenser approximately 0.66 inch below the hub of the blade. This portion of the vapor flow area is referred to as the condenser inlet section. The vapor flows into the condenser and is condensed on the condenser walls. There is a possibility that the flow will become choked at some point in the blade center port or the condenser inlet section. If this occurs, the mass flow of vapor to the condenser will have reached a maximum for a particular blade temperature and port area. If the heat flux to the blade is increased while the flow is choked the blade center port area will not be able to pass additional mass flow at that temperature, and the temperature of the blade wall will increase as a result. The choked condition uncouples the condenser operation from the evaporation rate in the blade. With unchoked flow an increase in condenser cooling will result in a lower blade surface temperature. If the flow to the condenser is choked, any increase in condenser cooling will not affect the temperature of the blade. Optimum performance of the return flow cascade will occur when the vapor flow is unchoked. A major objective of the vapor flow modeling is to determine the choking limit as a function of system temperature, heat flux to the blade, and rotational acceleration rate.

4.4.1 Vapor Choking in Blade

The vapor contribution from each shelf flows into the center blade port. The vapor flow can be modeled as a flow with mass addition in a constant area duct. The objective of this analysis is to determine the radial velocity distribution, the radial pressure distribution, and the choking limit in the blade center port. The geometry for this analysis is shown in Figure 4-4.

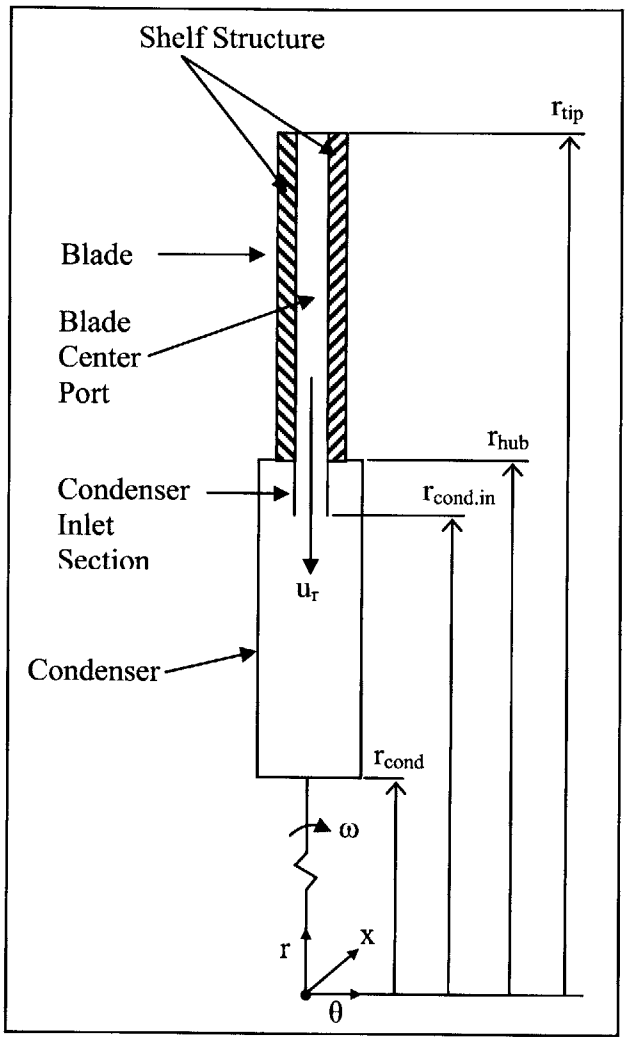

Figure 4-4 Diagram of Blade and Condenser for Vapor Flow Analysis

Euler's equation for inviscid flow in the r-direction can be written as:

$$\rho_v\left(\frac{\partial u_r}{\partial t}+u_r\frac{\partial u_r}{\partial r}+\frac{u_r}{r}\frac{\partial u_r}{\partial \theta}-\frac{u_\theta^2}{r}+u_x\frac{\partial u_r}{\partial x}\right)=-\frac{\partial p}{\partial r}+\rho_v g_r z \qquad (4.16)$$

Several assumptions are used to simplify the analysis. The flow is steady and there is no flow in the x- or θ-direction. The radial component of the vapor flow contributions from the shelves is neglected. The acceleration of earth's gravity is much less than the rotational acceleration and is therefore neglected. Reducing Equation (4.16) using the preceding assumptions, and also rewriting the centrifugal acceleration term in terms of the rotational acceleration of gravity, g, we find the following result:

$$\rho u_r \frac{\partial u_r}{\partial r} - \rho g = -\frac{\partial p}{\partial r} \tag{4.17}$$

The potassium vapor state can be modeled as an ideal gas since the state is well away from the critical point.

$$\rho = \frac{p}{RT} \tag{4.18}$$

The mass flow in the center blade port as a function of radius, r, is

$$\dot{m}(r) = (r_{tip} - r)\frac{d\dot{m}}{dr} \tag{4.19}$$

where

$$\frac{d\dot{m}}{dr} = \frac{\dot{q}A_s}{h_{fg}} \frac{1}{(r_{tip} - r_{hub})}. \tag{4.20}$$

Equation (4.20) includes the assumption that the heat flux is constant over the entire area of the blade and that each shelf produces an equal amount of vapor. This assumption is valid for the experimental apparatus. The mass flow as a function of radius can also be denoted

$$\dot{m}(r) = \rho u_r A_p = \frac{p u_r A_p}{RT} \tag{4.21}$$

Combining Equations (4.19) and(4.21), and solving for u_r, the velocity distribution in the blade center port is then

$$u_r = \frac{1}{\rho A_p}(r_{tip} - r)\frac{d\dot{m}}{dr}. \tag{4.22}$$

Equation (4.22) is differentiated:

$$\begin{aligned} \frac{du_r}{dr} &= \frac{d}{dr}\left[\frac{1}{\rho_v A_p}(r_{tip} - r)\frac{d\dot{m}}{dr}\right] \\ \frac{du_r}{dr} &= \frac{R(r_{tip} - r)}{A_p p^2}\left(p\frac{dT}{dr} - T\frac{dp}{dr}\right)\frac{d\dot{m}}{dr} - \frac{1}{A_p \rho_v}\frac{d\dot{m}}{dr} \end{aligned} \tag{4.23}$$

and finally, substituted into Equation (4.16), which can be solved for dP/dr:

$$\frac{dp}{dr} = \left(\frac{(r_{tip} - r)}{A_p p}\frac{d\dot{m}}{dr}\right)^2 R\left(T\frac{dp}{dr} - p\frac{dT}{dr}\right) + \frac{RT(r_{tip} - r)}{pA_p^2}\left(\frac{d\dot{m}}{dr}\right) + \frac{p}{RT}g \tag{4.24}$$

To find the pressure distribution in the blade port, a simplifying assumption is made that $\frac{dT}{dr} << \frac{dp}{dr}$. The ideal operating mode of the Return Flow Cascade is to maintain a nearly constant blade surface temperature. This can be carried forward to assume that the vapor contribution at each shelf is at the same temperature as the vapor already flowing through the blade center port, resulting in a constant system temperature throughout the blade and transition section. Solving for $\frac{dp}{dr}$ yields Equation (4.25):

$$\frac{dp}{dr} = \frac{\frac{RT(r_{tip} - r)}{pA_p^2}\left(\frac{d\dot{m}}{dr}\right)^2 + \frac{p}{RT}g}{1 - RT\left(\frac{(r_{tip} - r)}{pA_p}\frac{d\dot{m}}{dr}\right)^2} \tag{4.25}$$

The temperature that appears in Equation (4.25) represents a constant system temperature. Choked flow occurs at the point at which $dP \geq 0$ (or when $dp/dr \leq 0$ since $dr < 0$ as the analysis is done from tip to hub). The system temperature and heat flux (which affects the magnitude of $d\dot{m}/dr$) where $dp/dr = 0$ represent the choking limits on the Return Flow Cascade.

The first term in the numerator of Equation (4.25) represents the contribution of the momentum in the r-direction due to the mass addition. The second term in the numerator is the contribution of the force due to rotational acceleration. Both of these terms are always positive. The second term in the denominator is a dimensionless parameter which is the radial Mach number squared. The choking criterion for the blade can be written as

$$RT\left(\frac{(r_{tip} - r)}{pA_p}\frac{d\dot{m}}{dr}\right)^2 \geq 1 \tag{4.26}$$

or

$$M_r^2 \geq 1 \tag{4.27}$$

for choking to occur. The vapor pressure p is roughly proportional to T^2. Therefore the left hand side of Equation (4.26) is proportional to $1/T^3$. As temperature increases, vapor pressure in the blade increases, and the Mach number decreases. To determine whether the flow will choke for

a given set of operating conditions (heat flux to the blade, blade system temperature, and rotational acceleration) Equation (4.25) must be solved along the span of the blade. Because Equation (4.25) is not valid once the flow has choked, it must be solved in a step-wise fashion until the choking criterion is true.

A similar analysis can be done for the condenser inlet section, which is modeled as flow in a constant area duct. The major difference between this model and the previous one is that the mass flow through the condenser inlet section is constant. Starting with the reduced Euler equation, Equation (4.17), and Equations (4.18), and (4.21), the pressure gradient for the condenser inlet section is

$$\frac{dP}{dr} = \frac{\frac{P}{RT}g}{1-\left(\frac{\dot{m}}{PA_p}\right)^2 RT} \tag{4.28}$$

We can see that any pressure gradient in the condenser inlet section is due only to the effect of the centrifugal force on the vapor flow. The choking criterion in the condenser inlet section is

$$\left(\frac{\dot{m}}{PA_p}\right)^2 RT \leq 1 \tag{4.29}$$

Equation (4.28) must also be solved in a step-wise fashion. A Matlab code was written to solve for the pressure gradients in both the blade and the condenser inlet section. The code listing is located in Appendix D. The algorithm iteratively solves Equations (4.25) in the blade port and (4.28) in the transition section to determine if, for a given heat flux, system temperature, and rotational acceleration, the flow will choke. Once the choking conditions are known, the pressure gradient for a range of non-choking conditions can be calculated and the effects of the various operating parameters determined.

4.4.1.1 Comparison to Test Data

The minimum temperature required for non-choking vapor flow in the blade port is shown in Figure 4-5 at a rotational acceleration of 453G which corresponds to 15 RPS, the speed where most of the experiments were performed. The solid line shown on the plot is the

minimum system temperature required for non-choking flow as a function of power to the blade and is based on the preceding analysis.

Cascade initiation for Runs 10, 11, 13 and 19 occurred while the power was held constant and at a constant speed of 15 RPS. For other runs initiation occurred immediately after an increase in rotational speed from 10 to 15 RPS, indicating that a rotational speed limit was preventing cascade operation at the lower speeds. In either case, the cascade will not initiate until the minimum blade temperature at which vapor choking no longer restricts the mass flow to the condenser is reached, as shown in Figure 4-5. For runs where the cascade began operating immediately after an increase in speed it is likely that the minimum temperature for non-choking vapor flow had already been surpassed. For Runs 10, 11, 13 and 19, it would have been the other way around; the rig was operating at a fast enough speed for cascade operation, but the minimum temperature had not yet been reached. The temperature of the blade and the condenser were the only parameters changing when cascade initiation occurred for these runs, which strengthens the argument that a minimum temperature had not been reached.

The modeling in the previous section is based on the assumption that the temperature throughout the blade center port is constant and is the temperature that controls the onset of vapor choking. In actuality, the temperature in the blade port is not necessarily constant from hub to tip, especially when the blade has a conduction profile (hot mid-span and cooler hub and tip). To determine the temperature in the blade or condenser that controls the onset of vapor choking (and therefore the onset of cascade operation), the tip temperature, hub temperature and condenser temperature were plotted just at the point of cascade initiation for all runs where there was no blade tilt (Runs 7 – 13 and 19) and is shown in Figure 4-5. The point of cascade initiation when the blade tilt was evident (Runs 14 – 18) is difficult to pinpoint because the two sides of the blade initiated at different times, sometime as much as 10 or 15 minutes apart. The hub and tip temperatures shown in the plot are averages taken from the temperature map of the blade surface and therefore do not account for the temperature drop that occurs through the blade skin or the shelf structure.

A conclusion can be drawn from Figure 4-5 that the tip temperature controls the onset of vapor choking. One factor that supports this conclusion is the fact that when cascade initiation does occur, the temperature of the hub drops significantly, but the tip temperature hardly changes

and in some cases increases by several degrees. If the hub temperature controlled vapor choking, then the hub temperature drop would put the cascade back into the choking regime, and the temperature scan data shows that once the cascade has initiated, it will continue to cool effectively at the same conditions. When the center blade port is choked, the blade and condenser are uncoupled and the condenser temperature would have no effect on blade temperature.

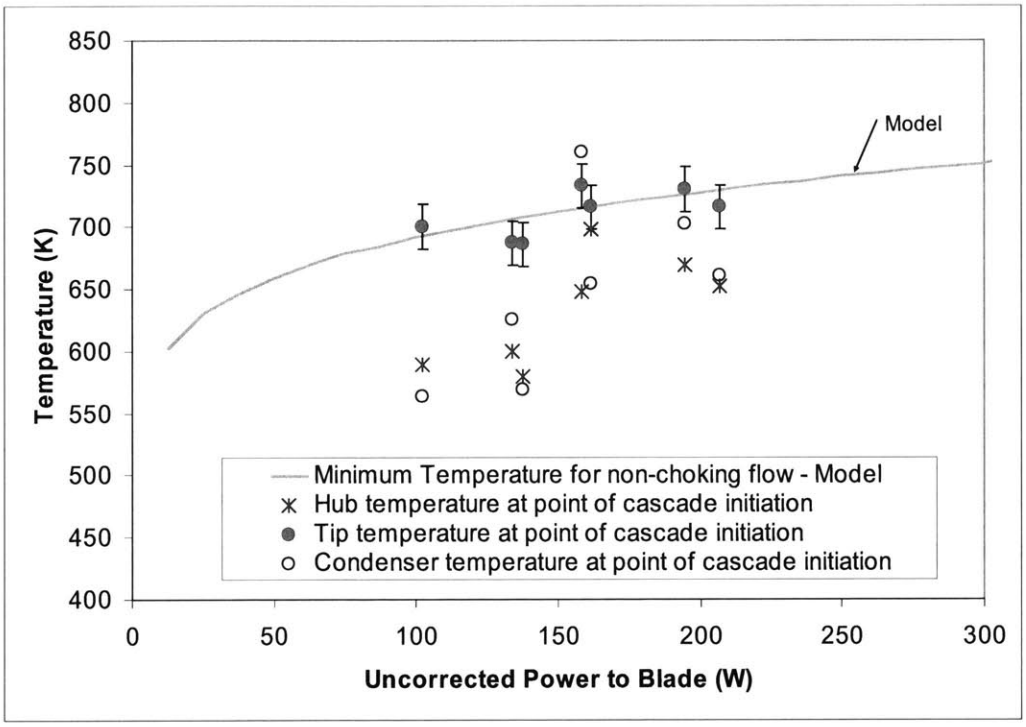

Figure 4-5 Comparison of Minimum Temperature for Unchoked Vapor Flow in Blade as Indicated by Cascade Initiation with Test Data at 453G (15 RPS)

Before cascade initiation occurs, the liquid is either trapped in the tip of the blade or inside the baffle at the entrance to the first shelf. Any evaporation that does occur will happen at the tip and the temperature of the vapor flowing down the blade center port will be set by the temperature of the tip pool. The modeling analysis assumes a constant temperature vapor flow from hub to tip and if the system behaves as described above, the temperature of the vapor flow will be nearly constant and will correspond to the tip temperature.

4.4.1.2 Pressure Gradient in Blade Port

The total pressure gradient through the blade port and transition section can be determined using the analysis outlined in Section 4.4.2. It is shown for a rotational acceleration of 453G (15 RPS) in Figure 4-6 as a function of system temperature. As the temperature increases, the total pressure drop through the blade and transition section decreases. The conditions shown on this figure represent the range of power levels in the experimental work. The analysis assumes a constant temperature through the blade port and condenser inlet. For conditions near the choking line, the pressure gradient determined from the model can be used to estimate the actual temperature difference between blade and condenser. This difference ranges from 5 – 15 K. As the temperature in the system increases, the pressure drop of the vapor through the blade and condenser decreases as shown in on the plot. At these conditions (well away from the choking line) the estimated temperature difference between blade and condenser is much smaller, on the order of 0.1 K. The average temperature difference measured during the experimental work when the cascade was operating is 50 ± 18 K. This temperature difference also includes the conduction through the blade skin, which ranges from 5 – 10 K for the heat fluxes achieved during the testing.

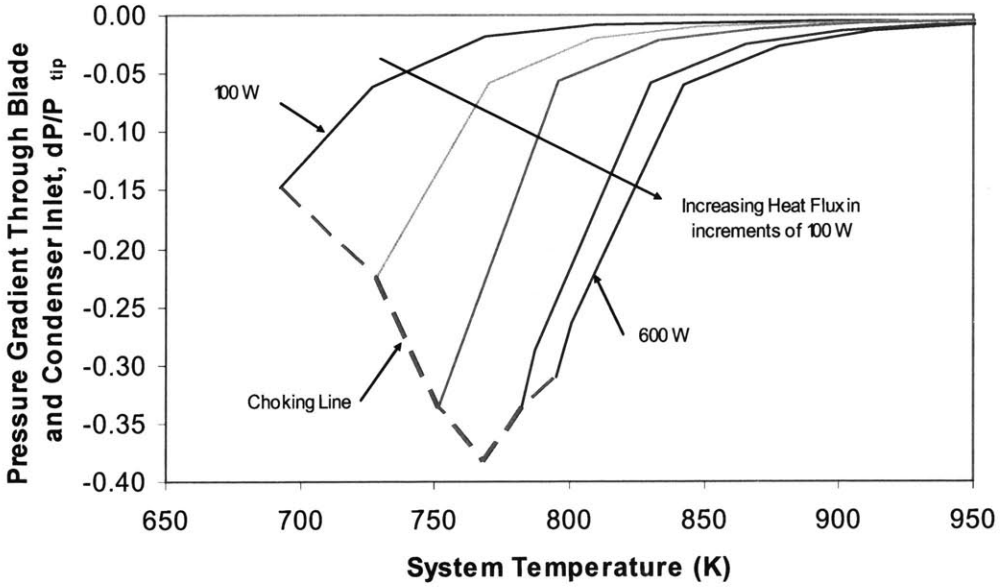

Figure 4-6 Pressure Gradient in Blade Port and Transition Section for Rotational Acceleration = 453G

4.5 Film Condensation

Vapor flow from the blade is liquefied on the condenser walls via either film condensation or dropwise condensation. Dropwise condensation can occur when the condensate does not wet the wall. Droplets of condensate will nucleate at small surface imperfections and grow in size until the rotational acceleration levels cause the droplets to flow radially outwards towards the blade. The heat transfer coefficients for dropwise condensation can be up to 30 times higher than for film condensation, although developing a non-wetting condenser surface can be difficult.

Film condensation will occur when the liquid wets the surface well. The droplets will tend to spread out, forming a thin liquid film that flows radially outward under the influence of the rotational acceleration. Laminar film condensation cane be analyzed using the classical Nusselt analysis. [29] The assumptions inherent in the Nusselt analysis for film condensation on a vertical wall are that the condensate forms a falling film under the influence of gravity, the flow is laminar and the liquid-vapor interface temperature is equal to the saturation temperature. For water, the film condensation flow is laminar for Re < 30. The film Reynolds number is defined as:

$$\mathrm{Re} = \frac{4\Gamma}{\mu_l} \tag{4.30}$$

where Γ is the mass flow rate per unit width of film and is given by

$$\Gamma = \frac{g\delta^3(\rho_l - \rho_v)}{3\nu_l} \tag{4.31}$$

For the rig conditions Re = 100 and for the engine conditions Re = 750 so the laminar analysis can not be used. At the higher Reynolds numbers the film could be wavy laminar or turbulent. The wave motion is complex and results from long-wavelength waves due to the rotational acceleration and shorter wavelength waves cause by surface tension. Empirical correlations for liquid metals at high levels of rotational acceleration is not available in the data. However, conservation estimates of the film thickness, film velocity, and temperature difference through the film can be made using the Nusselt analysis for the rig and engine conditions. The results are shown in Table 4-3.

Table 4-3 Comparison of Typical Film Condensation Parameters for Rig and Engine Conditions

	Rig Conditions (453G)	Engine Conditions (50,000G)
Film Thickness	9 μm	3 μm
Film Velocity	1 m/s	15 m/s
Temperature Difference through film	0.4 K	1.5 K

One possible limiting mechanism for film condensation is the vapor drag on the film. When the vapor flow is in the same direction as the acceleration of gravity, vapor drag can enhance the heat transfer. In the Return Flow Cascade, the vapor is flowing in the opposite direction of the acceleration and therefore may decrease the heat transfer effectiveness.

4.6 Liquid Flow

When the Return Flow Cascade is operating as designed, the liquid condensate flows up the condenser walls and fills the first shelf at the hub of the blade. The baffle prevents the liquid from spilling over the sides of the shelves and causes it to flow through the nine liquid overflow ports in each shelf. There is a maximum flow that can pass through a single overflow port which is dependent on the size of the port, the depth of the liquid pool in the shelf and the rotational acceleration of the system. In addition the flow may also be limited by surface tension effects. It should be noted that the liquid overflow ports in the experimental rig were inadvertently undersized. The overflow port size can be modified for future applications of the Return Flow Cascade.

4.6.1 Flow Limit Due to Surface Tension

A dimensionless parameter that characterizes the effect of surface tension on liquid flow is the Bond number,

$$Bo = \sqrt{\frac{\rho_l g D_h^2}{\gamma}}. \tag{4.32}$$

The Bond number is the ratio of the buoyancy force to the surface tension of the working fluid. If Bo < 1 then the flow will be surface tension limited.

If the assumption is made that there is poor wetting between the potassium and the nichrome walls of the liquid flow ports, then setting Bo = 1 and solving for g will give an estimate of the rotational acceleration needed to force the liquid through the port. A better method that takes into account the pool depth which causes the pressure head is to use a force balance between the surface tension force at the perimeter of the port and the pressure force from the liquid pool. The surface tension force at the entrance to the overflow port is

$$F_{ST} = \pi D_h \gamma \tag{4.33}$$

where D_h is the hydraulic diameter of the port, and γ is the surface tension. The pressure force due to the force from the liquid in the pool is

$$F_p = \rho g h A_{port} \tag{4.34}$$

where h is the depth of the pool. Combining Equations (4.33) and (4.34) and solving for g gives the minimum rotational acceleration needed to overcome the surface tension effects:

$$g \geq \frac{4\gamma}{\rho h D_h} \tag{4.35}$$

Since the surface tension and the density are both functions of temperature, a relationship between system temperature and rotational acceleration can be expressed, as shown in Figure 4-7 for a range of pool depths. The operating regime for the experimental work is shown on the plot. The operating regime for an engine is not shown because it is at much higher rotational acceleration levels (>50,000 G).

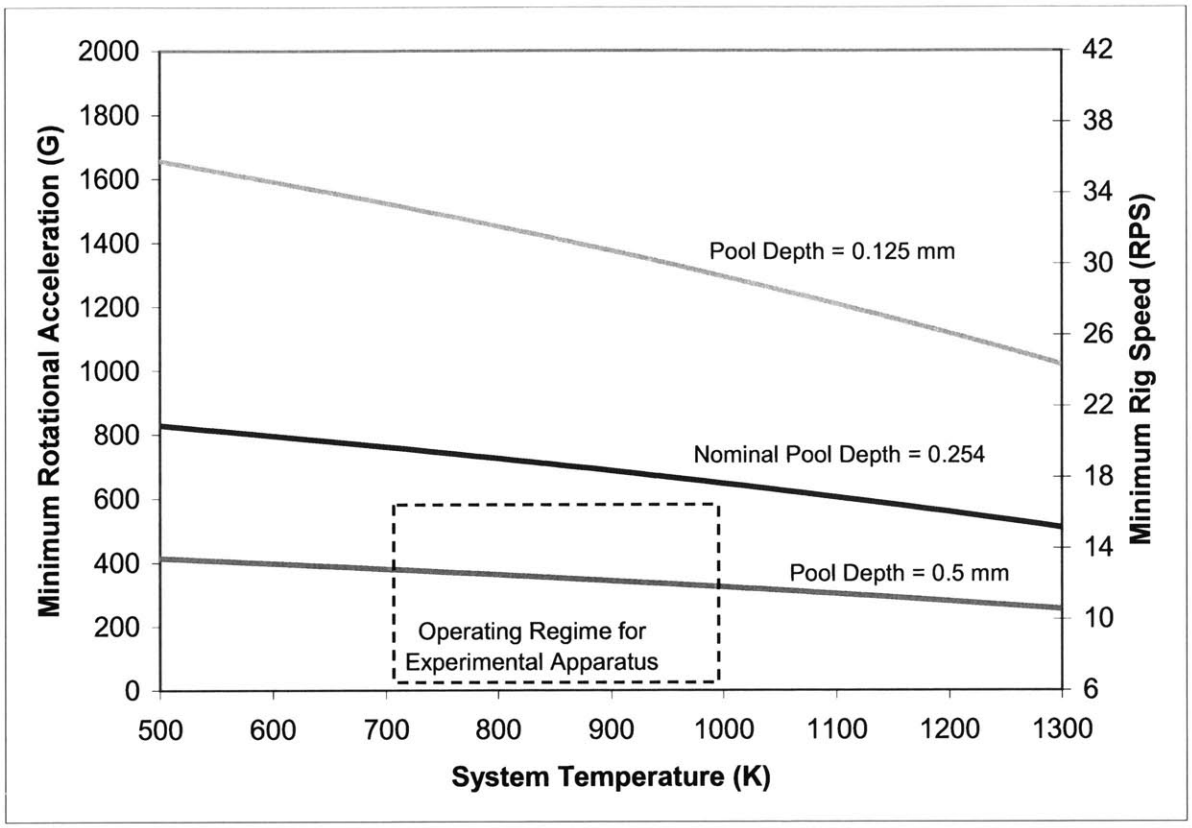

Figure 4-7 Minimum Rotational Acceleration Require to Overcome Surface Tension Limits in Liquid Overflow Port

At a pool depth of 0.254 mm the minimum rotational acceleration required for cascade operation is just outside the range of speeds tested in the experimental work (0 – 16.5 RPS). At the pool depth is increased, the minimum rotational acceleration falls within the range of rig speeds and specifically in the range where cascade operation initiations (11 – 15 RPS).

4.6.2 Fluid Flow Limit in Overflow Ports

There is a fluid flow limit on the amount of liquid mass flow that can pass through the overflow ports. The limit is dependent on the shelf geometry, the area and number of ports and the rotational acceleration. The maximum mass flow that can pass through the overflow ports is

$$\dot{m}_{ports} = \rho_l N_{ports} A_{port} \sqrt{2gh} \,. \tag{4.36}$$

The maximum mass flow that needs to pass through the nine ports in the first shelf is equal to the evaporation rate from the shelves:

$$\dot{m}_{evap} = \frac{qA_s}{h_{fg}} \tag{4.37}$$

where A_{blade} is the surface area of the blade. By setting Equations (4.36) and (4.37) equal and solving for g, a relationship can be found that gives the minimum rotational acceleration required for cascade operation.

$$g \geq \frac{1}{2h}\left(\frac{qA_s}{N\rho A_{port} h_{fg}}\right)^2 \tag{4.38}$$

For the average heat flux at cascade initiation (6 W/cm^2) the rotational acceleration limit is less than 4 RPS. This indicates that the this limit was not responsible for the fact that cascade operation did not occur below 11 RSP. It is much more likely, based on the results in the previous section, that surface tension limited the flow through the liquid overflow ports until speeds greater than 14 RPS were reached.

4.7 Blade Conduction Analysis

One method of determining whether the Return Flow Cascade is operating as designed during the experimental work is to make a prediction of the blade surface temperature without evaporative cooling for comparison. In the experimental apparatus, the blade is resistively heated. This can be modeled as internal heat generation in the blade skin. If the blade has a fixed temperature at the tip and the hub the resulting temperature profile would be parabolic with the maximum temperature at the span mid-point. In the rig, the current to the blade is delivered at the tip via copper bus bars. At the hub the majority of the current flows through a copper ground strap, rather than the stainless steel condenser structure connected to the blade. The conduction out of the tip and the hub of the blade affect the blade temperature profile and can be modeled using a transient one dimensional conduction heat transfer model with internal heat generation. A schematic of the set-up is shown in Figure 4-8.

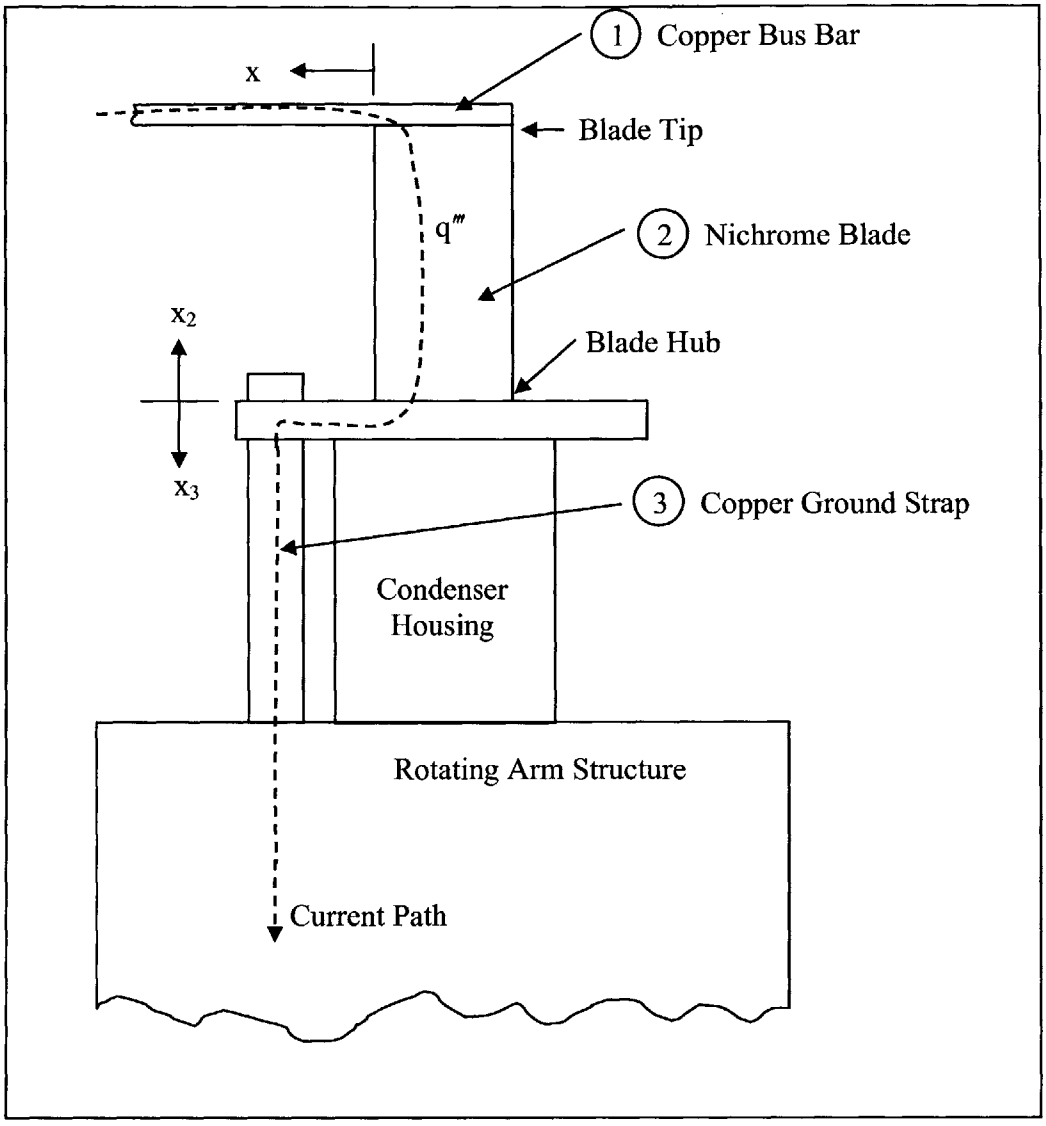

Figure 4-8 Schematic of Blade, Copper Bus Bar and Copper Ground Strap for Conduction Modeling Analysis

The current flows in through the copper bus bar, then through the blade from tip to hub and finally through the copper ground strap and into the rotating arm structure. The ground strap is dominant current path, carrying 97% of the current to the rotating arm when used. The blade assembly with the copper bus bar and ground strap is shown in Figure 3-6.

Designating the copper ground strap with the subscript 1, the blade with the subscript 2, and the copper bus bar with subscript 3, the energy balance for each component is as follows:

$$\frac{\partial T_1}{\partial t} - \alpha_1 \frac{\partial^2 T_1}{\partial x_1^2} = 0$$
$$\frac{\partial T_2}{\partial t} - \alpha_2 \frac{\partial^2 T_2}{\partial x_2^2} = \frac{q'''}{\rho_2 c_{p_2}} \tag{4.39}$$
$$\frac{\partial T_3}{\partial t} - \alpha_3 \frac{\partial^2 T_3}{\partial x_3^2} = 0$$

Equation (4.39) includes the assumption that there is heat generation only in the blade (1), but not in the copper bus bar (2) or ground strap (3).

The boundary conditions are

$$\begin{aligned} &x_1 = L_1, T_1 = T_\infty \\ &x_1 = 0, x_2 = L_2, T_1 = T_2 \\ &x_2 = 0, x_3 = 0, T_2 = T_3 \\ &x_3 = L_2, T_3 = T_\infty \end{aligned} \tag{4.40}$$

and the initial condition is

$$t = 0, T_1 = T_2 = T_3 = T_\infty \tag{4.41}$$

where L_1, L_2, and L_3 are the lengths of each number component in Figure 4-8 and T_∞ is the ambient temperature. The energy balance equations were solved numerically using finite difference forward time integration. Discretizing the derivatives in Equation (4.39), and solving for temperature at each time step gives

$$T_1^{i,n+1} = T_1^{i,n} + \Delta t \left[\alpha_1 \frac{T_1^{i-1,n} - 2T_1^{i,n} + T_1^{i+1,n}}{(\Delta x_1)^2} \right]$$
$$T_2^{i,n+1} = T_2^{i,n} + \Delta t \left[\alpha_2 \frac{T_2^{i-1,n} - 2T_2^{i,n} + T_2^{i+1,n}}{(\Delta x_2)^2} + \frac{q'''}{\rho_2 c_{p_2}} \right] \tag{4.42}$$
$$T_3^{i,n+1} = T_3^{i,n} + \Delta t \left[\alpha_3 \frac{T_3^{i-1,n} - 2T_3^{i,n} + T_3^{i+1,n}}{(\Delta x_3)^2} \right]$$

The temperature distribution was found using a Matlab code (located in Appendix D). The lengths of the copper ground strap and the copper bus bar were found by estimating the distance from the blade model where the temperature in the copper was equal to ambient

temperature. The model could then be run for a given corrected power for comparison to test data.

4.7.1 Conduction Profile Comparison with Test Data

The conduction profile from Run 7-32 was used for comparison. Scan 7-32 is shown in Figure 4-9. The mid-chord suction side temperature profile is compared to the model in Figure 4-10. The corrected power for Scan 7-32 is P_{corr} = 42.6 W. The model was run at 42.6 W and the result is shown for comparison on the plot. Because the temperature profile from Scan 7-32 levels off at the tip, the peak of the predicted curve is shifted slightly towards this tip. The leveling off at the tip is likely because of the formation of a tip pool which through natural convection or boiling is keeping the tip at a constant temperature. To adjust for this, the length of the blade was shortened slightly in the model and the model was run at many different corrected powers until the best match was found at a corrected power of 58 W. The discrepancy between the power used for the model match and the actual corrected power is likely due to an overestimation of the radiation losses. However, the major finding is that the profiles match well and indicate that little or no cascade cooling is occurring when the conduction profile is evident.

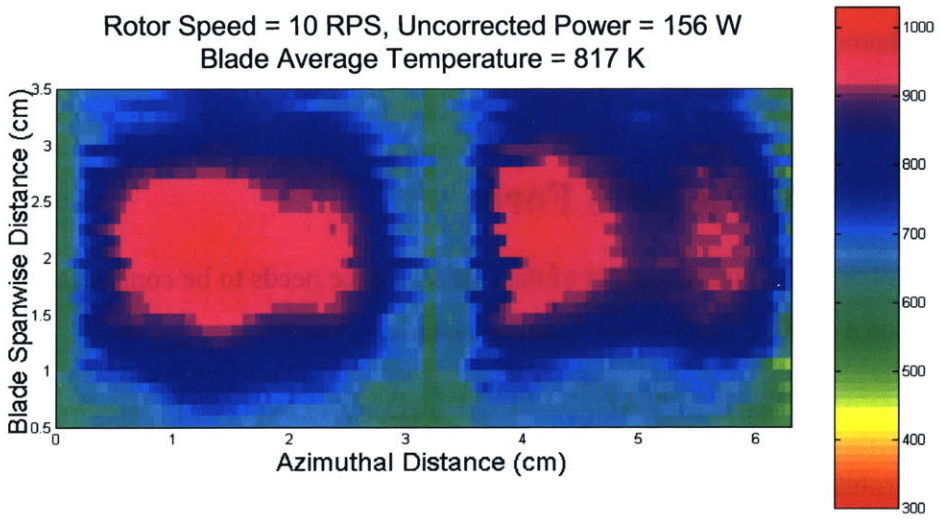

Figure 4-9 Blade Temperature Distribution (K), Corrected Power = 42.6 W (Run 7-32)

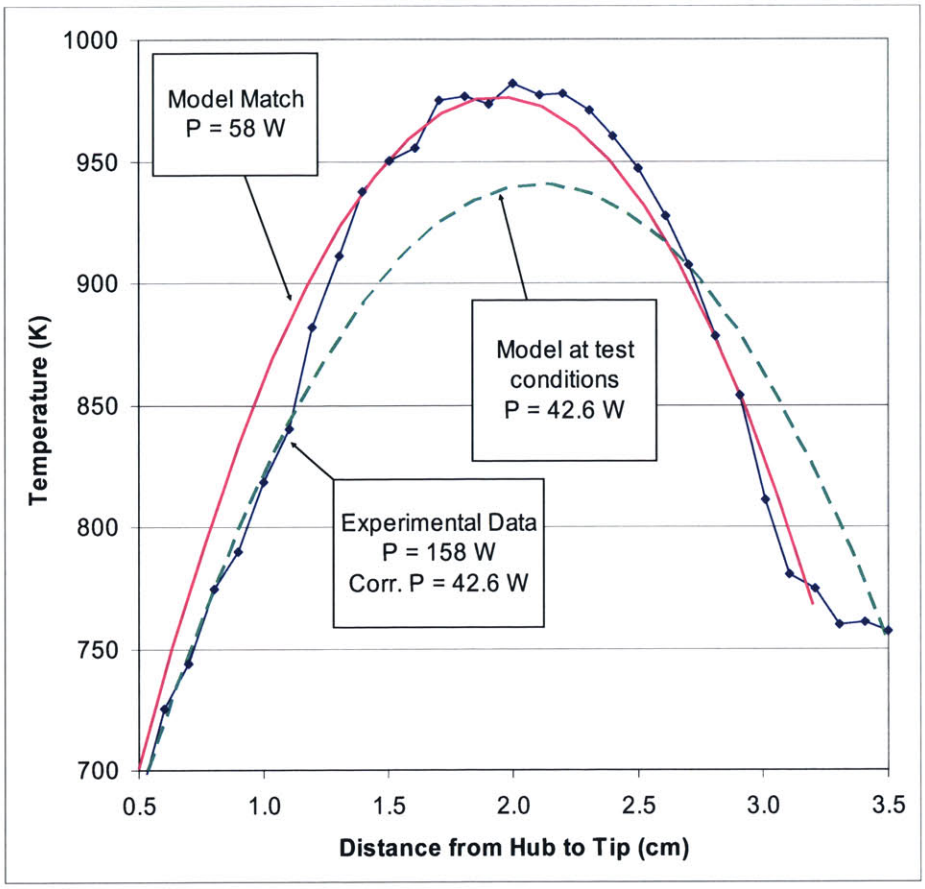

Figure 4-10 Mid-chord Suction Side Profile, Run 7-32 compared with Model Match

4.8 Effect of Coriolis Force

In a rotating system, the effect of the Coriolis force needs to be considered. The acceleration on a particle of fluid in a rotating system is

$$\vec{a} = \frac{d\vec{V}}{dt} + \frac{d^2\vec{r}}{dt^2} + \frac{d\vec{\Omega}}{dt} \times \vec{r} + 2\vec{\Omega} \times \vec{V} + \vec{\Omega} \times \left(\vec{\Omega} \times \vec{r}\right) \tag{4.43}$$

For a steady rotational speed and steady flow inside the blade, all terms on the right hand side in Equation (4.43) cancel out except for the last two, which represent the Coriolis acceleration and the centrifugal acceleration, respectively. A nondimensional parameter that describes the importance of the Coriolis effect is the Rossby number, defined as

$$\mathrm{Ro} = \frac{\mathrm{U}}{\mathrm{L}\Omega} \tag{4.44}$$

where U is a representative velocity of the fluid relative to the noninertial reference frame, L is the distance over which U varies appreciably, and Ω is the rotation rate. The Rossby number represents the ratio of inertial forces to Coriolis forces. If $\mathrm{Ro} \gg 1$, the Coriolis force is likely to have a very small effect on the flow pattern. If $\mathrm{Ro} \ll 1$, the Coriolis force is dominant. A plot of Rossby number for liquid and vapor flow in the blade for both rig and engine conditions is shown in Figure 4-11.

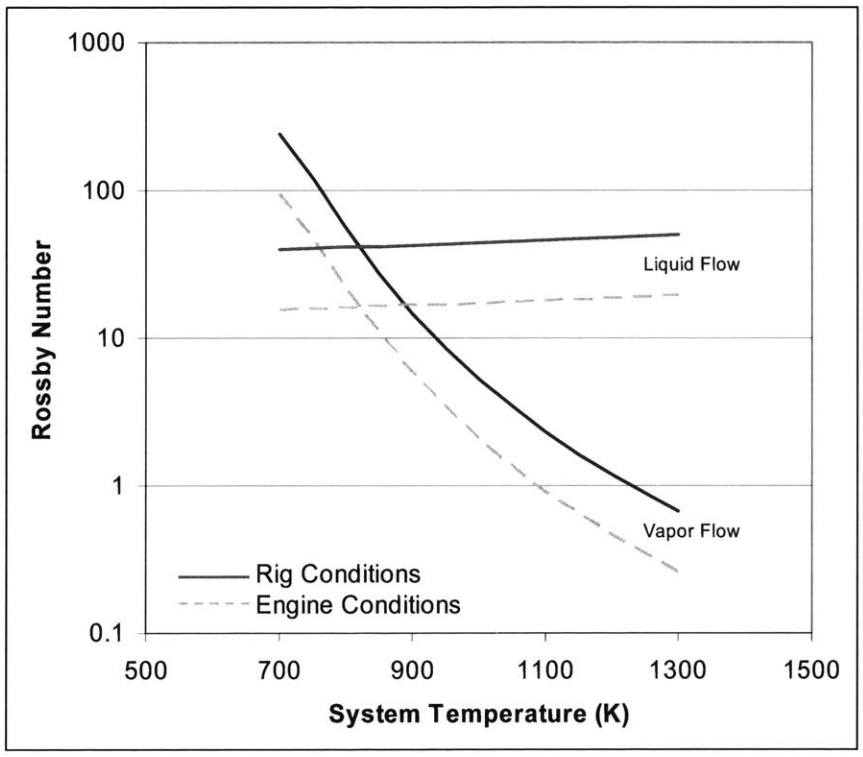

Figure 4-11 Effect of Coriolis Acceleration on Liquid and Vapor Flow in Blade for Rig and Engine Conditions

Figure 4-11 shows that the higher rotational acceleration levels found in engines result in a lower Rossby number and hence a larger effect from Coriolis forces. However, inertial forces are the dominant effect in liquid flow in the blade for both rig and engine operating conditions. The large drop in Rossby number as a function of system temperature for vapor flow is due to the fact that vapor density increases with temperature, which results in a lower vapor velocity in

the blade center port. The effect of the Coriolis force on the vapor flow is an additional force in the direction of the pressure side of the blade.

4.9 Modeling Conclusions

Several major conclusions were made as a result of the comparison of the experimental and modeling results. First, the Return Flow Cascade will operate in either the natural convection or nucleate boiling regimes. Second, the minimum speed limit on cascade operation is due to surface tension limited flow in the liquid overflow ports. Third, the tip temperature controls vapor choking. And finally, Coriolis effects are not significant in the rig operating regime.

Chapter 5 Engine Implementation

5.1 Extension of Modeling Results to Engine Conditions

A comparison of the evaporative cooling testing conditions and the conditions that the system would be exposed to in a modern gas turbine engine are shown in Table 5-1. The top rig rotational speed achieved during testing was 16.5 RPS which corresponds to a rotational acceleration of 567 G. Although this value is lower than the planned rotational acceleration levels, it is on the same order of magnitude. The cascade behavior that was observed is not expected to change significantly over that range (567 G to 1805 G). The fact that only low levels of power to the blade were achieved before the blade failed could affect the ability to extrapolate the cascade behavior in the rig to the cascade behavior in an engine. For this case, the modeling results will be used to bridge the gap and predict what the limits may be for engine operating conditions.

Table 5-1 Maximum Conditions Expected and Achieved During Testing

	Rotating Speed and Acceleration			Average Blade Heat Flux
	RPS	**Tip Speed (m/s)**	**G's**	
Rig (Planned)	30 RPS	98 m/s	1805 G	>100 W/cm^2
Rig (Actual)	16.5 RPS	54 m/s	567 G	24 W/cm^2
Engine	N/A	~ 400 m/s	~ 50,000 G	>100 W/cm^2

5.1.1 Pool Boiling

As a result of the higher rotational acceleration in an engine, the pressure difference through the liquid pool in the shelf is about 170 kPa (25 psi) compared to the pressure gradient for the rig conditions which was found to be 1.5 kPa (0.22 psi). The higher heat fluxes in an engine will cause a conduction temperature profile in the liquid pool with a temperature difference of up to 25 K, but the high rotational acceleration will enhance convection flow in the pool and a lower temperature difference would be expected. For engine conditions, then, the

expected boiling regime is the conduction or natural convection regimes. The pool temperature will never get high enough to allow for boiling anywhere other than near the surface of the pool.

The estimate of critical heat flux used for the rig conditions can also be used as a conservative estimate for the engine conditions. The results show that the estimated CHF is higher than the heat flux that turbines blades in current engines would be exposed to. The empirical boiling data in the literature indicates that as pressure at the heating surface increases, so does the CHF. It should be noted the empirical correlations used were not developed for liquid pools experiencing high levels of rotational acceleration. There may be other factors in determining the CHF which are unknown at this time, but the estimates made above provide a lower limit on the CHF for engine operation.

5.1.2 Vapor Choking

For the blade model tested in the experimental rig, it was found that the tip temperature controlled the point at which the vapor flow in the blade center port became unchoked. The formation of a tip pool could also occur in gas turbine engine operation and cascade operation will not begin until the tip temperature has reached the minimum required temperature. A comparison of the minimum required tip temperature for a gas turbine, with a rotational acceleration of 50,000G, and the rig, with a rotational acceleration of 453 G (or 15 RPS) is shown in Figure 5-1. There is a small change of about 10 K (18 °F) in the minimum temperature for unchoked flow as rotational acceleration is increased from 453G to 50,000G. Hence, the rotational acceleration is not a significant factor in determining the heat flux limit due to vapor choking. The modeling data presented in Figure 5-1 indicate that for a system temperature of 975 – 1025 °C (1300 – 1380 °F), the blade port area used in the blade model, and at the heat fluxes expected in modern gas turbine engines (>500,000 W/m^2), vapor choking in the blade port or transition section at steady state operation will not occur. In designing a new evaporatively cooled blade, the port area may be dependent on the shelf structure and the space availability in the blade.

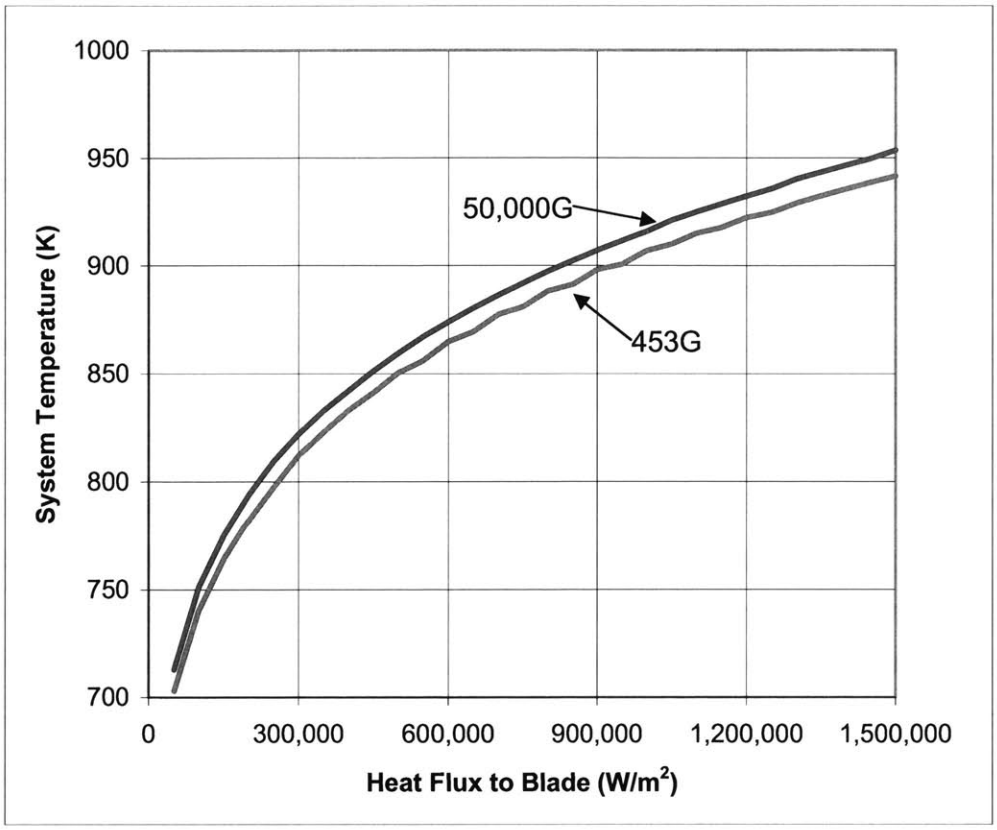

Figure 5-1 Minimum Blade Temperature for Non-Choked Vapor Flow in Blade Center Port

5.1.3 Film Condensation

A comparison of the film condensation parameters for rig and engine conditions was presented in Section 4.4, Table 4-2. The effect of vapor drag on the effectiveness of the heat transfer in the condenser will increase at higher heat fluxes and rotational acceleration levels, assuming that a similar condenser design is used. It is very likely that the engine condenser design will have a much different geometry and the effects of vapor drag could be minimized.

5.1.4 Liquid Flow Limits

The liquid flow limits identified in Sections 4.6.1 and 4.6.2 were encountered in the experimental rig because of the low levels of rotational acceleration. These limits will not be significant in the engine at higher G levels.

5.1.5 Blade Conduction

The blade conduction model developed for the experimental rig was for the case of an electrically heated blade modeled as internal heat generation in the blade skin. Both the hub and tip of the blade model were in contact with copper bars and the resulting temperature profile with no cascade cooling had a "conduction profile" with a hotter temperature mid-span and cooling temperatures at the hub and tip. The heat flux distribution on a turbine blade in a gas turbine may be different. There would be no conduction out the tip and the cooling of the turbine disk would also have to be taken into account. One issue that could arise is excessive cooling at the blade hub at startup due to conduction to the turbine disk. During the rig testing, the copper ground strap kept the hub temperature lower than the rest of the blade and may have prevented vapor from flowing into the condenser by causing it to condense on the internal surface of the baffle. While it is not necessary that the vapor be condensed in the condenser, it is necessary that any condensed liquid flow directly back into the shelves. This was not the case in the rig testing, as the baffle prevented condensed liquid from flowing into the shelves unless it condensed in the condenser.

5.2 Issues for Implementation in an Engine

There are several benefits that would come from the implementation of the Return Flow Cascade in a gas turbine engine. First, the ability of the RFC cooling system to maintain the blade temperature at a nearly constant level will reduce the thermal stresses in the blade material. Second, with conventional air cooling, all heat exchange to the air coolant happens in the turbine blade itself. The RFC secondary heat exchanger could be located in the blade root or in the turbine disk. Heat exchanger designs would not be constrained by the geometry of the blade and could use less compressor air. Third, film cooling can cause mixing losses in the turbine which can decrease the thermal efficiency. The Return Flow Cascade is a form of internal cooling and does not have these losses. When film cooling is no longer used, however, the heat flux to blade (and therefore the heat load on the Return Flow Cascade) is increased. A determination of the air flow required to cool the RFC condenser is needed to fully appreciate the savings in performance achievable with the Return Flow Cascade technology. The combination of a more effective heat

exchanger design, lower losses in the turbine, lower thermal stresses in the blade and possibly the addition of a thermal barrier coating to the blade should allow for better engine performance at the current firing temperature levels, or allow some margin to increase firing temperatures.

5.2.1 Blade Geometry

The experimental work has shown that the shelf design, apart from the undersized liquid overflow ports, allows consistent cooling of the entire blade surface area including the leading and trailing edges. Even though the heat flux levels in the experimental work were low compared to engine conditions, the basic shelf design was proven to be effective in distributing liquid throughout the blade and could be used as a baseline design for turbine blades in an engine. The relatively simple internal structure of the evaporatively cooled blade would allow also for more freedom in turbine blade aerodynamic design.

5.2.2 Condenser Design

A major challenge in successfully implementing the Return Flow Cascade in a gas turbine engine is the design of the condenser. Several factors must be taken into account when designing the condenser. First, although the experimental work centered on a single blade with integral condenser, a common condenser could be used for a turbine rotor in an engine. For either design, the distribution of the liquid metal coolant in the system is important, especially for rotor balancing and start-up transients. The possibility of vapor condensation occurring either at the hub of the blade or in the passage connecting the blade and condenser must be considered, in order to avoid the vapor recirculation issues that were a result of the ground strap in the experimental work. Certainly compressor bleed air is the most likely secondary cooling fluid for the condenser heat exchanger, although eventually other options such as engine oil or fuel may be considered.

5.2.3 Internal Coolant

Potassium was identified as the most feasible primary coolant for an engine due to its high heat of vaporization and vapor pressure characteristics. The long term effects of steel and nickel alloys exposed to potassium have been studied [30] and there are no significant corrosion

effects. It should be noted that liquid metal cooling is common in nuclear reactors and in heat pipes without long term damaging effects to the containment material.

5.3 Design Study

A design study was undertaken for a cooled high pressure turbine stage with operating conditions similar to a PW2037 aircraft engine. The purpose of the design study was to make a comparison of both evaporative and film cooling schemes for the turbine blade geometry tested in the current experimental work. Both schemes were analyzed using Inconel 600 as the turbine blade material. In addition, an evaporative cooling analysis was carried out for turbine blades made of a low alloy steel, AISI 4140 to determine whether the use of a lower weight, higher strength material with less ability to withstand high temperatures was feasible. Compressor discharge air was used as the primary coolant for the film cooling scheme and as the secondary coolant for the evaporative cooling scheme.

The results show that the evaporative cooling scheme uses much less compressor discharge air than the film cooling scheme, but adds a non-negligible amount of weight to the rotating disk. Also, the low alloy steel blade can be evaporatively cooled with 2% more core air flow as the film cooling scheme using the nickel based alloy, but from a lower pressure point in the compressor. In either case, replacing film cooling with internal cooling can increase the turbine efficiency by 0.5 – 1.5 % [31].

It should also be noted that this design study does not attempt to optimize the engine design around the improved cooling capability, so the improvement projected is less than could be achieved with a redesigned engine.

5.3.1 Engine Parameters

The engine parameters used in the analysis are shown in Table 5-2. Conditions were assumed to be ground level take-off.

Table 5-2 Engine Parameters for Design Study

Assumed:	
Compressor Pressure Ratio, PR	27.6
Turbine Inlet Temperature, T_4	1650 K (2510 °F)
Turbine Inlet Mach Number, M_4	1
Desired Blade Skin Temperature, T_w	1100 K (1520 °F)
Ambient Pressure, P_o	101325 Pa (14.7 psia)
Ambient Temperature, T_o	293 K (68 °F)
Compressor Efficiency	0.9
Spacing between blades	0.015 m
Hub Radius	0.25 m

Calculated:	
Compressor Discharge Temperature, T_3	808 K (995 °F)
Core Mass Flow	80.5 kg/s (177 lbm/s)
Number of Blades, N_b	44
Heat Flux to Blade	7.57×10^5 W/m^2

The compressor discharge temperature was determined using the definition of compressor isentropic efficiency.

$$T_3 = \left(\frac{PR^{\left(\frac{\gamma-1}{\gamma}\right)} - 1}{\eta_c} + 1 \right) T_o \tag{5.1}$$

The core mass flow was estimated by determining the mass flow rate through the choked turbine nozzle. The number of high pressure first stage turbine blades was determined using the assumed blade hub radius and blade spacing. The number of blades is used only for the purposes of calculating the required cooling air mass flow and may not represent the ideal number of

blades needed for nominal turbine aerodynamic performance. Finally, the heat flux to the blade was determined using a convection analysis for turbulent flow over a flat plate, which is a commonly used first order estimate of turbine blade heat flux.

5.3.2 Evaporatively Cooled Nickel Based Alloy Turbine

The turbine blade design chosen is similar to the design that was used in the experimental work. The overall profile and shape are identical, while the internal shelf structure was modified slightly. The blade parameters are shown in Table 5-3.

Table 5-3 Blade Parameters for Design Study

Given:	
Profile	Shown in Figure 2-5
Chord, c	0.025 m
Span, S	0.035 m
Perimeter, P	0.07 m
Blade Surface Area, A_{blade}	0.0025 m^2
Primary Two-Phase Coolant	Potassium
Secondary Coolant	Comp. Discharge Air
Material	Inconel 600

Calculated:	
Blade Skin Thickness, t_b	0.0005 m
Blade Internal Temperature, T_b	1000 K (1340 °F)
Shelf Spacing, S_{shelf}	0.0012 m
Number of Shelves, N_{shelf}	29
Nominal Pool Depth	0.00025 m
Evaporation Rate, $\dot{m}_{evap}$	0.69 g/s
Blade Center Port Area, A_{bcp}	0.35 cm^2
Power to single blade	1301 W

The blade skin thickness was determined using the thermal stress analysis as outlined in Section 5.1.5. The blade internal temperature takes into account the desired external blade surface temperature and the expected temperature drop through the blade skin. The shelf spacing was set to prevent large thermal stresses along the blade surface. The shelf structure has the same nominal dimension as the skin thickness. The nominal pool depth was then set accordingly. The number of shelves was determined from the blade span and the shelf spacing. The evaporation rate of vapor from the shelves is a function of the heat of vaporization of potassium and the heat flux to the blade.

The blade center port area was set at the same area as the blade used for the experimental work. Some results from the vapor flow model presented in Chapter 4 are shown in Figure 5-2 with the design point (75 W/cm^2, 0.35 cm^2) shown. Since the blade internal temperature was set at 1000 K, there should be no vapor choking at the steady state condition.

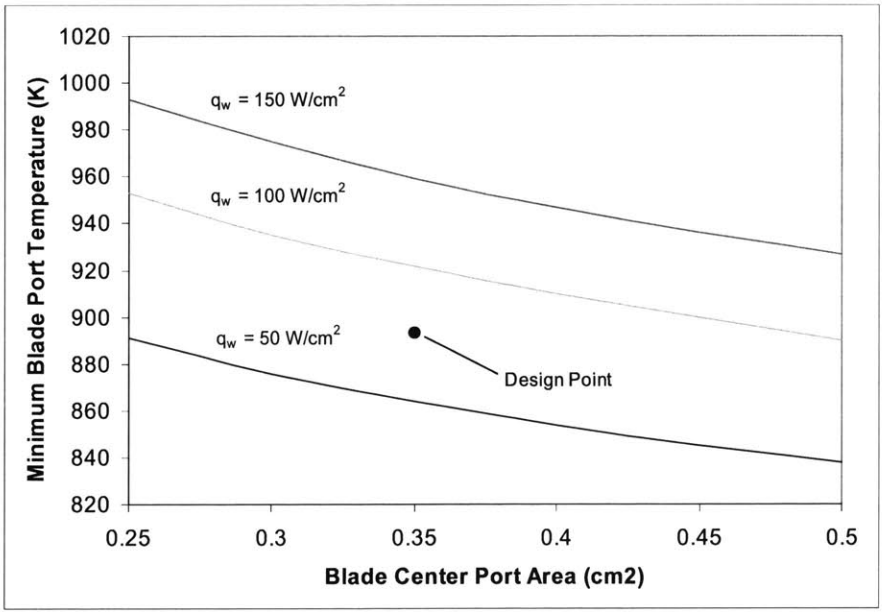

Figure 5-2 Minimum Blade Port Temperature for Non-Choking Flow in Blade Port

There are two main options for the placement of the condenser. The first is to locate the condenser directly below the blade hub with the condensing surfaces attached to the blade stalk. The trade-offs with locating the condenser on the stalk are the limited available space and the extra condenser weight that would contribute to higher stresses in the stalk and turbine disk. The second option is to use a single remotely-located condenser for all turbine blades. The condenser

could be attached to the turbine disk or located on a separate disk. This allows reduced stresses in the blade stalk and disk as well as fewer constraints on heat exchanger area. This would be a the method of choice if fuel or oil were used as the secondary coolant. Because a decision was made to use compressor discharge air and thus allow a direct comparison with film cooling, and an integral condenser design simplifies the analysis of vapor transport from blade to condenser, the stalk mounted condenser was the chosen design for this study.

Table 5-4 Condenser Parameters for Design Study

Given:	
Location	Below hub, attached to blade stalk
Coolant	Compressor Discharge Air
Configuration	Array of finned passages (Figure 5-4)
Material	Inconel 600

The condenser heat exchanger effectiveness as a function of the percentage of core engine flow can be determined from a knowledge of the heat rate and the temperatures of the air and condensing potassium. The effectiveness is defined as

$$\varepsilon = \frac{q}{q_{max}} = \frac{q}{C_{min}\left(T_b - T_3\right)}. \tag{5.2}$$

where $C_{min} = \left(\dot{m}c_p\right)_{min}$, the minimum heat capacity. Since the hot side of the heat exchanger is a condensation process which takes place at constant temperature and has the maximum heat capacity, C_{min} is then equal to the heat capacity of the cooling air and is defined as

$$C_{min} = C_{cold} = \dot{m}_{air} c_{p_{air}}. \tag{5.3}$$

Substituting Equation (5.3) into Equation (5.2) gives a relationship between the effectiveness and the cooling air mass flow rate. This is shown for the estimated heat flux to the blade (7.57×10^5 W/m^2) in Figure 5-3. The more effective the heat exchanger design is, the less cooling air flow is required.

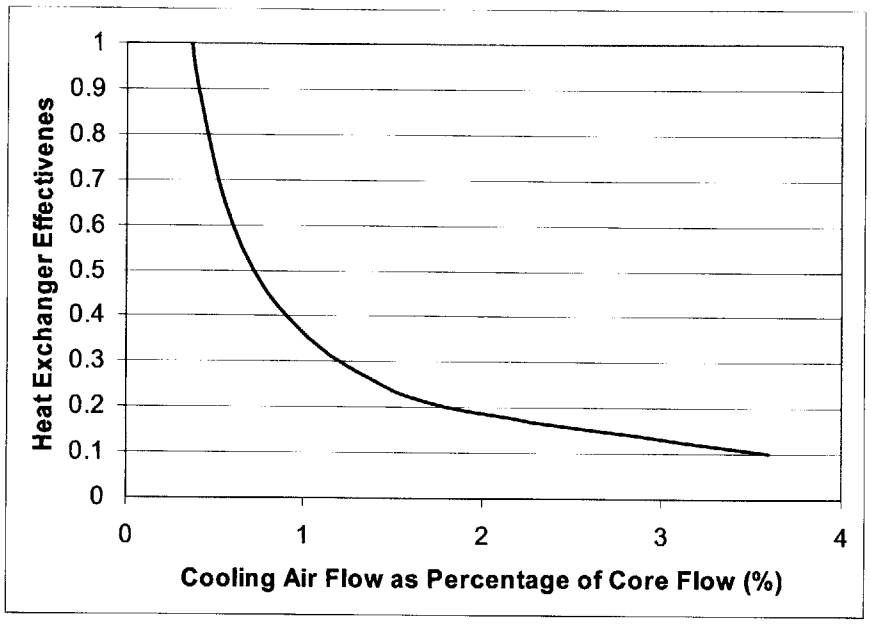

Figure 5-3 Heat Exchanger Effectiveness of Condenser for Evaporative Cooling Design Study

For this design study, a relatively simple condenser design was chosen consisting of a number of finned cooling air passages perpendicular to vapor condensation passages attached to the blade stalk. This design is shown in Figure 5-4. The design variables are the number, size and spacing of the air passages and fins. The whole condenser and stalk structure fits into an envelope just below the blade hub with approximate dimensions of 3.5 cm × 2.5 cm × 1.5 cm. It is important that the original stalk area be maintained throughout the height of the condenser to handle the stress load from the blade. This is shown in the top view in Figure 5-5, where the separate vapor condensing fins can clearly be seen. The load bearing area is shown as the dark shaded regions. The approximate weight addition of the condenser structure is 22.9 grams per blade with a total weight addition of 1.0 kg for the entire disk. This does not take into account the fact that the mass of an evaporatively cooled blade could be less than a conventionally cooled blade due to the increased void area within the blade. This mass addition is not negligible and the disk design may have to be modified to handle the increased stresses. The final condenser design was optimized only for heat exchanger performance and not necessarily for minimal disk

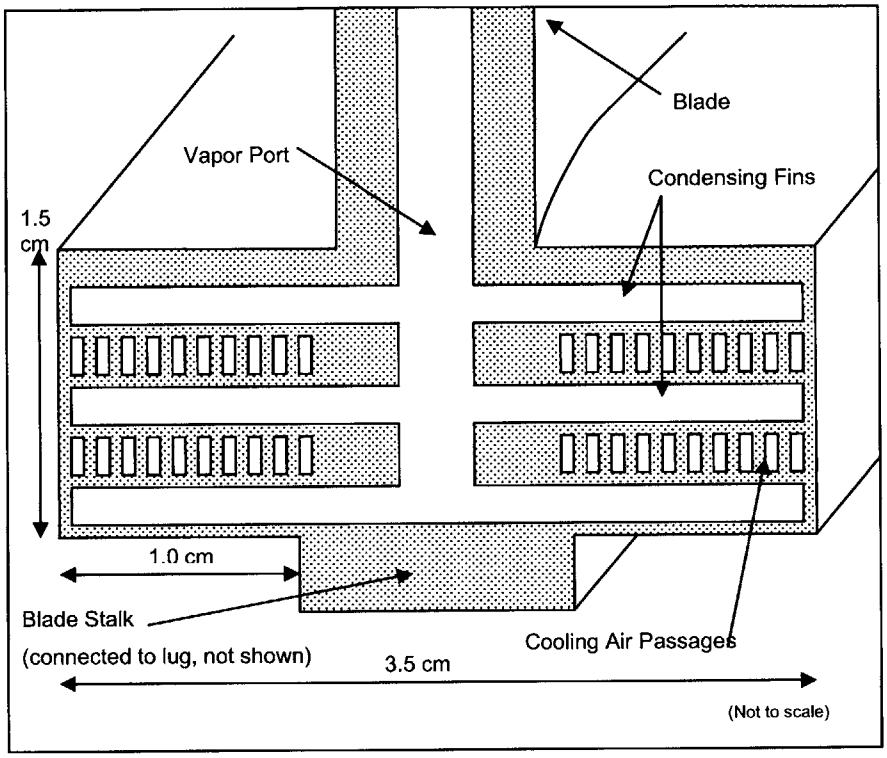

Figure 5-4 Schematic of Condenser Heat Exchanger Cross Section for Evaporatively Cooled Turbine Blade

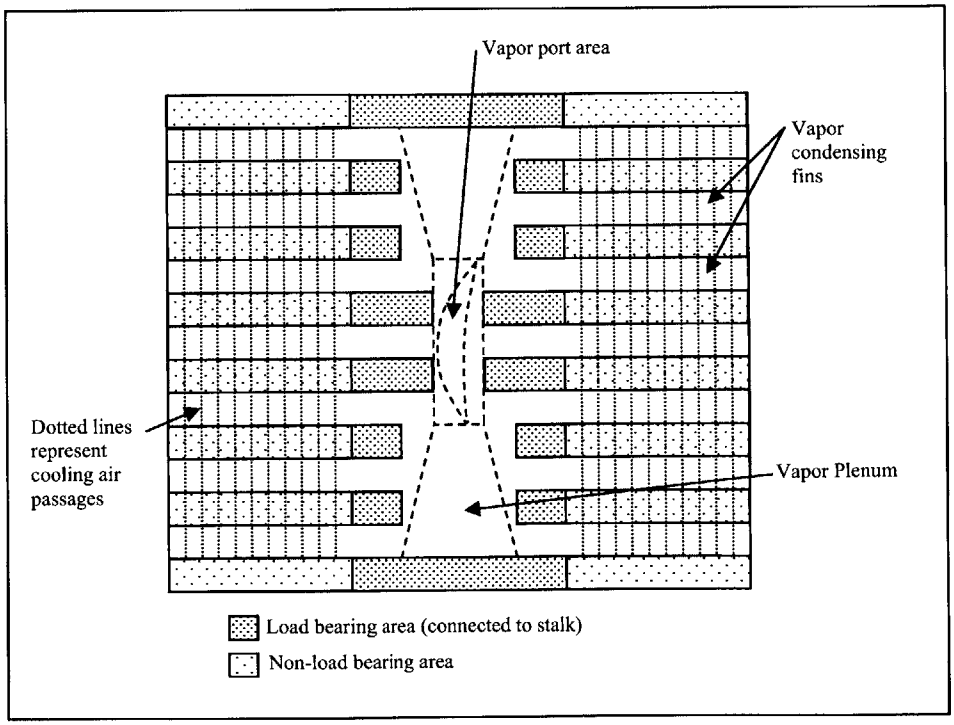

Figure 5-5 Top View of Condenser

and stalk stress, although there is confidence that an acceptable trade-off could be found with additional analysis.

The cooling air mass flow required for a given condenser configuration can be determined using a convection analysis for finned passages. A single array of cooling air passages as shown in Figure 5-6 were analyzed. The geometrical parameters and the cooling air mass flow were varied until the required heat flux per blade could be dissipated. The temperature at the base of the fins, T_b, is constant along the entire length of the passage and corresponds to the temperature of the condensing potassium. Conduction effects through the wall (but not the fins) were neglected.

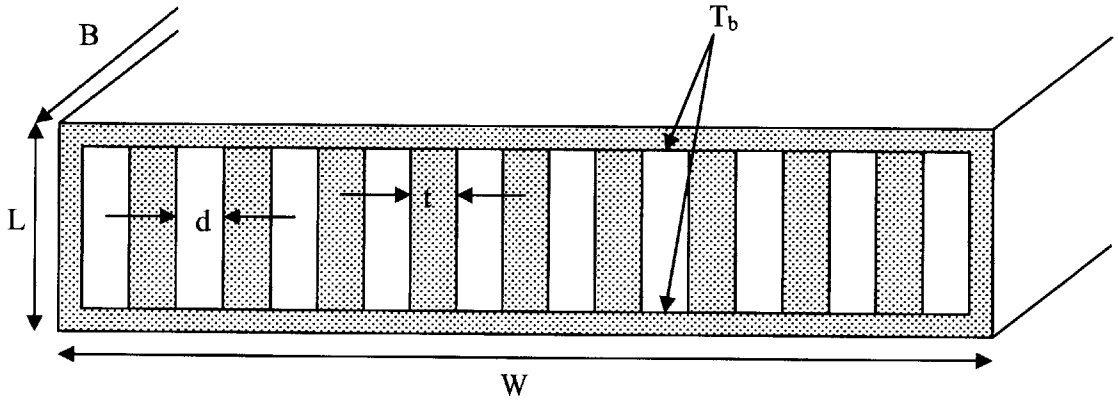

Figure 5-6 Schematic of Single Condenser Array Geometry

The heat flux that can be dissipated by such an array is given by

$$q = 2\bar{h}A_t\eta_o\theta_{b,lm} \tag{5.4}$$

where $\bar{h}$ is the average heat transfer coefficient, A_t is the total surface area of the heat exchanger, η_o is the overall efficiency of the fin array, and $\theta_{b,lm}$ is the log mean temperature difference across the heat exchanger. The fin array efficiency is defined as

$$\eta_o = 1 - \frac{N_f A_f}{A_t}(1-\eta_f) \tag{5.5}$$

where A_f is the surface area of one fin, and η_f is the efficiency of one fin, defined as

$$\eta_f = \frac{\tanh(mL/2)}{mL/2} \tag{5.6}$$

and m is

$$m = \sqrt{\frac{\bar{h}P}{kA_c}}. \tag{5.7}$$

P is the perimeter of the fin, A_c is the cross sectional area, and k is the thermal conductivity of the fin material (in this case, Inconel 600).

The heat transfer coefficient can be determined by modeling the flow as fully developed turbulent flow through a duct. The appropriate correlation is the Dittus-Boelter equation:

$$Nu_D = 0.023 Re_D^{4/5} Pr^{0.4} \tag{5.8}$$

The average heat transfer coefficient can then be found from the definition of the Nusselt number,

$$\bar{h} = \frac{kNu_D}{D} \tag{5.9}$$

where D is the hydraulic diameter of the air passage. Once the total fin array efficiency is found from Equation (5.5), the thermal resistance of the array can be determined:

$$R_{tot} = \frac{1}{2\eta_o \bar{h} A_t} \tag{5.10}$$

and the outlet air temperature is found from

$$\frac{T_b - T_{c,o}}{T_b - T_{c,i}} = e^{\left(-1/\dot{m}c_p R_{tot}\right)}. \tag{5.11}$$

The log mean temperature distance is then

$$\theta_{b,lm} = \frac{\left(T_b - T_{c,o}\right) - \left(T_b - T_{c,i}\right)}{\ln\left[\frac{\left(T_b - T_{c,o}\right)}{T_b - T_{c,i}}\right]} \tag{5.12}$$

The pressure drop through the condenser heat exchanger is determined by using the flow stream pressure drop equation through the heat exchanger core

$$\frac{\Delta P}{P_i} = \frac{(\rho u)^2}{P_i}\left[\left(1+\sigma^2\right)\left(\frac{\upsilon_o}{\upsilon_i} - 1\right) + f\frac{A_t}{A_{free}}\frac{\upsilon_m}{\upsilon_i}\right] \tag{5.13}$$

where σ is the ratio of the heat exchanger free flow area to frontal area, υ is the specific volume, and f is the friction factor for turbulent flow found from

$$f = \left(0.790 \ln Re_D - 1.64\right)^{-2}. \tag{5.14}$$

The final calculated condenser parameters are shown in Table 5-5.

Table 5-5 Evaporative Cooling Results for Design Study

Calculated:	
Condenser Heat Exchanger Effectiveness	0.24
Required Cooling Air Mass Flow, $\dot{m}_{cond}$	1.16 kg/s
Percentage of Core Flow	1.5 %
Outlet Temperature, T_{out}	854 K (1077 °F)
Pressure Drop, $\Delta P/P_{in}$	0.012

The results show that only 1.5 % of the core flow is needed for secondary cooling of the Return Flow Cascade. This is small compared to the percentage that is typically needed for film cooling of the first stage turbine rotor (4 – 10%). The pressure drop and temperature increase through the condenser are acceptable and should allow injection of the coolant flow into the core stream somewhere downstream of the first stage turbine rotor.

It is important to note that these results do not stand alone. They are provided as a comparison to the film cooling study (presented in the next section) and to show the feasibility of the RFC design for an engine.

If lower temperature, lower pressure cooling air was bled from an earlier stage of the compressor, the required mass flow would decrease for the condenser designed described above. This trend is shown in Figure 5-7 along with the expected coolant outlet temperature which is important for determining into which turbine stage the coolant air flow should be reinjected. The increase in cooling air temperature is such that there would still be a large temperature difference (400 – 500 K) between the cooling air and the turbine core flow temperature at the point of injection. The pressure drop in the condenser cooling passages is fairly small ($\Delta P / P_{in} \approx 0.01$). Therefore, the low temperature of the condenser outlet cooling air is the limiting factor in determining which turbine stage the cooling flow should be rejected to.

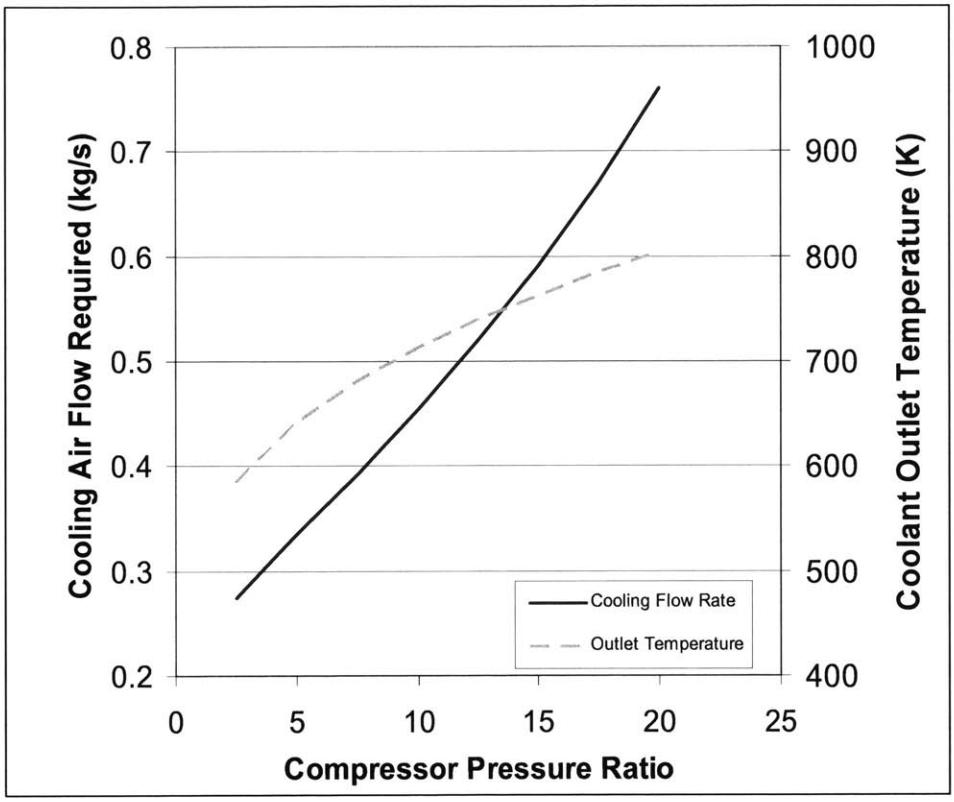

Figure 5-7 Required Cooling Air Flow for Range of Compressor Pressure Ratios

5.3.3 Film Cooling of a Nickel Based Alloy Turbine Blade

For this analysis full coverage film cooling of the turbine blade was assumed. The turbine blade geometry is the same as that use in the evaporative cooling analysis. For comparison purposes, the engine parameters and the desired blade wall temperature are also the same.

Table 5-6 Film Cooling Parameters for Design Study

Assumed:	
Configuration	Full coverage film cooling
Cooling Hole Diameter, D	0.001 m
Number of Cooling Holes in Spanwise Direction	7
Number of Cooling Rows in Chordwise Direction, n	14
Cooling hole injection angle, α	35 °

The adiabatic film cooling effectiveness of the cooling configuration was determined from an analysis by Goldstein [[32]] for multi-row film cooling:

$$\eta_{ad} = \frac{1.9\,\mathrm{Pr}^{2/3}}{1+0.329\left(\frac{c_{p_e}}{c_{p_f}}\right)\xi^{0.8}\beta} \tag{5.15}$$

$$\xi = \left(\frac{X+1.909D}{m_R L}\right)\left(\frac{\mu_f}{\mu_e}\mathrm{Re}_f\right)^{-0.25} \tag{5.16}$$

$$\beta = 1+1.5\times10^{-4}\,\mathrm{Re}_f\left(\frac{\mu_f}{\mu_e}\right)\sin\alpha \tag{5.17}$$

where m_R is the cooling air to core air mass flux ratio and L is the equivalent slot width, defined by

$$L = \frac{n\pi D^2}{4S} \tag{5.18}$$

S is the spacing between cooling holes. Once the adiabatic film efficiency is known, the adiabatic film temperature can be determined:

$$T_{aw} = T_4 - \eta_{ad}\left(T_4 - T_c\right) \tag{5.19}$$

where T_c is the temperature of the air coolant. For this analysis, $T_c = T_3$. The adiabatic film temperature, T_{aw} was then used to estimate the effective heat flux to the blade for the film cooled case, q_{film}. For a given mass flow of cooling air, the heat flux is then

$$q_{film} = \rho u c_p\left(T_4 - T_{aw}\right)\mathrm{St} \tag{5.20}$$

and the Stanton number, St is

$$\mathrm{St} = 0.0295\,\mathrm{Re}_x^{-0.2}\,\mathrm{Pr}^{-0.4} \tag{5.21}$$

The required cooling air mass flow is determined by making an initial guess of the mass flow and then solving for the heat flux, q. The mass flow was varied until the calculated value of q_{film} was reached. The results of the film cooling analysis are shown in Table 5-7.

Table 5-7 Results of Film Cooling Analysis for Design Study

Calculated:	
Adiabatic Film Cooling Effectiveness, η_{ad}	0.255
Cooling Air to Core Air Mass Flux Ratio, m_R	0.23
Required Cooling Air Mass Flow, $\dot{m}_{film}$	2.0 kg/s
Percentage of Core Flow	2.6 %

The percentage of core flow required for film cooling is higher than that required for evaporative cooling of the same blade geometry in the same engine.

5.3.4 Evaporative Cooling of a Low Alloy Steel Turbine Blade

The analysis outlined in Section 5.4.2 was repeated for an evaporatively cooled low alloy steel (AISI 4140) turbine stage. The engine parameters were held constant for both analyses with one exception, the blade surface temperature. A turbine blade made of AISI 4140 can resist creep deformation at temperatures up to 850 K, so a blade wall temperature of 800 K was set, compared to 1100 K for the Inconel 600 blade. The compressor discharge temperature is higher than the desired blade wall temperature, so lower pressure air from the compressor (at a pressure ratio of 20 and a temperature of 733 K) was used to cool the condenser for the steel blade. The condenser design was not changed for the AISI 4140 case. A comparison of the results for evaporatively cooled and film cooled turbines blades, as well as the evaporatively cooled AISI 4140 blade is shown in Table 5-8.

Table 5-8 Cooling Performance Comparison of Nickel Based Alloy and Low Alloy Steel Turbine Blades

Turbine Blade Material	Inconel 600		AISI 4140
Type of Blade Cooling	Evaporative	Film Cooled	Evaporative
Desired Blade Surface Temperature (K)	1100 K	1100 K	800 K
Blade Material Density	8470 kg/m^3	8470 kg/m^3	7850 kg/m^3
Heat to a single blade	1301 W	1301 W	2916 W
Cooling Air Mass Flow Required	1.16 kg/s	2.0 kg/s	5.4 kg/s
% of Core Flow	1.5 %	2.5 %	6.7 %

The results show that the low alloy steel turbine blades can be effectively cooled using the Return Flow Cascade technology with 2% more cooling air than the nickel alloy film cooled blade, but the cooling air can be bled from the compressor at a lower temperature and pressure, ultimately increasing the compressor efficiency. The low alloy steel blades are lighter weight and stronger, resulting in less thermal stresses in the blades. The additional mass of the condenser must be taken into account. The extra weight may end up being an acceptable trade-off to the improved turbine performance, but further design studies that optimize the condenser design against blade weight would have to be done. In any case, the required percentage of core flow to evaporatively cool a low alloy steel blade is well within the range of coolant flows found in current engine technology.

5.3.5 Fuel as a Secondary Coolant for RFC Cooling

Another option for the condenser secondary coolant is engine fuel. The temperature rise in the fuel required to dissipate the blade heat flux for the engine conditions given in Section 5.3.1 was determined to be approximately 100 K, assuming direct fuel cooling of the condenser as designed in Section 5.3.2. There is a maximum temperature to which jet fuel can be heated before it becomes thermally unstable. Beyond this point the fuel can break down chemically which could result in cracking or coking. For a common jet fuel, Jet A, this limit is 443 K. An additive has been developed for a similar military fuel, JP-8, that increases the thermal stability limit by 55 K. An endothermic fuel like JP-7 has a higher heat capacity than Jet A and JP-8 and could handle more enthalpy increase before becoming unstable. The distillation (or boiling)

range of the fuel is also an issue. Jet A, has a boiling range of 443 – 573 K. The fuel delivery and fuel injection systems in a typical commercial aircraft engine are designed to handle liquid fuels. If the fuel is heated to within the boiling range and a significant amount of fuel vapor were allowed to form, the fuel delivery and injection systems would have to be redesigned to handle the larger amount of vapor.

The engine fuel could be used to directly cool the condenser or engine oil could be used as an intermediary. The latter option would require a fuel-oil heat exchanger to be added but would still result in pre-heating of the fuel. In either case, a routing system would have to be designed to deliver fuel to the condenser or heat exchanger and then to the combustor

Engine fuel has a higher heat capacity than compressor discharge air and could effectively cool the condenser designed in the previous sections with a fuel mass flow rate of 0.245 kg/s. A typical fuel flow for the PW2037 engine is 1.6 kg/s at take-off and 0.45 kg/s at cruise. If engine fuel were used to cool the condenser at the cruise fuel flow rate, the heat transfer area could be reduced by half to dissipate the same amount of heat as the air cooled condenser. This would reduce the weight increase from adding a compressor and would reduce stresses on the blade and disk.

5.3.6 Design Study Summary

The results of this design study show that an evaporative cooling system can be designed that performs as well or better than full coverage film cooling. As mentioned previously, turbine efficiency could increase as a result of switching to internal evaporative cooling by removing the losses incurred by film cooling. More work can be extracted from the flow in the turbine and the specific core thrust will increase. Increasing the turbine inlet temperature will further increase the specific core thrust. If less compressor discharge air flow is needed for cooling, more compressor air is available for combustion and the fuel flow rate will increase as a result. The specific fuel consumption, SFC, is defined as $SFC = \dot{m}_f / F$ where $\dot{m}_F$ is the fuel flow rate and F is the thrust. SFC could decrease in an engine with evaporative cooling if the increased thrust offsets the increased fuel flow.

The challenge of reinjecting the condenser cooling air flow into the turbine core flow still remains with evaporatively cooled blades. Engine fuel as a secondary coolant eliminates this

issue, but presents a new set of challenges such as routing the fuel to the condenser, preventing over-heating and chemical breakdown of the fuel, and possible combustor redesign if an endothermic fuel is substituted for its higher heat capacity capability.

Some typical results of the overall effect of using evaporative cooling instead of film cooling are determined using the engine design described in Section 5.3.1 at sea level static conditions. The film cooled case has a turbine inlet temperature of 1650 K. The effect of increasing the turbine inlet temperature by 100 K is shown for the evaporatively cooled case, where T_4 = 1750 K. From Kerrebrock [33] the compressor temperature ratio, τ_c, that produces the maximum specific core thrust is:

$$\tau_c = \frac{\sqrt{\theta_t}}{\theta_o}. \tag{5.22}$$

The maximum core thrust is then

$$\left(\frac{F}{\dot{m}a}\right) = M_o\left(1+\frac{\left(\sqrt{\theta_t}-1\right)^2}{\theta_o - 1} - 1\right). \tag{5.23}$$

The specific impulse is

$$I = \left(\frac{a_o h}{g c_p T_o}\right)\left(\frac{M_o\left(\theta_t - 1\right)}{2\theta_t\left(\theta_o - 1\right)}\right). \tag{5.24}$$

where $\theta_t = T_{t_4}/T_o$, $\theta_o = T_{t_o}/T_o$, $\tau_c = T_{t_3}/T_{t_2}$, T_o is the inlet temperature, h is the heating value of the fuel, M_o is the inlet Mach number, and a is the speed of sound.

Equations (5.22) - (5.24) were used to estimate the approximate overall performance changes that could come from using an evaporatively cooled first stage turbine rotor versus a film cooled rotor. A comparison of the overall engine performance parameters shows an increase of 4.6% in specific core thrust, and an increase of 1% in specific impulse.

Chapter 6 Summary, Conclusions and Future Work

6.1 Summary of Major Findings

The Return Flow Cascade was used to effectively cool a rotating turbine blade model with potassium as the coolant. The cascade cooling maintained the blade surface at a nearly constant temperature and proved to be self-regulating. The first full surface temperature scans of an evaporatively cooled turbine blade clearly indicated when cascade cooling was in effect. The vapor choking limit as predicted by the modeling matched well with the conditions observed during the experimental work. A good understanding of the two-phase flow processes was gained from the experimental and modeling results. The inadvertent effects of excessive blade root cooling and blade tilt were measured and explained.

6.2 Conclusions

Vaporization cooling using the Return Flow Cascade is an effective method for turbine blade cooling in aircraft engines. Compared to direct air cooling, vaporization cooling reduces or eliminates turbine aerodynamic losses and increases engine efficiency. The work described in this dissertation has proven this capability and provides the groundwork for further development of the system. The increased understanding of the internal two-phase processes in an evaporatively cooled turbine blade provides a basis for optimal design of the internal structure of the blade. A demonstration of the Return Flow Cascade in a gas turbine engine will lend credence to the viability of the technology for eventual implementation in gas turbines in service.

The challenges involved in implementing turbine blade cooling via the Return Flow Cascade for a gas turbine engine are two-fold. The first challenge is redesigning the turbine blades and turbine rotor to accommodate the cascade shelves and condenser. Specifically, the weight addition due to either an integral or remote condenser and the issue of what to do with the condenser cooling air will need to be analyzed. The second challenge is to gain a better understanding of the behavior of liquid metal two phase processes at high rotational acceleration. A number of issues based on the experimental and modeling work were identified for engine

operation. These include vapor choking, condenser design to prevent vapor drag, recirculation in the blade, and the long-term effects of exposing the blade material to the liquid metal coolant.

Overall, it is believed that this technology is viable for gas turbine engines. It is a major shift from the conventional air cooling technologies. They are continuously being improved, but with only small gains in engine performance. The Return Flow Cascade solves several of the problems encountered with air cooling and could represent a much larger increase in engine performance. The trade-off is the major effort, testing and redesign that go into developing a new, radically different cooling technology.

6.3 Future Work

The Return Flow Cascade technology is now advanced enough that a test in a gas turbine engine would provide valuable results and a better understanding of the response of the cooling system to gas turbine operating conditions. When the technology has successfully been demonstrated on a test stand, an ideal first application of the Return Flow Cascade would be in a gas turbine used for auxiliary power for aircraft. The mid-range Auxiliary Power Units (APU's) used for Boeing 737 and Airbus A320 aircraft do not currently have cooled rotors, but eventually the increased power requirements from the airframers will necessitate some turbine cooling. There is opportunity here to design a cooling system for a small gas turbine from scratch without replacing an existing cooling system. Another application would be ground based power generation gas turbines. Adding weight is less of a concern than for aircraft engines and there would be more flexibility in developing an optimal Return Flow Cascade cooling design. Finally, the feasibility of using the Return Flow Cascade for radial turbine cooling and the compressor cooling that would be needed in high performance jet engines could be studied.

Since the Return Flow Cascade concept has been shown to successfully cool a representative turbine blade geometry, further experimental work could be done to test proposed cascade shelf and condenser designs. An effective test could be done with a simpler geometry which would allow for faster turn around to get meaningful test results. For example, a simple cylindrical model such as the one tested by Kerrebrock and Stickler [2] could be used. A number of models could be fabricated to make experimental comparisons of the effect of the baffle, the effect of the liquid metal coolant choice, different shelf designs, and different condenser designs.

With the suggestions made above for improvements to the experimental rig, a large compendium of data could be collected that would expand the design space for the Return Flow Cascade.

Should additoinal work be performed in the Rotating Heat Transfer Rig, several improvements are suggested. The ground strap was not necessary for the power levels tested in the current work. Should higher powers be tested, the ground strap may be needed, but should be more carefully designed to minimize heat loss from the hub of the blade. The "solder bathtub" worked well to deliver power to the blade and could be used again. The cooling air flows for the condenser and the transformers should be separated so that an accurate measurement of the condenser cooling air flow can be made. The IR sensor should be calibrated using an identical solid mock-up of the blade model to allow for a predictable temperature profile through the model. The most accurate surface temperature measurements will be obtained by allowing for changes in focal distance and emissivity over the surface of the blade. This is accomplished by developing a calibration curve for each temperature measurement location on the blade. Finally, any future testing of the Return Flow Cascade should involve testing with and without the internal flow baffle to better understand the role it plays in effective cascade operation.

Additionally, there is an opportunity to learn more about the behavior of liquid metal evaporation and condensation at high rotational acceleration levels. An experimental study of the onset of nucleate boiling and the transition to unstable boiling for these conditions would help define the two-phase regimes that could be expected for the Return Flow Cascade.

Appendix A Description of IR System

The blade surface temperature measurement is made using an Electro-Optical System HgCdTe infrared detector [20,21]. The detector is housed in a dewar of liquid nitrogen which is mounted on a two-axis traverse system with the focusing optics, including primary and secondary spherical mirrors. As shown in Figures A.1 and A.2, the sensor and optics remain stationary while the blade model is rotated in from of them. The horizontal traverse is used to set the focus location and the vertical traverse is used to collect radiation readings at different locations along the span of the blade. The magnification of the focusing system is approximately one, so the 1 mm^2 area of the IR detector window collects the radiation from a 1 mm^2 area on the blade surface. In order to provide optical access to both sides of the blade, two first surface flat mirrors are mounted at 45 ° angles at either side of the blade model. The leading edge of the blade is blocked by one of the copper bus bars providing electrical power to the blade, so the entire scan of the blade surface is taken from the reflections off the flat mirrors. A row of data at one spanwise location on the blade can be taken during one pass of the rotating arm. The time needed to collect data over the entire surface of the blade is dependent on the rotational speed and the time needed in increment the vertical traverse to the next spanwise location. A full scan typically took 2 – 3 minutes to complete during the testing.

Previous researchers who used the same facility have described in detail the process of focusing, calibrating and testing the IR system [19, 20, 21] so only a brief outline is included here. Focusing and calibration were done using a mock-up test model which consisted of an electrically heated 0.25 in diameter stainless steel tube mounted on the end of the rotating arm. The appropriate horizontal traverse (focus) setting was determined by seeing where the voltage signal from the heated model was highest. Once this was determined, two thermocouples were tack welded to the back of the model (the side not facing the IR detector) and IR measurements were taken to develop a calibration between IR measured voltage and temperature.

The curvature of the blade causes the IR beam length to be slightly longer or shorter than the focal distance and can cause some uncertainty in the final temperature. This topic is covered in Appendix E, Uncertainty Analysis.

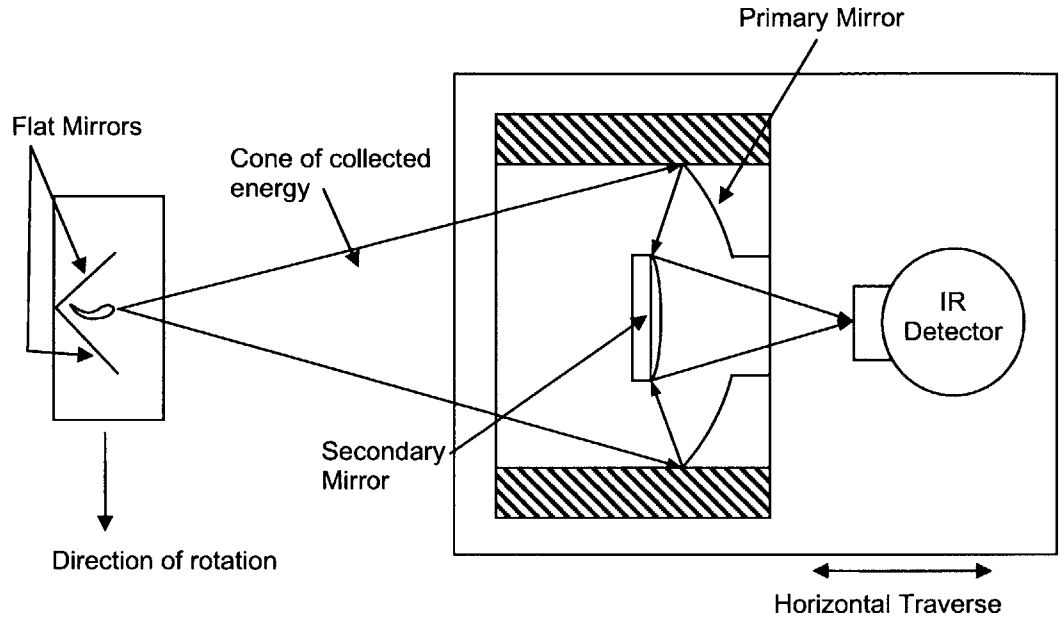

Figure A-6-1 Schematic of Infrared Imaging System for Blade Surface Temperature Measurement – Top View

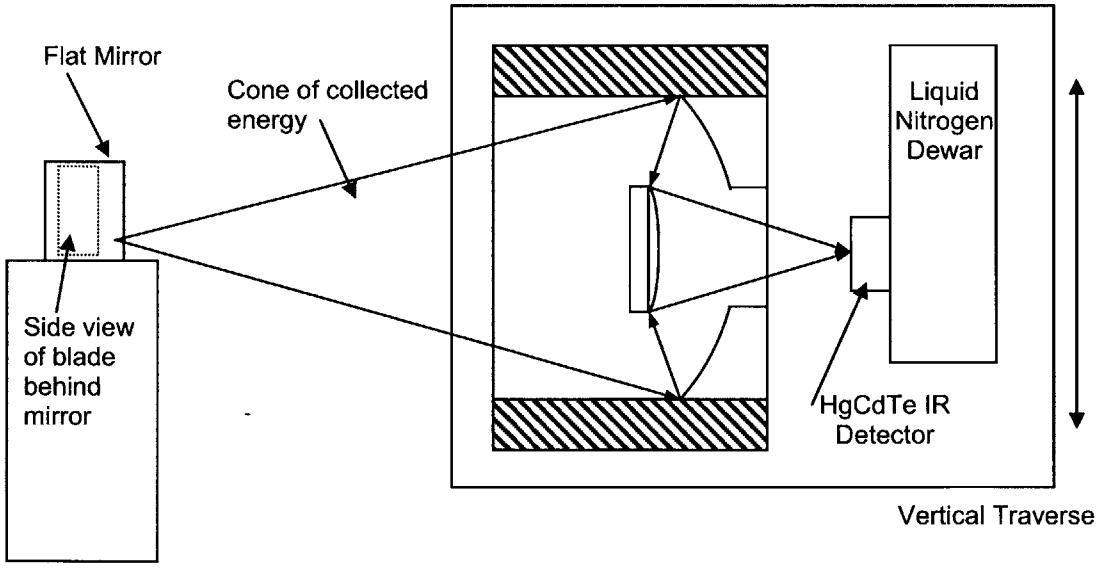

Figure A-6-2 Schematic of Infrared Imaging System for blade Surface Temperature Measurement – Side View

Appendix B Startup and Shutdown Checklists

B.1 Startup Checklist

IR Cooling System

- ☐ Check pressure of LN_2 in dewar (should be greater than 10 psi).
- ☐ Verify that tygon tubing is inserted properly into LN_2 feed tube.
- ☐ Open supply valve on LN_2 dewar.

IR system is cooled when LN_2 is spitting out of return port. If pressure of LN_2 in dewar is less than 10 psi, vent dewar, remove LN_2 delivery device and fill completely with LN_2.

Electrical Power to Instrumentation

- ☐ Turn on power strip for instrument rack.
- ☐ Turn on data acquisition computer.
- ☐ Switch on power to thermocouples.
- ☐ Switch on RPS controller amp power (instrument rack).
- ☐ Turn on and zero flowmeter.
- ☐ Plug in and turn on power strip in traverse instrumentation rack.
- ☐ Plug in power cord for motor controller.

Air and Vacuum Lines

- ☐ Turn on air compressor and dryers (in GTL basement).
- ☐ All valves in air supply line open except yellow handled valve near regulator.
- ☐ Open orange valve in vacuum line.
- ☐ Close light green vent valve.
- ☐ Check rotor arm for loose wires, connections, etc.
- ☐ Close rig and secure clamps.
- ☐ Turn on cooling water to vacuum pump and heat exchanger.
- ☐ Turn on vacuum pump.

Speed Control

- ☐ Open appropriate LabView VI (Focus, Calibration, or Take IR Data)
- ☐ Turn on power to motor.
- ☐ Turn on oil coolant circulating pump.
- ☐ Set motor speed in Labview and start VI.

Power to Blade Model

- ☐ Open yellow handled cooling air valve and set to desired pressure or flow.
- ☐ Turn on power source and set at desired power.

Data Acquisition

- ☐ Turn on IR detector amplifier power (when IR detector is cooled down).

☐ Open appropriate Labview VI's and take data.

B.2 Shutdown Checklist

IR Cooling System
☐ Turn off IR detector amplifier power.
☐ Close supply valve on LN_2 dewar.

Power to Blade Model
☐ Turn off power to model.
☐ Increase cooling air flow.

Speed Control
☐ Set motor speed to zero in Labview.
☐ When motor has wound down, shut down motor.

Air and Vacuum Lines
☐ Close orange valve on vacuum line.
☐ Turn off vacuum pump.
☐ Open light green vent valve.
☐ Undo rig clamps as chamber is venting.
☐ Reduce pressure in air line by turning regulator CW.
☐ Close yellow handled valve in air line.

Full Shutdown
☐ Turn off oil coolant circulation pump.
☐ Unplug power cord for motor controller.
☐ Turn off and unplug power strip in traverse instrumentation rack.

Data Acquisition
☐ Shut off RPS amp power.
☐ Shut off power to thermocouples.

Final Check
☐ Check rotor arm for loose wires, connections etc.
☐ Check blade model and condenser for any signs of coolant leakage.
☐ Turn off water.
☐ Shut down air compressor and dryers.

Appendix C Table of Run Conditions and IR Scans

C.1 Measured Test Parameters

Scan	Rig	Uncorrected	Corrected	Heat Flux	Condenser Temperatures			Air Flow	Blade Tilt	Ground
	Speed	Power	Power		T1	T2	T3		Evident	Strap
	(RPS)	(W)	(W)	(W/cm^2)	(K)	(K)	(K)	ON/OFF		
pp7-8	5	100.3	66.5	2.67	561.2	551	535.2	OFF	No tilt	Installed
pp7-22	10	106.1	58.6	2.35	630.8	630.1	626.9	OFF	No tilt	Installed
pp7-29	10	133.7	60.7	2.43	706	706.1	704.5	OFF	No tilt	Installed
pp7-32	10	155.9	42.5	1.70	738.8	739.3	738.7	OFF	No tilt	Installed
pp7-37	11	158.3	58.9	2.36	760.1	760.7	760.2	OFF	No tilt	Installed
pp7-38	14	158.5	118.2	4.74	779.5	780	779.4	OFF	No tilt	Installed
pp7-41	14	159.3	116.0	4.65	787.4	787.9	787.3	OFF	No tilt	Installed
pp7-42	14	159.0	114.3	4.59	788.9	789.4	788.8	OFF	No tilt	Installed
pp7-43	14	149.4	120.1	4.82	736.4	737.4	737.1	ON	No tilt	Installed
pp7-44	14	100.3	74.1	2.97	585.3	586.1	585.9	ON	No tilt	Installed
pp7-47	15	150.4	114.1	4.58	766.3	766.9	766.3	OFF	No tilt	Installed
pp7-51	15	108.8	82.8	3.32	709.7	710.1	709.1	OFF	No tilt	Installed
pp8-9	10	125.8	54.6	2.19	593.3	589.8	579.6	OFF	No tilt	Installed
pp8-10	15	131.5	63.8	2.56	625.8	623.8	617.1	OFF	No tilt	Installed
pp8-11	15	133.9	104.7	4.20	652	654.8	657.2	OFF	No tilt	Installed
pp8-17	15	178.4	143.0	5.74	678.4	679.6	680.4	ON	No tilt	Installed
pp8-21	15	258.0	207.3	8.32	748.5	749.5	749.1	ON	No tilt	Installed
pp8-23	15	299.8	243.6	9.77	756.4	757.5	757	ON	No tilt	Installed
pp9-1	5	93.2	45.5	1.83	433.1	417.7	400.7	OFF	No tilt	Installed
pp9-2	10	98.1	40.4	1.62	563.7	558.9	549.4	OFF	No tilt	Installed
pp9-3	15	102.2	76.4	3.07	610.1	610.3	610.9	OFF	No tilt	Installed
pp9-4	15	104.4	77.4	3.11	624.7	626.5	628.5	OFF	No tilt	Installed
pp9-5	15	208.5	169.3	6.79	735	735.2	734.4	OFF	No tilt	Installed
pp9-6	15	216.0	144.9	5.81	824.5	824.9	824.5	OFF	No tilt	Installed
pp9-7	15	117.5	80.3	3.22	582	582	584.5	ON	No tilt	Installed
pp9-8	15	143.6	89.8	3.60	761.3	761.5	760.9	OFF	No tilt	Installed
pp9-9	15	204.7	106.1	4.26	867	867.3	867	OFF	No tilt	Installed
pp9-10	15	210.9	158.6	6.36	749.3	749.5	749	ON	No tilt	Installed
pp9-11	15	214.1	162.7	6.53	680.1	680.4	682.2	ON	No tilt	Installed
pp9-12	15	247.9	185.7	7.45	745.1	745.2	744.5	ON	No tilt	Installed

pp10-15	15	198.6	85.2	3.42	Nm	658.5	659.6	OFF	No tilt	Installed
pp10-17	15	198.1	79.6	3.19	Nm	691.6	693.3	OFF	No tilt	Installed
pp10-18	15	194.9	74.6	2.99	Nm	700.3	702	OFF	No tilt	Installed
pp10-19	15	194.5	119.9	4.81	Nm	721.3	723.3	OFF	No tilt	Installed
pp10-22	15	195.5	130.7	5.24	Nm	729.3	730.7	OFF	No tilt	Installed
pp10-25	15	251.2	160.2	6.43	Nm	795.3	796.7	OFF	No tilt	Installed
pp10-26	15	245.0	194.8	7.82	Nm	722.9	724.4	ON	No tilt	Installed
pp10-27	15	293.5	242.9	9.75	Nm	675.5	677.6	ON	No tilt	Installed
pp10-29	15	349.1	290.7	11.67	Nm	725.2	726	ON	No tilt	Installed
pp10-35	15	397.9	340.8	13.68	nm	684.2	687.8	ON	No tilt	Installed
pp11-7	15	198.3	70.2	2.82	608.6	Nm	609.7	OFF	No tilt	Installed
pp11-8	15	205.6	88.9	3.57	656.1	Nm	661.3	OFF	No tilt	Installed
pp11-9	15	206.7	143.2	5.75	694	Nm	697.5	OFF	No tilt	Installed
pp11-10	15	198.4	132.3	5.31	707.4	Nm	711.3	OFF	No tilt	Installed
pp11-11	15	247.3	170.0	6.82	742.7	Nm	747.3	OFF	No tilt	Installed
pp11-16	15	308.2	247.3	9.92	688.3	Nm	693.3	ON	No tilt	Installed
pp11-21	15	351.6	264.2	10.60	681	Nm	687	ON	No tilt	Installed
pp11-24	15	409.2	297.1	11.92	754.4	Nm	758.8	ON	No tilt	Installed
pp11-27	15	453.2	338.6	13.59	725.9	Nm	729.9	ON	No tilt	Installed
pp11-30	15	406.2	296.2	11.88	742.9	Nm	747.8	ON	No tilt	Installed
pp11-32	15	304.9	231.3	9.28	716.8	Nm	721.3	ON	No tilt	Installed
pp12-6	10	143.6	91.9	3.69	568.7	564.2	559.6	OFF	No tilt	Installed
pp12-7	15	137.5	105.1	4.22	583.2	583.5	584.9	OFF	No tilt	Installed
pp12-10	15	200.8	159.0	6.38	665.3	663.2	663	OFF	No tilt	Installed
pp12-12	15	259.2	195.0	7.83	759.7	758	759.7	OFF	No tilt	Installed
pp12-14	15	304.0	208.8	8.38	825.9	823.8	826.1	OFF	No tilt	Installed
pp12-17	15	349.2	248.4	9.97	842.6	840.1	843.1	ON	No tilt	Installed
pp12-19	15	405.6	288.4	11.57	862.2	859.5	862.7	ON	No tilt	Installed
pp12-21	15	457.3	325.6	13.07	888.9	886.1	889.3	ON	No tilt	Installed
pp12-24	15	498.2	387.5	15.55	848.2	845.7	849.8	ON	No tilt	Installed
pp12-26	15	547.0	413.2	16.58	873.3	870.9	873.8	ON	No tilt	Installed
pp12-28	15	604.6	466.9	18.74	872.5	870.4	873.1	ON	No tilt	Installed
pp13-1	5	100.0	96.1	3.85	290	289.5	290.1	OFF	Tilt evident	Installed
pp13-2	9	224.8	81.6	3.28	509.5	480.8	452.4	OFF	Tilt evident	Installed
pp13-7	15	180.0	95.5	3.83	637.8	635.5	637.7	OFF	Tilt evident	Installed
pp13-8	15	173.5	86.6	3.47	641.9	639.3	640.7	OFF	Tilt evident	Installed
pp13-9	15	200.8	73.7	2.96	652	649.7	652	OFF	Tilt evident	Installed
pp13-15	15	198.9	96.0	3.85	740.8	739.2	738.8	OFF	Tilt evident	Installed
pp13-21	15	268.9	140.0	5.62	826	824.8	822.5	OFF	Tilt evident	Installed
pp13-23	15	300.5	142.7	5.73	852.1	850.9	848.3	OFF	Tilt evident	Installed
pp13-24	15.8	241.5	165.3	6.63	726.1	725.3	723.3	OFF	Tilt evident	Installed

pp14-3	10	175.7	114.2	4.58	590.5	588.8	585.4	OFF	Tilt evident	Installed
pp14-6	15	180.5	123.8	4.97	648.1	647.4	647.7	OFF	Tilt evident	Installed
pp14-8	15	253.9	177.5	7.12	737.3	736.1	734.7	OFF	Tilt evident	Installed
pp14-10	15	321.3	197.7	7.93	829.7	828.4	826.4	OFF	Tilt evident	Installed
pp14-11	15	316.9	224.0	8.99	747.9	746.6	745.3	ON	Tilt evident	Installed
pp14-13	15	416.9	306.8	12.31	748	746.8	745	ON	Tilt evident	Installed
pp14-15	16	412.9	272.2	10.92	805.5	804.4	802.1	ON	Tilt evident	Installed
pp14-19	16	426.9	276.1	11.08	827.7	826.9	824.2	ON	Tilt evident	Installed
pp14-21	16	447.7	284.2	11.40	838.3	837.7	834.8	ON	Tilt evident	Installed
pp14-24	16.5	492.8	350.8	14.08	730.5	730.2	727.2	ON	Tilt evident	Installed
pp14-26	16.5	552.5	383.7	15.40	775.9	775.6	772.9	ON	Tilt evident	Installed
pp14-29	16.5	330.5	161.6	6.48	870	869.3	866.3	ON	Tilt evident	Installed
pp14-31	16.5	191.3	90.6	3.64	769.9	769.7	767	ON	Tilt evident	Installed
pp16-1	10	92.0	71.0	2.85	352.4	337.8	326.7	OFF	Tilt evident	Not installed
pp16-2	10	94.3	72.4	2.90	383.6	366.9	352	OFF	Tilt evident	Not installed
pp16-3	10	154.1	116.3	4.67	439	421.8	401.6	OFF	Tilt evident	Not installed
pp16-4	10	154.1	112.1	4.50	503.5	496.9	484.2	OFF	Tilt evident	Not installed
pp16-5	15	141.4	107.4	4.31	536.1	534.3	530.8	OFF	Tilt evident	Not installed
pp16-7	15	216.3	164.1	6.59	577.2	577.7	578.5	OFF	Tilt evident	Not installed
pp16-8	15	218.4	153.8	6.17	668.7	667.9	667	OFF	Tilt evident	Not installed
pp16-9	15	214.5	149.9	6.01	686.2	685.3	684.1	OFF	Tilt evident	Not installed
pp16-14	15	243.9	137.3	5.51	785.5	784.8	782.9	OFF	Tilt evident	Not installed
pp16-15	15	181.7	97.9	3.93	754.5	754	752.2	OFF	Tilt evident	Not installed
pp16-16	10	189.5	102.5	4.11	709.9	709.6	708	OFF	Tilt evident	Not installed
pp16-17	5	0.0	0.0	0.00	520.5	510.6	497.2	OFF	Tilt evident	Not installed
pp17-1	5	103.9	82.7	3.32	326.3	322.8	322.1	OFF	Tilt evident	Not installed
pp17-2	10	103.8	75.8	3.04	474.8	459.4	439.4	OFF	Tilt evident	Not installed
pp17-5	10	152.1	93.3	3.74	582.2	581.4	578.7	OFF	Tilt evident	Not installed
pp17-6	15	140.9	95.8	3.84	599.9	599.1	599.5	OFF	Tilt evident	Not installed
pp17-7	15	142.3	95.7	3.84	603.1	602.4	602.8	OFF	Tilt evident	Not installed
pp17-10	15	216.5	135.2	5.42	699.6	698.6	697.6	OFF	Tilt evident	Not installed
pp17-14	15	287.4	158.0	6.34	791.9	791.1	789.2	OFF	Tilt evident	Not installed
pp17-15	15	300.4	181.9	7.30	771.2	770.4	768.9	ON	Tilt evident	Not installed
pp17-18	15	264.7	181.0	7.26	548	525.3	525.9	ON	Tilt evident	Not installed
pp17-19	15	268.8	183.4	7.36	517.2	509	508	ON	Tilt evident	Not installed
pp18-1	5	112.2	105.3	4.22	288.7	287.8	288.2	OFF	Tilt evident	Not installed
pp18-2	5	115.0	96.1	3.86	401.2	380.7	363.1	OFF	Tilt evident	Not installed
pp18-3	10	114.1	90.9	3.65	465.3	445.2	426.1	OFF	Tilt evident	Not installed
pp18-4	10	105.3	81.6	3.28	473.9	455.1	437	OFF	Tilt evident	Not installed
pp18-5	10	145.9	109.2	4.38	493.8	481.2	470.3	OFF	Tilt evident	Not installed

pp18-6	10	155.3	112.1	4.50	558.7	556.7	557.6	OFF	Tilt evident	Not installed
pp18-7	15	170.2	132.7	5.32	584.7	583.4	586.5	OFF	Tilt evident	Not installed
pp18-8	15	244.1	181.2	7.27	634	633.9	636	OFF	Tilt evident	Not installed
pp18-9	15	291.1	199.0	7.99	765.3	763.5	761.9	OFF	Tilt evident	Not installed
pp18-10	15	378.0	283.7	11.39	725.9	723.9	722.9	ON	Tilt evident	Not installed
pp18-11	15	376.6	294.2	11.81	680.5	678.4	677.6	ON	Tilt evident	Not installed
pp19-10	15	153.7	58.6	2.35	654.5	645		OFF	No tilt	Not installed
pp19-11	15	161.4	97.1	3.90	668	667		OFF	No tilt	Not installed
pp19-12	15	155.0	91.9	3.69	679	676.9		OFF	No tilt	Not installed
pp19-13	15	210.5	71.9	2.88	701.2	698.8		OFF	No tilt	Not installed
pp19-14	15	215.0	52.0	2.09	728.6	725.9		OFF	No tilt	Not installed

C.2 Calculated Parameters

Scan	Average Blade Temperature			Hub Avg.	Tip Avg.
	SS	PS	Total	Temp	Temp.
	(K)	(K)	(K)	(K)	(K)
pp6-4	561.19	574.88	568.04	473.6	523.2
pp6-9	709.85	699.12	704.48	552.2	647.8
pp6-10	714.29	703.14	708.71	575.0	651.9
pp6-15	751.11	705.07	728.09	575.3	674.6
pp6-18	785.47	755.61	770.54	597.4	702.5
pp6-21	839.58	837.69	838.63	643.0	754.3
pp6-22	799.16	802.65	800.90	610.6	717.0
pp6-23	792.94	783.16	788.05	596.2	716.2
pp6-26	786.57	785.48	786.03	599.1	709.6
pp7-8	668.89	664.49	666.69	543.7	579.5
pp7-22	714.20	698.46	706.33	581.9	658.3
pp7-29	768.46	746.44	757.45	616.9	699.5
pp7-32	821.92	811.98	816.95	657.4	732.3
pp7-37	813.89	782.79	798.34	642.1	733.4
pp7-38	694.77	702.13	698.45	612.2	735.4
pp7-41	702.97	711.31	707.14	640.2	728.1
pp7-42	705.79	716.04	710.92	646.1	737.5
pp7-43	659.55	667.52	663.53	586.5	712.4

pp7-44	645.45	655.87	650.66	563.5	681.9
pp7-47	684.17	691.74	687.96	615.7	723.7
pp7-51	649.97	654.40	652.18	565.7	689.1
pp8-9	752.10	753.74	752.92	599.6	680.9
pp8-10	741.52	760.95	751.24	599.9	687.3
pp8-11	653.67	676.07	664.87	578.0	686.2
pp8-17	678.55	694.56	686.55	598.0	713.9
pp8-21	721.79	735.20	728.49	654.5	755.3
pp8-23	735.36	746.64	741.00	663.4	784.1
pp9-1	712.87	698.09	705.48	554.4	676.3
pp9-2	729.74	735.03	732.38	589.4	699.6
pp9-3	635.78	659.28	647.53	558.6	692.5
pp9-4	640.94	665.41	653.18	571.2	683.8
pp9-5	699.91	680.50	690.20	580.1	743.6
pp9-6	760.89	772.12	766.50	682.1	825.4
pp9-7	679.12	694.31	686.72	591.5	735.0
pp9-8	721.77	718.22	720.00	653.9	759.1
pp9-9	806.29	816.98	811.63	735.8	867.4
pp9-10	726.54	728.60	727.57	641.6	791.5
pp9-11	723.76	726.24	725.00	630.4	787.4
pp9-12	749.91	745.23	747.57	670.1	808.7
pp10-15	802.34	823.89	813.11	654.4	705.2
pp10-17	806.39	833.93	820.16	666.5	720.5
pp10-18	808.53	837.32	822.93	669.4	729.9
pp10-19	751.33	774.92	763.13	653.1	723.2
pp10-22	737.42	760.03	748.73	654.3	724.8
pp10-25	785.15	804.49	794.82	703.5	776.2
pp10-26	711.02	733.43	722.22	639.1	760.7
pp10-27	709.49	735.50	722.49	633.6	768.1
pp10-29	727.45	752.05	739.75	654.0	789.2
pp10-35	721.85	749.20	735.52	637.7	796.1
pp11-7	818.61	842.16	830.38	665.2	694.2
pp11-8	810.85	826.35	818.60	652.4	716.4
pp11-9	731.99	759.98	745.99	637.6	713.5
pp11-10	739.15	765.63	752.39	645.2	717.7
pp11-11	764.81	782.04	773.43	672.0	745.0
pp11-16	740.31	749.33	744.82	637.6	759.4
pp11-21	785.04	786.91	785.97	656.2	798.7
pp11-24	820.14	824.15	822.14	698.7	836.5
pp11-27	821.26	823.49	822.38	679.3	844.1

pp11-30	817.08	820.81	818.94	695.9	842.3
pp11-32	767.56	772.21	769.89	665.5	787.3
pp12-6	682.40	751.45	716.92	579.7	685.9
pp12-7	649.21	692.58	670.90	566.8	681.3
pp12-10	677.89	720.09	698.99	595.7	718.8
pp12-12	728.30	774.04	751.17	655.6	760.3
pp12-14	781.30	821.46	801.38	693.0	804.8
pp12-17	790.13	833.92	812.03	709.1	825.6
pp12-19	812.69	856.73	834.71	730.0	856.9
pp12-21	831.83	869.29	850.56	729.2	890.1
pp12-24	807.37	843.13	825.25	714.5	868.0
pp12-26	834.20	875.07	854.63	754.8	894.0
pp12-28	838.50	877.43	857.97	754.4	895.8
pp13-1	481.06	492.70	486.88	432.5	394.2
pp13-2	840.10	860.22	850.16	662.3	683.7
pp13-7	752.60	806.40	779.50	626.9	720.3
pp13-8	756.83	811.07	783.95	630.2	724.2
pp13-9	818.19	851.85	835.02	655.6	750.5
pp13-15	788.10	836.68	812.39	678.2	797.8
pp13-21	829.57	870.38	849.98	729.6	847.8
pp13-23	859.73	903.79	881.76	759.7	889.5
pp13-24	767.80	789.04	778.42	659.9	771.5
pp14-3	715.89	768.42	742.15	591.2	725.3
pp14-6	709.01	759.27	734.14	603.5	743.5
pp14-8	751.98	796.42	774.20	645.1	784.3
pp14-10	822.14	867.49	844.81	730.1	841.3
pp14-11	772.72	824.92	798.82	668.6	821.7
pp14-13	798.01	847.66	822.83	695.0	849.0
pp14-15	829.40	891.64	860.52	726.5	874.4
pp14-19	843.98	903.54	873.76	753.0	883.2
pp14-21	852.83	918.54	885.68	763.6	905.0
pp14-24	816.27	899.27	857.77	716.4	869.9
pp14-26	844.46	926.39	885.42	743.1	886.1
pp14-29	844.24	927.18	885.71	744.0	884.5
pp14-31	788.77	840.50	814.63	707.6	814.2
pp16-1	612.97	647.18	630.08	511.5	637.4
pp16-2	618.68	652.84	635.76	528.5	641.1
pp16-3	673.91	709.38	691.65	577.7	700.6
pp16-4	683.30	721.79	702.55	593.4	706.9
pp16-5	671.29	690.05	680.67	563.9	716.7

pp16-7	707.56	748.66	728.11	614.9	752.5
pp16-8	733.12	777.23	755.18	655.8	771.4
pp16-9	736.25	776.71	756.48	664.6	782.0
pp16-14	809.21	844.51	826.86	747.5	840.8
pp16-15	776.85	810.64	793.74	722.2	800.7
pp16-16	770.58	818.27	794.42	694.6	796.5
pp16-17	516.24	516.83	516.53	514.7	515.7
pp17-1	624.04	636.34	630.19	511.0	592.4
pp17-2	648.25	675.91	662.08	566.1	660.3
pp17-5	714.57	769.25	741.91	625.2	726.4
pp17-6	697.71	727.60	712.65	675.9	740.5
pp17-7	700.26	731.97	716.11	637.5	734.1
pp17-10	759.69	808.87	784.28	685.4	787.3
pp17-14	828.23	875.56	851.90	761.9	839.5
pp17-15	811.72	863.90	837.81	743.7	828.0
pp17-18	763.23	809.40	786.32	654.4	810.5
pp17-19	765.30	810.66	787.98	652.1	813.3
pp18-1	527.22	543.74	535.48	453.0	437.2
pp18-2	614.41	631.55	622.98	522.7	643.5
pp18-3	608.66	656.39	632.52	552.5	638.7
pp18-4	632.66	658.51	645.59	560.6	658.2
pp18-5	672.51	704.68	688.60	590.8	700.3
pp18-6	691.78	724.13	707.95	603.8	721.0
pp18-7	681.87	707.15	694.51	612.8	722.6
pp18-8	730.54	772.56	751.55	654.1	764.9
pp18-9	783.61	826.65	805.13	727.3	814.4
pp18-10	779.04	829.79	804.42	705.9	826.5
pp18-11	763.48	808.34	785.91	682.4	816.9
pp19-10	816.54	789.93	803.23	697.6	716.4
pp19-11	762.48	756.62	759.55	679.1	730.5
pp19-12	758.23	758.36	758.30	684.6	758.6
pp19-13	870.93	841.89	856.41	745.7	768.9
pp19-14	893.51	869.56	881.53	768.5	772.8

Appendix D Matlab Code Listing

D.1 Blade Surface Temperature Data Reduction

```
% bladepostprocess
% Surface Plot of Blade Temperature - Post Processing
% September 9, 2003
clear all;

 % This code plots data that has been manually "cleaned up" to show
 % only the blade.  Corrections have been made for small changes in
 % rotational speed that caused original plots to have chatter.

 % September 23, 2003
 % Added new calibration correlation for xh = 2.75 only.  This is not
 % valid for other focus locations.

 % Change plot size.
 % January 11, 2004

% Input Run Parameters
Nvert = 45; % Number of vertical steps
dx = 0.05; % Azimuthal Data Spacing (cm)
xstart = 0;
xend = 128;
RPS = 10.0; % Rotor speed
Power = 155.9; % Model Power (W)
RunName = 'Rotating Run 7';
Date = '8/25/03';
Time = '3:15 pm';
datafile = 'pp7-32a.dat';
focus = 2.75; % Focus location (in)
T2cond = 738.8;
T3cond = 739.3;
T4cond = 738.7;
wflow = 'OFF';
TSS = 1019.8;
TPS = 1001.9;
q=1.70;

TSSK = round((TSS+459.67)/1.8);
TPSK = round((TPS+459.67)/1.8);

% Populate x matrix
x = (xstart*dx):dx:((xend-1)*dx);

% Read in datafile
[fid,message] = fopen(datafile,'r');
m = Nvert;
n = xend - xstart +5;
[A,count] = fscanf(fid,'%f',[m n]);
```

```
% Separate out y matrix and IR data
yin = A(2:Nvert,2);
y = yin*2.54;
z = A(2:Nvert,6:n);

%Set any negative entries in z matrix to zero.
for i = 1:Nvert-1
   for j = 1:xend-xstart
      if z(i,j) < 0.0
         z(i,j) = 0;
      end;
   end;
end;

% Determine which calibration constants to use.
if focus == 2.50
   a1 = .620833;
   a2 = 6.55180e-11;
   flag = 1;

elseif focus == 2.75
   a1 = 1.502665e8;
   a2 = 4.959407e9;
   a3 = 1.696704e10;
   flag = 3;

elseif focus == 3.00
   a1 = .452393;
   a2 = 6.52321e-11;
   flag = 1;

elseif focus == 3.25
   a1 = .476795;
   a2 = 5.95546e-11;
   flag = 1;

else

   if focus > 3.00
         b1 = .452393;
         b2 = 6.52321e-11;
         c1 = .476795;
         c2 = 5.95546e-11;
         df = focus - 3.00;
         flag = 2;

    elseif focus > 2.75
         b1 = .539210;
         b2 = 7.05695e-11;
         c1 = .452393;
         c2 = 6.52321e-11;
         df = focus - 2.75;
         flag = 2;

    elseif focus > 2.50
```

```
        b1 = .620833;
        b2 = 6.55180e-11;
        c1 = .539210;
        c2 = 7.05695e-11;
        df = focus - 2.5;
        flag = 2;

    end;
end;

% Convert IR voltage data to temperature.

if flag == 1
   T = ((z+a1)/a2).^0.25;
   TF = T*1.8-459.67;

elseif flag == 2
   T1 = ((z+b1)/b2).^0.25;
   T2 = ((z+c1)/c2).^0.25;
   T = (T2 - T1)*df/0.25+T1;
   TF = T*1.8-459.67;

elseif flag == 3
   T = (a1*z.^2+a2*z+a3).^.25;
   TF = T;
end;

% Format matrices for plotting
yrev1 = max(y) - flipud(y);
yrev2 = yrev1 - (max(yrev1)-3.5);
[X,Y]=meshgrid(x,yrev2);
Trev = flipud(TF);

fig2 = figure;
colormap(hsv);
pcolor(X,Y,Trev)
shading flat
v = caxis;
Tmax = round(v(2));
caxis ([300 1030]);
colorbar
axis equal
axis([0 6.3 0.5 3.5])
xlabel('Azimuthal Distance (cm)')
ylabel('Blade Spanwise Distance (cm)')
t4 = title(['Rotor Speed = ',num2str(RPS),' RPS, q = ',num2str(q),' W/cm^2,
Tmax = ',num2str(Tmax),' K']);
set(t4,'FontSize',18)
set(fig2,'Units','pixels');
set(fig2,'Position',[30,300,1000,575])
t5 = text(0.5,0.25,'LE <-- Suction Side --> TE');
t6 = text(4.1,0.25,'TE <-- Pressure Side --> LE');
t7 = text(0.2,0.7,'Hub');
t8 = text(0.2,3.4,'Tip');
```

```
t9 = text(0,0,['Suction Side Avg. Temp = ',num2str(TSSK),' K']);
t10 = text(3.8,0,['Pressure Side Avg. Temp = ',num2str(TPSK),' K']);
t11 = text(0,-0.2,[Date,', ',Time]);
t12 = text(3.8,-0.2,['Condenser Temps: ',num2str(T2cond),',
',num2str(T3cond),', ',num2str(T4cond),' K']);
t13 = text(0,-0.4,[datafile]);
t14 = text(3.8,-0.4,['Cooling Air Flow ',wflow]);

set(t5,'FontSize',10);
set(t6,'FontSize',10);
set(t7,'FontSize',10);
set(t8,'FontSize',10);
set(t9,'FontSize',12);
set(t10,'FontSize',12);
set(t11,'FontSize',12);
set(t12,'FontSize',12);
set(t13,'FontSize',12);
set(t14,'FontSize',12);

Tsave = transpose(Trev);
save plotdata yrev2 Tsave -ascii -tabs
```

D.2 Minimum Temperature for Vapor Choking

```
% Calculation of Minimum Temperature in Blade Port for Non-Choking Flow

% Numerical Integration for Flow Through Blade Port
% August 9, 2002
% Jessica Townsend

% Assume constant temperature in blade port.
% September 9, 2002

% Added ability to run at different g's instead of w's.
% October 2, 2002

% Changed all properties from cesium to potassium
% October 18, 2002

clear all;
warning off;

global i drb drtr Tshelf rtip P r Kb Ktr g R

gam = 1.67;
R = 212.64;
hfg = 1985000;
Absurf = .002492;

Ab = 3.5e-5;
Atr = 3.5e-5;
Ac = 2.61e-4;
```

```
rtip = .5181;
rhub = .4825;
% Radius to bottom of transition section
rtrans = .4656;
% Radius to bottom of condenser
rcond = .4554;

pi = 3.14159;

Nb = 50;
Nq = 30;
Ntr = 10;

qinit = 5e3;
drb = (rhub-rtip)/Nb;
drtr = (rtrans-rhub)/Ntr;

choke = 0;

for i = 1:(Nb+1)
   r(i) = rtip+(i-1)*drb;
end;

for i = (Nb+2):(Ntr+Nb+1)
   r(i) = r(Nb+1)+(i-(Nb+1))*drtr;
end;

   g = 4444;
   w = sqrt(g/rhub);
   RPS = w/(2*pi);

for j = 1:Nq
   j
   q(j) = j*qinit;
   mdot = q(j)*Absurf/hfg;
   dmqdr=mdot/(rtip-rhub);
   Kb = (dmqdr/Ab)^2;
   Ktr = (mdot/Ab)^2;

   Tshelf = 251.1154*q(j)^9.2869e-2;
   Pshelf = 1e6*exp(10.46980-10250.76/Tshelf)*Tshelf^-0.409;
   P(1) = Pshelf;
   % rho(1) = Pshelf/(R*Tshelf);

   % First check to see if initial guess of Tshelf causes flow to choke.  If
it does,
   % choke = 1, if not, choke = 0.
   for i = 1:Nb
      P(i+1) = fzero('FindPibg',P(i),optimset('disp','off'));
      if (P(i+1)>P(i))
         choke = 1;
         break;
      end;
   end;
```

```
   if choke==0
      for i = Nb+1:Nb+Ntr
         P(i+1) = fzero('FindPitrg',P(i),optimset('disp','off'));
         if P(i+1)>P(i)
            choke = 1;
            break
         end;
      end;
   end;

   %If initial guess of Tshelf causes flow to choke, increase Tshelf until a
non-
   %choking condition is reached.
if choke==1
   while (choke == 1)
      Tshelf = Tshelf + 1;
      P(1) = 1e6*exp(10.46980-10250.76/Tshelf)*Tshelf^-0.409;

      for i = 1:Nb
         P(i+1) = fzero('FindPibg',P(i),optimset('disp','off'));
         if (P(i+1)>P(i))
            choke = 1;
            break;
         end;
      end;

      if i == Nb
         choke = 0;
      end;

      if choke == 0
         for i = Nb+1:Nb+Ntr
            P(i+1) = fzero('FindPitrg',P(i),optimset('disp','off'));
            if P(i+1)>P(i)
               choke = 1;
               break
            end;
         end;
      end;

      if i == (Nb+Ntr)
         choke = 0;
      end;
   end;

   Tchoke(j) = Tshelf;

elseif choke == 0
   while (choke == 0)
      Tshelf = Tshelf - 1;
      P(1) = 1e6*exp(10.46980-10250.76/Tshelf)*Tshelf^-0.409;

      for i = 1:Nb
         P(i+1) = fzero('FindPibg',P(i),optimset('disp','off'));
         if (P(i+1)>P(i))
```

```
            choke = 1;
            break;
         end;
      end;

      if choke == 0
         for i = Nb+1:Nb+Ntr
            P(i+1) = fzero('FindPitrg',P(i),optimset('disp','off'));
            if P(i+1)>P(i)
               choke = 1;
               break
            end;
         end;
      end;

   end;

   Tchoke(j) = Tshelf+1;
   Pchoke(j) = P(i);
end;

end;

Tchoke

save chokedata q Tchoke -ascii -tabs -append


% Plots
hold on;
plot(q,Tchoke,'-o');
grid on;
xlabel('Heat Flux to Blade (W/m^2)');
ylabel('Minimum Temperature (K)');
title(['Return Flow Cascade - Minimum Temperature in Blade Port for Non-
Choking Flow']);
hold off;
```

D.3 Pressure Distribution in Blade Port

```
% Pressure Distribution in Blade Port

% Original Program
% August 9, 2002
% Jessica Townsend

% Assume constant system temperature
% Added ability to run at different g's instead of w's
% October 2, 2002

% Change properties from cesium to potassium
% December 9, 2003
```

```
clear all;
warning off;

global i drb drtr drc Tshelf rtip rcond P r Kb Ktr Kc g R

Tmax = 1073;
gam = 1.67;
R = 212.64;
hfg = 1985000;
Absurf = .002492;

Ab = 3.5e-5;
Atr = 3.5e-5;
Ac = 2.61e-4;
rtip = .5181;
rhub = .4825;
% Radius to bottom of transition section
rtrans = .4656;
% Radius to bottom of condenser
rcond = .4554;

pi = 3.14159;

Nb = 50;
Nq = 6;
Nt = 20;
Ntr = 10;
Nc = 50;
Ng = 4;

qmax = 3600;
qinit = qmax/Nq;
drb = (rhub-rtip)/Nb;
drtr = (rtrans-rhub)/Ntr;
drc = (rcond-rtrans)/Nc;

v(1) = 0;


for i = 1:(Nb+1)
   r(i) = rtip+(i-1)*drb;
end;

for i = (Nb+2):(Ntr+Nb+1)
   r(i) = r(Nb+1)+(i-(Nb+1))*drtr;
end;

for i = (Ntr+Nb+2):(Ntr+Nb+Nc+1)
   r(i) = r(Ntr+Nb+1)+(i-(Ntr+Nb+1))*drc;
end;

% 17776 m/s^2 = 15 RPS
   g = 17776;
   w = sqrt(g/rhub);
```

```
   RPS = w/(2*pi);

for k = 1:Nq
   k
   q(k) = k*qinit/Absurf;
   mdot = q(k)*Absurf/hfg;
   dmqdrb = mdot/(rtip-rhub);
   dmqdrc = mdot/(rcond-rtrans);
   Kb = (dmqdrb/Ab)^2;
   Ktr = (mdot/Atr)^2;
   Kc = (dmqdrc/Ac)^2;
   T(k,1) = 251.1154*q(k)^9.2869e-2;

for j = 1:Nt+1
   Tshelf = (j-1)*(Tmax-T(k,1))/Nt+T(k,1)+7;
   Pshelf = (10^6)*exp(10.46980-10250.76/Tshelf)*Tshelf^(-0.409);
   P(1) = Pshelf;
   rho(1) = Pshelf/(R*Tshelf);
   T(k,j) = Tshelf;

   for i = 1:Nb
      P(i+1) = fzero('FindPibg',P(i),optimset('disp','off'));
      rho(i+1)= P(i+1)/(R*Tshelf);
      v(i+1) = mdot/(rho(i+1)*Ab);
      M(i+1) = v(i+1)/sqrt(gam*R*Tshelf);
   end;

   for i = Nb+1:Nb+Ntr
      P(i+1) = fzero('FindPitrg',P(i),optimset('disp','off'));
      rho(i+1)= P(i+1)/(R*Tshelf);
      v(i+1) = mdot/(rho(i+1)*Atr);
      M(i+1) = v(i+1)/sqrt(gam*R*Tshelf);
   end;

   for i = Nb+Ntr+1:Nb+Ntr+Nc
      P(i+1) = fzero('FindPicg',P(i),optimset('disp','off'));
      rho(i+1)= P(i+1)/(R*Tshelf);
      v(i+1) = mdot/(rho(i+1)*Ac);
      M(i+1) = v(i+1)/sqrt(gam*R*Tshelf);
   end;

dPb(k,j) = P(Nb)-P(1);
dPtr(k,j) = P(Nb+Ntr)-P(Nb);
dPc(k,j) = P(Nb+Ntr+Nc)-P(Nb+Ntr);
dPtot(k,j) = P(Nb+Ntr+Nc)-P(1);
dPqP(k,j) = dPtot(k,j)/P(1);
end;

end;

end;

Tt = transpose(T);
dPt = transpose(dPtot);
dPbt = transpose(dPb);
```

```
dPtrt = transpose(dPtr);
dPqPt = transpose(dPqP);


save pressdata Tt dPbt dPtrt -ascii -tabs

% Plots
figure;
hold on;
plot(Tt,dPt);
grid on;
xlabel('Shelf Temperature (K)');
ylabel('Pressure Drop Through Blade Port (Pa)');
title(['Return Flow Cascade - Pressure Drop Through Blade Port']);
hold off;

figure;
hold on;
plot(Tt,dPqPt);
grid on;
xlabel('Shelf Temperature (K)');
ylabel('Pressure Drop Through Blade Port dP/P');
title(['Return Flow Cascade - Pressure Drop Through Blade Port']);
hold off;
```

D.4 Temperature Distribution in Blade

```
% Conduction in Blade
% December 7, 2003
% Jessica Townsend

% This is a finite difference numerical model of the temperature
% distribution in the copper, blade and condenser

% Define material properties

clear all;
% Copper
rho3 = 8933;
cp3 = 231;
k3 = 401;
al3 = k3/(rho3*cp3);

% Nichrome
rho2 = 8314;
cp2 = 525;
k2 = 17;
al2 = k2/(rho2*cp2);

% Stainless steel
rho1 = 8055;
cp1 = 480;
```

```
k1 = 15;
al1 = k1/(rho1*cp1);

% Copper
%rho1 = 8933;
%cp1 = 231;
%k1 = 401;
%al1=k1/(rho1*cp1);

% Internal Heat Generation
Power = 58;
Ablade = 2.49e-3;
tblade = 5e-4;
qgen = Power/(Ablade*tblade);

L1 = 0.23;
L2 = 0.027;
L3 = 0.43;

n1 = 11;
n2 = 21;
n3 = 11;

% Position Step
dx1 = L1/(n1-1);
dx2 = L2/(n2-1);
dx3 = L3/(n3-1);

dt = 0.05;
m = 7200;

T1 = zeros(n1,m);
T2 = zeros(n2,m);
T3 = zeros(n3,m);


for i = 1:n1
   x1(i) = dx1*(i-1);
   T1(i,1) = 366;
end;

for i = 1:n2
   x2(i) = dx2*(i-1);
   T2(i,1) = 366;
end;

for i = 1:n3
   x3(i) = dx3*(i-1);
   T3(i,1) = 366;
end;

for j = 2:m
   t(j-1)=(j-1)*dt;
   T1(1,j) = 366;
      for i = 2:n1-1
```

```
      T1(i,j) = T1(i,j-1)+(dt*al1/dx1^2)*(T1(i-1,j-1)-2*T1(i,j-1)+T1(i+1,j-
1));
   end;
%   T1(n1,j) = T1(n1-1,j)+(k2/k1)*(dx1/dx2)*(T2(2,j-1)-T2(1,j-1));
  T1(n1,j)=((k1/dx1)*T1(n1-1,j-1)+(k2/dx2)*T2(2,j-1))/((k1/dx1)+(k2/dx2));
   T2(1,j)=T1(n1,j);
   for i=2:n2-1
      T2(i,j)=T2(i,j-1)+dt*((al2/dx2^2)*(T2(i-1,j-1)-2*T2(i,j-1)+T2(i+1,j-
1))+qgen/(rho2*cp2));
   end;
 %  T2(n2,j) = T2(n2-1,j)+(k3/k2)*(dx2/dx3)*(T3(2,j-1)-T3(1,j-1));
   T2(n2,j) =((k2/dx2)*T2(n2-1,j-1)+(k3/dx3)*T3(2,j-1))/((k2/dx2)+(k3/dx3));
   T3(1,j) = T2(n2,j);
   for i = 2:n3-1
      T3(i,j) = T3(i,j-1)+(dt*al3/dx3^2)*(T3(i-1,j-1)-2*T3(i,j-1)+T3(i+1,j-
1));
   end;
   T3(n3,j) = 366;
end;

T1p = T1(:,m);
T2p = T2(:,m);
T3p = T3(:,m);

T1pp = T1p*1.8-459.67;
T2pp = T2p*1.8-459.67;
T3pp = T3p*1.8-459.67;

x1p = x1-L1;
x3p = x3+L2;

x2pp = x2*100+0.5;

figure;
plot(x1p,T1p,x2,T2p,x3p,T3p);
t1 = title(['Heat Conduction Model: Temperature Profile in Blade']);
%set(t1,'FontSize',18);
xlabel('Distance (m)')
ylabel('Temperature (K)')
axis([-0.06,0.06,450,1000]);

save conddata x2pp T2pp -ascii -tabs
```

Appendix E Uncertainty Analysis

This appendix quantifies the uncertainty in the measurements presented in this thesis. The uncertainty of an independent measurement is based on the accuracy of the measurement device. All uncertainties provided by the manufacturer of the measurement equipment are assumed to be at a 95% confidence level. Other uncertainties may arise from calibration and curve fitting. The precision error in a derived quantity is propagated using:

$$p_y = \sqrt{\sum_{i=1}^{n}\left(\frac{\partial y}{\partial x_i} p_i\right)^2}$$

where y is a function of n independent variables x_1, x_2, .., x_n, and p_i is the uncertainty in each of the variables x_i. The total uncertainty calculated for each parameter is done at a confidence level of 95% which corresponds to the interval $\mu \pm 2\sigma$, where μ is the true value, and σ is the standard deviation.

E.1 Independent Quantities

E.1.1 Speed Measurement

The speed of the rotating arm was measured using a Model L25 BEI incremental optical encoder and a Measurement Computing PCI-Quad04 Quadrature Encoder Input Board. The manufacturer gives the accuracy of the PCI-Quad04 Board as ±1 count. The encoder has a resolution of 500 counts/rotation. Therefore the uncertainty in the speed measurement for a nominal speed of 15 RPS is ±0.03 RPS.

E.1.2 Temperature Measurement

The sensors used to measure the condenser temperature are Omega Type K, ungrounded, high temperature thermocouples. The manufacturer gives the standard limits of error as ±0.75%. For a nominal temperature measurement of 950 K the uncertainty is b_{T1} = ±4.3 °C. The uncertainty associated with the signal conditioner, an Analog Devices 5B47 Isolated Linearized

Thermocouple Input is $b_{T2} = \pm 1.55$ °C. The total uncertainty in the temperature measurement is the root-sum-square of all the uncertainties in the system.

$$p_T = \sqrt{p_{T_1}^2 + p_{T_2}^2}$$

This equation gives a total uncertainty of $p_T = 4.6$ °C or 8.3 °F.

An Electro-Optical Systems infrared (IR) detector was used to measure the temperature of the blade surface. A detailed description of the operation of the IR detector and the methods for measuring temperature can be found in Chapter 3, Section 3.2. There are three types of errors that contribute to the overall uncertainty in the temperature of the blade surface. The first is the focal distance error. The focal distance is a function of the size and types of mirrors used in the telescope. However, the blade profile has an irregular shape and any given location on the blade surface may be as far as 0.23 inch from the focal length. This corresponds to an error in temperature of ± 16 °C or 28.8 °F. The second error is due to the uncertainty in the Omega Type K thermocouple used as the standard when calibrating the system and is given above as 4.6 °C or 8.3 °F. The third error is associated with fitting the calibration curve to the voltage-temperature data. Using the student-t method with a confidence level of 95%, the calibration error is ± 7.4 °C or 13.3 °F. The total error is found from the root-mean-sum of these three errors and is found to be ± 18.2 °C or 32.8 °F.

Another possible source of error in the measurement of the blade surface temperature is due to the variation in emissivity between the mockup model, which was used to calibrate the IR detector, and the blade model, from which measurements were actually taken. This error is difficult to quantify and not included in the final calculation of uncertainty, but an estimate can be made. The mockup model, made of a stainless steel rod, was heavily oxidized at the time of calibration. The blade model, made of Nichrome, was also heavily oxidized during the testing. If the emissivity of the blade model is taken to be 1.0, then using the calibration curve that was determined for the voltage to temperature conversion, it can be shown that if the mock-up model had an emissivity of 0.95, the temperature calculated from the calibration would be too high by 11.7 K (21 °F).

E.1.3 Current Measurement

The current into the Rotating Heat Transfer Rig is measured using a shunt from Ram Meter Inc. rated at 25 A/50 mV. The manufacturer gives the relative accuracy of the shunt as ± 0.33 %. This corresponds to an absolute accuracy of $p_{C1} = \pm 0.08$ A. A set of transformers on the rotating arm step up the current before it passes through the blade model. To calculate the current through the blade model, a calibration was performed in which the current was measured outside the rig as described above, and inside the rig at the blade model using a Weston 200 A/50 mV shunt. A linear curve with zero-intercept was fit to the data. The uncertainty corresponding to the fit is $p_{C2} = \pm 18.5$ A and was calculated using the student-t distribution with a 95% confidence level. The total uncertainty for the current through the blade model is then

$$p_C = \sqrt{p_{C_1}^2 + p_{C_2}^2} = \pm 18.5 \text{ A}$$

E.1.4 Voltage Measurement

Two voltage measurements were made. The first was made using a Craftsman Professional Multimeter Miniscope with an accuracy of ± 0.02%. This voltage measurement was made during the current calibration process and measured the voltage drop through the blade model from tip to hub. The uncertainty based on a mean voltage of 0.1 V is $p_{V1} = \pm 3.54\text{E-}5$ V.

During the testing, a second voltage measurement was taken of the voltage drop through the blade model from tip to hub. This measurement was made using an Analog Devices 5B40 Signal Conditioner with an accuracy of ± 0.05% FS (0-5 V). The uncertainty in the second voltage reading is then $p_{V2} = \pm 0.0025$ V.

E.1.5 Pressure Measurement

An Omega PX303-100G5V pressure transducer was used to measure the pressure of the cooling air flow to the condenser. The manufacturer gives the error as ± 1%FS. For a full scale value of 100 psi, the absolute uncertainty for the pressure measurement is $u_p = \pm 1$ psi.

E.1.6 Flow Measurement

A Micromotion CFM050 mass flowmeter was used to measure the flow rate of cooling air to the condenser. The manufacturer gives the uncertainty as ± 0.2 % FS. The full scale value of the meter is 5 kg/s and the absolute uncertainty is $u_m = \pm 0.01$ kg/s.

E.2 Derived Quantities

E.2.1 Resistance Calculation

The resistance of the blade is calculated from Ohm's Law:

$$R = \frac{V}{I}$$

The uncertainty in the resistance calculation is given by:

$$u_R = \sqrt{\left(\frac{\partial R}{\partial I} p_I\right)^2 + \left(\frac{\partial R}{\partial V} p_V\right)^2}$$

where the partial derivatives are evaluated at the mean current, 400 A, and the mean voltage, 0.1 V. The uncertainty in the resistance calculation is u_R = 1.156E-5 Ω. The resistance value used in further calculations is actually an average of 6 different measurements. The error associated with the averaging was found using the student-t distribution with a confidence level of 95%. This error is ± 1.664E-4 Ω. The total uncertainty in the value of resistance used for further calculations is the root-mean-sum of the uncertainties given above and is ± 1.664E-4 Ω.

E.2.2 Power Calculation

The power of the blade was calculated in two ways. For Rotating Runs 6 – 9, the power was calculated using the measured current and the average resistance of the blade model:

$$P_1 = I^2 R$$

The uncertainty in the power calculation is given by:

$$u_{P_1} = \sqrt{\left(\frac{\partial P_1}{\partial I} p_I\right)^2 + \left(\frac{\partial P_1}{\partial R} p_R\right)^2}$$

With a mean current of 400 A and a mean resistance of 8.326E-4 Ω, the uncertainty u_{P1} is ± 53.3 W.

The second method for calculating power uses the measured current and measured voltage of the blade model:

$$P_2 = VI$$

The uncertainty of this power calculation is given by:

$$u_{P_2} = \sqrt{\left(\frac{\partial P_2}{\partial I} p_I\right)^2 + \left(\frac{\partial P_2}{\partial V} p_{V_2}\right)^2}$$

With a mean current of 400 A and a mean voltage of 0.10 V, the uncertainty u_{P2} is ± 14.8 W. Based on this result, the second method of calculating power is used for runs where the voltage data is available.

References

[1] Martinez-Tamayo, F., 1995, "The Impact of Evaporatively Cooled Turbine Blades on Gas Turbine Performance," Master's Thesis, Department of Aeronautics and Astronautics, Massachusetts Institute of Technology, Cambridge, MA.

[2] Kerrebrock, J. L., and Stickler, D. B., 2000, "Vaporization Cooling for Gas Turbines, the Return Flow Cascade," Journal of Engineering for Gas Turbines and Power, Vol. 122, pp. 36 – 42.

[3] Dawson, V. P., 1991, Engines and Innovation: Lewis Laboratory and American Propulsion Technology, NASA Publication SP-4306.

[4] Schmidt, E., 1951, "Heat Transmission by Natural Convection at High Centrifugal Acceleration in Water-cooled Gas-turbine Blades," *General Discussion on Heat Transfer*, Institution of Mechanical Engineers, London, Section IV, p. 361.

[5] Cohen, H., and Bayley, F.J., 1955, "Heat Transfer Problems of Liquid Cooled Gas Turbine Blade", Proceedings of the Institute of Mechanical Engineers, Vol. 169, pp. 1063-1080.

[6] Gray, V.H., 1969, "The Rotating Heat Pipe – A Wickless, Hollow Shaft for Transferring High Heat Fluxes," ASME Paper 69-HT-19.

[7] Lee, Y., and Mital, U., 1972, "A Two-Phase Closed Thermosyphon," International Journal of Heat and Mass Transfer, Vol. 15, pp. 1695-1707.

[8] Imura, H., Sasaguchi, S., and Numata, S., 1983, "Critical Heat Flux in a Closed Two-phase Thermosyphon," International Journal of Heat and Mass Transfer, Vol. 26, pp. 1181-1187.

[9] Hong, J. T., Chen S. L., Wang, S.C., 1991, "Effect of Noncondensable Gas on the Performance of a Two-phase Closed Thermosyphon with Wall Conduction," International Communications on Heat and Mass Transfer, Vol. 18, pp. 691 – 704.

[10] Genot, J., and LeGrives, E., 1970, "Liquid Metal Cooling of Turbine Blades", ONERA Paper presented at the AGARD Conference on High Temperature Turbines, Florence. (translated)

[11] Chato, J. C., 1965, "Condensation in a Variable Acceleration Field and the Condensing Thermosyphon," Journal of Engineering for Power, Transactions of the ASME, Vol. 87, pp. 355 – 360.

[12] Ling, J., Cao, Y., and Chang, W. S., 1999, "Analysis of Radially Rotating High-Temperature Heat Pipes for Turbomachinery Application," ASME Journal of Engineering for Gas Turbines and Power, Vol. 121, pp. 306-312.

[13] Ling, J., and Cao, Y., 1999, "Closed-form Analytical Solutions for Radially Rotating Miniature High Temperature Heat Pipes Including Non-condensable Gas Effects," International Journal of Heat and Mass Transfer, Vol. 43, pp. 3661-3671.

[14] Ling, J., Cao, Y., and Lopez, A.P., 2001, "Experimental Investigations of Radially Rotating Miniature High-Temperature Heat Pipes," ASME Journal of Heat Transfer, Vol. 123, pp. 113-119.

[15] Waowaew, N., Terdtoon, P., Maezawa, S., Kamonpet, P., and Klongpanich, W., 2003, "Correlation to Predict Heat Transfer Characteristics of a Radially Rotating Heat Pipe at Vertical Position," Applied Thermal Engineering, Vol. 23, pp. 1019 – 1032.

[16] Kerrebrock, J. L., "Evaporatively Cooled Internal Combustion Engine," U.S. Patent No. 5,299,418, issued April 5, 1994.

[17] Stickler, D. B., and Kerrebrock, J. L., "Evaporatively Cooled Rotor for a Gas Turbine Engine," U.S. Patent 5,954,478, issued September 21, 1999.

[18] Stickler, D. B. and Kerrebrock, J. L., "Improved Evaporatively Cooled Rotor for a Gas Turbine Engine," U.S. Patent No. 5,857,836, issued January 12, 1999.

[19] Katz, H., 1974, "Experience in the Design and Application of Turbine Blade Pyrometers," Progress in Aeronautics and Astronautics, Vol. 34, pp. 409 – 418.

[20] Curwen, K. R., 1974, "Turbine Blade Pyrometer System in the Control of the Concorde Engine," Progress in Aeronautics and Astronautics, Vol. 34, pp. 399 – 407.

[21] Guidez, J., 1989, "Study of the Convective Heat Transfer in a Rotating Cooling Channel," ASME Journal of Turbomachinery, Vol. 111, pp. 43 – 50.

[22] Kreatsoulas, J. C., 1983, "An Experimental Study of Impingement Cooling in Rotating Turbine Blades," Gas Turbine Lab Report #178, Massachusetts Institute of Technology, Cambridge, MA.

[23] Barry, P., 1994, "Rotational Effects on Turbine Blade Cooling," Master's Thesis, Department of Aeronautics and Astronautics, Massachusetts Institute of Technology, Cambridge, MA.

[24] Bons, J., 1997, "Complementary Velocity and Heat Transfer Measurements in a Rotating Turbine Cooling Passage," Ph.D. Thesis, Department of Aeronautics and Astronautics, Massachusetts Institute of Technology, Cambridge, MA.

[25] Blair, Michael F., 1992, "An Experimental Study of Heat Transfer in a Large-Scale Turbine Rotor Passage," Presented at the International Gas Turbine and Aeroengine Congress and Exposition, Cologne, Germany, June 1-4.

[26] Dwyer, O.E., 1976, Boiling Liquid-Metal Heat Transfer, American Nuclear Society.

[27] Edwards, J.A. and Hoffman, H.W., 1965, "Superheat with Boiling Alkali Metals," Proceedings of the Conference on Application of High-Temperature Instrumentation to Liquid-Metal Experiments, Argonne National Laboratory, September 28 – 29, ANL-7100.

[28] Lienhard, J.H. and Dhir, V.K., 1973, "Extended Hydrodynamic Theory of the Peak and Minimum Pool-Boiling Heat Fluxes," NASA Report CR-2270.

[29] Mill, A.F., 1992, Heat Transfer, Richard D. Irwin, Inc.

[30] Phillips, W. M., 1969, "Some Alkali Metal Corrosion Effects in a Rankine Cycle Test Loop," Proceedings of the Sessions on Corrosion by Liquid Metals of the 1969 Fall Meeting of The Metallurgical Society of AIME, Philadelphia, Pennsylvania, pp. 197 – 215.

[31] Lakshminarayna, B., 1996, Fluid Dynamics and Heat Transfer of Turbomachinery, John Wiley & Sons, Inc.

[32] Goldstein, R. J., et al., 1985, "Effect of Surface Roughness on Film Cooling Performance," ASME Paper 84-GT-41, Journal of Engineering for Power, Vol. 107.

[33] Kerrebrock, J.K., Aircraft Engines and Gas Turbines, 1992, The MIT Press, Cambridge Massachusetts.

4788-51